Tensile-Strained Germanium *via* III-V Heterostructures for Emerging Electronic and Photonic Applications

Shuvodip Bhattacharya

Dissertation submitted to the Faculty of the

Virginia Polytechnic Institute and State University

in partial fulfillment of the requirements for the degree of

Doctor of Philosophy

in

Electrical & Electronics Engineering

Mantu K. Hudait, Chair

Mariusz Kriysztof Orlowski

Xiaoting Jia

Levon Volodya Asryan

Jean Joseph Heremans

May 09, 2025

Blacksburg, Virginia

Keywords: Molecular Beam Epitaxy, Germanium, Tensile Strain, Heterogeneous Integration, Metamorphic Buffers, Effective Carrier Lifetime, Carrier Dynamics, Doping, Microwave Reflectance Photoconductance Decay

Copyright 2025, Shuvodip Bhattacharya

Tensile-Strained Germanium *via* III-V Heterostructures for Emerging Electronic and Photonic Applications

Shuvodip Bhattacharya

(ABSTRACT)

The relentless scaling down of feature dimensions in silicon (Si)-based complementary metal-oxide-semiconductor (CMOS) architectures has been the primary catalyst for the enhancement of technological functionalities within portable electronic systems and computational infrastructures. Concurrently, advancements in condensed matter physics, materials science, and state-of-the-art fabrication methodologies have collectively facilitated continued improvements in device performance metrics. Nonetheless, as Si and strained-Si-based platforms approach phenomenological saturation thresholds, the pursuit of alternative channel semiconductor materials becomes imperative. Simultaneously, the escalating integration of Si photonics aims to mitigate the performance bottleneck imposed by copper-based electrical interconnects at nanoscale dimensions. In this context, band-engineered germanium (Ge) emerges as a pivotal candidate for propelling next-generation electronic and photonic device paradigms. This study systematically examines unintentionally doped and heavily boron (B)-doped, tensile-strained germanium (ε-Ge), synthesized *via* III-V metamorphic buffer layers comprising InGaAs and InAlAs. The structural quality and carrier dynamics of such Ge epilayers is characterized with a comprehensive suite of advanced techniques, including transmission electron microscopy (TEM) for defect analysis, high-resolution x-ray

diffractometry (HR-XRD) for strain and lattice parameter determination, microwave-reflectance photoconductive decay (μ-PCD) to quantify effective carrier lifetimes τ_{eff}, and atomic force microscopy (AFM) for surface morphology assessment. Through iterative refinement of epitaxial growth parameters, defect-limited $\tau_{eff} > 100ns$ is achieved in *unstrained* Ge and ε-Ge, with strain levels surpassing the indirect-to-direct bandgap crossover threshold. These findings position ε-Ge as a viable material for photonic device integration. Furthermore, detailed comparative analyses reveal that heteroepitaxial growth on InGaAs templates yields superior crystalline quality compared to InAlAs counterparts, establishing InGaAs as the preferred buffer for ε-Ge integration. The feasibility of integrating overlayers on ε-Ge to mimic quantum well separate confinement heterostructure configurations is demonstrated, enabling the fabrication of Ge-based active optical sources. Notably, for the first time, combined experimental validation and atomistic modeling elucidate that high boron incorporation within highly ε-Ge layers induces an additive tensile strain, which dynamically alters the defect landscape during epitaxial growth. This comprehensive investigation thus advances the fundamental understanding of ε-Ge/III-V heterostructures, equipping device engineers with vital insights for engineering next-generation electronic and photonic systems optimized for scalability, performance, and integration.

Tensile-Strained Germanium *via* III-V Heterostructures for Emerging Electronic and Photonic Applications

Shuvodip Bhattacharya

(GENERAL AUDIENCE ABSTRACT)

Transistors are essential components in a wide range of electronic devices and computing systems used in modern technology. The ongoing miniaturization of silicon-based complementary metal-oxide-semiconductor (CMOS) transistors over recent decades has played a vital role in achieving significant enhancements in computational performance, supported by parallel developments in solid-state physics, materials science, and manufacturing processes. Furthermore, improved fabrication methods have enabled high-volume, cost-effective production, increasing accessibility for consumers and industries alike. As a result, micro- and nano-electronic devices are now widespread across various sectors, interconnected within the Internet of Things ecosystem, with vast amounts of data being shared and managed by data centers and related infrastructure. However, the continued downscaling of transistors is approaching fundamental physical limitations. As device dimensions shrink, challenges such as increased power density, leakage currents, and heat dissipation become more prominent. Similarly, copper interconnects used for circuitry communication are experiencing performance constraints, with increased signal delay and potential reliability concerns. To sustain the trajectory of ongoing performance improvements, research into alternative materials and innovative solutions is essential. This study systematically examines the material properties and

carrier dynamics of epitaxially grown Germanium and tensile strained Germanium using III-V buffers, aiming to advance applications in emerging electronic and photonic devices. Through a comprehensive suite of analytical and modeling methods, the work explores various approaches to fabricating high-quality Germanium epitaxial layers. Additionally, the research demonstrates the potential of heterostructures for developing Germanium-based optical sources, which could serve as viable alternatives to copper interconnects nearing their performance limits. Overall, this work provides valuable insights into these material systems, equipping device engineers with knowledge necessary to continue the advancement of semiconductor device performance.

Dedication

To my Bapi, for His unwavering love, vision, and the dream that we are now fulfilling together...

To my Ma, for giving me the gift of love, perseverance, and scholarship...

Acknowledgments

This has been an incredible journey for me, which helped me develop both as a scholar and in the personal front. It is needless to say that this dissertation would not have seen the light of day without the contribution, support, and guidance of my community.

First, I would like to extend my sincerest appreciation and respect to my advisor, Professor Mantu Hudait, for his continued guidance and encouragement throughout my time at Virginia Tech. His extensive knowledge and expertise in semiconductor science and never dimming enthusiasm toward fundamental research has influenced and helped me become the curious researcher I am today. I am grateful for his mentorship and the opportunities that he provided me through several in-depth conversations about research. Beyond an academic relationship, it has been a joy to discuss several different topics and learn about different perspectives of viewing the world.

Secondly, I would like to thank Professors Levon Volodya Asryam, Jean Joseph Heremans, Xiaoting Jia, and Mariusz Kriysztof Orlowski for their incessant support and encouragement as members of my Ph.D. committee.

Additionally, I would like to thank all my team members from my research group: Advanced Devices & Sustainable Energy Laboratory (ADSEL) who I shared this journey with, including, but not limited to: Michael Clavel, Sengunthar Karthikeyan, Muntasir

Mahdi, and Apoorva Rose. Similarly, I owe my gratitude to all my friends, professors, colleagues, and supervisors who have encouraged me throughout this journey.

I would like to take this opportunity to extend my sincerest gratitude to the Engineering Education Department for their continued financial support and Benjamin Chambers, Hulya Dogan, Tamara Knott, Holly Matusovich and Juan Ortega for their camaraderie.

I would, however, be simply remiss if I did not express my gratitude for Donald Leber, Mark Hollingsworth, and Rick Johnston for sharing the gift of friendship, besides their professional expertise in the fabrication and characterization facilities at Virginia Tech.

I am deeply indebted to my beloved parents, Drs. Sharmila Bhattacharya and Prasenjit Bhattacharya, for their perpetual understanding and belief in my abilities. Their steadfast belief in my potential has been my guiding light. They were my first teachers and, although, I lost my father while pursuing this academic journey thousands of miles away from home, their teachings have shaped and will continue to shape me. Their values and dreams fuel my spirit and inspire me to carry forward.

To Sanjukta, my extraordinary partner in all things... Words cannot fully express how profoundly thankful I am for your resolute, unconditional love. Your boundless patience and faith in me have carried me through my darkest, most challenging moments. Even across the miles that have separated us at times, your steadfast belief and your willingness to stand by my side ignited a fire within me that refused to burn out. This

triumph—it is not just mine; it is a testament to your incredible strength, support, and the love that sustains us. I am finally done, and I owe everything to you. This achievement is as much yours as it is mine, and I cherish you more than words can ever express.

This work is partly supported by National Science Foundation (NSF) under Grant numbers **ECCS-1348653**, **ECCS-1507950**, and **ECCS-2042079**—*a US-Ireland joint R&D program.*

Contents

List of Figures **xiv**

List of Tables **xxii**

1 Introduction **1**

1.1 Brief History of Silicon and its Impact on the Semiconductor Industry . . . 1

1.2 Silicon Bottleneck in CMOS and Considerations for New Channel Materials 4

1.3 Application in Electronic Devices: Germanium as a Channel Material . . . 5

1.4 Application in Photonics: Rise of Silicon Photonics and Germanium for Optical Sources . . . 9

1.5 Germanium Optical Sources: Strategies and Applications . . . 11

1.6 Minority Carrier Lifetime as a Metric for Material Quality . . . 13

1.7 Aim of this Work and Dissertation Outline . . . 16

Bibliography . . . 19

2 Interplay between Strain and Thickness on Effective Carrier Lifetime of Buffer Mediated Epitaxial Germanium probed by Photoconductance Decay Technique **41**

2.1 Introduction 43
2.2 Experimental Section 45
2.2.1 Materials Synthesis 45
2.2.2 Materials Characterization 46
2.3 Results and Discussion 49
2.3.1 Strain Analysis *via* HR-XRD 49
2.3.2 Structural Characterization *via* HR-XTEM 53
2.3.3 Material Quality Characterization *via* μ-PCD 55
2.4 Conclusion 64
Bibliography 65

3 Elucidating the Role of InGaAs and InAlAs Buffers on Carrier Dynamics of Tensile Strained Germanium Double Heterostructures 77

3.1 Introduction 79
3.2 Experimental Section 82
3.2.1 Materials Synthesis 82
3.2.2 Materials Characterization 83
3.3 Results and Discussion 85
3.3.1 Analysis of strain state and InAs composition using HR-XRD 85

3.3.1.1 Cation (Ga, Al) grading in InAs-based buffer 86
3.3.1.2 Overlayer growth and strain state in (001) biaxially tensile strained Ge 92
3.3.2 Strain State Estimation using Raman Spectroscopy 94
3.3.3 Surface Morphology *via* AFM 99
3.3.4 Effective Carrier Lifetime Analysis *via* μ-PCD 104
3.3.4.1 Effect of strain template on (001) biaxially tensile strained Ge 106
3.3.4.2 Effect of overlayer growth on (001) biaxially tensile-strained Ge 108
3.4 Conclusion 111
Bibliography 113

4 Heavy Boron Doping Effects on Biaxially Tensile Strained Germanium (> 1.5%) investigated via Structural Characterization, Effective Lifetime Assessment and Atomistic Modeling 125

4.1 Introduction 128
4.2 Experimental Section 131
4.2.1 Materials Synthesis 131
4.2.2 Materials Characterization 132

4.3 Results and Discussion . . . 136
4.3.1 ε-Ge Strain State and Buffer InAs Composition Analysis using HR-XRD . . . 136
4.3.2 Heterostructure analysis *via* TEM . . . 142
4.3.3 Effective Minority Carrier Lifetime using μ-PCD . . . 150
4.3.4 Atomistic simulation for B-induced deformation of Ge-Ge bonds . . . 154
4.4 Conclusion . . . 162
Bibliography . . . 164

5 Summary and Future Prospects **177**
5.1 Summary . . . 177
5.2 Future Work . . . 184
Bibliography . . . 187

Appendices **189**

Appendix A List of Publications **191**

List of Figures

1.1 Bandgap *vs.* bulk mobility landscape of Si, Ge and common III-V materials. Used with permission of Springer Nature [8]. 7

2.1 Cross sectional schematics of the heterostructures studied in this work, namely (a) *unstrained* Ge/AlAs/GaAs, (b) 0.61% ε-Ge/$In_{0.115}Ga_{0.885}As$, and (c) 0.89% ε-Ge/$In_{0.173}Ga_{0.827}As$. 48

2.2 (a) Symmetric (004) RC of the *unstrained* and ε-Ge heterostructures, obtained *via* x-ray analysis. Pendellösung oscillations observed clearly in the unstrained and 0.61% ε-Ge epilayer, and partially in the 0.89% ε-Ge epilayer, indicate superior material quality. (b)-(c) Symmetric (004) and asymmetric (115) RSMs of the strained heterostructures, respectively. Here, *r.l.u.* represents reciprocal lattice unit ($Å^{-1}$). The RLCs for the corresponding layers are labeled accordingly. 50

2.3 Low-magnification cross-sectional bright-field TEM micrographs obtained from (a) ε-Ge/$In_{0.115}Ga_{0.885}As$ and (b) ε-Ge/$In_{0.173}Ga_{0.827}As$ heterostructures, respectively, showing the extended stack. High-magnification cross-sectional bright-field micrographs from (c) ε-Ge/$In_{0.115}Ga_{0.885}As$ and (d) ε-Ge/$In_{0.173}Ga_{0.827}As$ heterostructures, respectively, showing the heterointerfaces. The insets show the corresponding FFT patterns from the entire visible area. Exclusive FFT patterns generated from each individual region in (c) and (d), are shown in (e-g) and (h-j), respectively. The diffractograms show no peak splitting, indicating contribution from a single lattice parameter across the heterointerfaces. 56

2.4 (a) Typical transient μ-PCD curves obtained from varying thicknesses of the *unstrained* Ge/AlAs/GaAs heterostructure. τ_{eff} values labeled alongside the curves are obtained by fitting the principal mode of decay with an exponential regression. (b) Extracted τ_{eff} (unfilled circles) are plotted against $2/d$, where d is the epilayer thickness, showing the linear fit according to $1/\tau_{eff} = 1/\tau_{bulk} + 2S/d$. Separation of the lifetime components yielded $\tau_{bulk} = 114 \pm 2\ ns$ and $S = 21.3 \pm 0.04\ cm/sec$. Given the good fitting ($R^2 = 0.9931$), a point on the linear fit corresponding to $d = 75\ nm$ (*green diamond*) yielding $\tau_{eff} \approx 69\ ns$ was extracted to eliminate thickness effect while comparing lifetime performance of ε-Ge epilayers. The traces shown in Figure 2.4 (a) are normalized and vertically shifted for viewing clarity. 59

2.5 (a) Typical transient μ-PCD curves obtained from 270 nm *unstrained* Ge/AlAs/GaAs, 75 nm 0.61% ε-Ge/$In_{0.115}Ga_{0.885}As$, 75 nm 0.89% ε-Ge/$In_{0.173}Ga_{0.827}As$ and 30 nm 1.6% ε-Ge/In0.24Ga0.76As heterostructures. The traces have been normalized and vertically shifted for clarity. (b) Extracted τ_{eff} shown in (a) and extracted from etched 100 nm *unstrained* Ge/AlAs/GaAs (*see Figure 2.4(b)*) plotted against the imparted in-plane tensile strain (ε) to Ge epilayers, 0% indicating *unstrained* epilayers. The alternate y-axis shows the critical layer thickness, h_c, calculated based on the People and Bean strain energy-balance model [52]. The thickness effect on τ_{eff} is also shown (black arrow, pointing downward) indicating the reduction in τ_{eff} with decreasing thickness. A point taken on the fit of Figure 2.4(b) corresponding to $d = 75\ nm$ yielding $\tau_{eff} \approx 69\ ns$ (*green diamond*) is also indicated, which was used to eliminate thickness effect when comparing τ_{eff} between *strained* and *unstrained* Ge epilayers. The observed increase in τ_{eff} as strain is increased is indicated using the green arrow pointing upward at an angle. 61

3.1 Representative schematics of the heterostructures studied in this work. Toward the left of each heterostructure, the InAs composition grading (solid red) with growth thickness is represented along with the estimated compositions from XRD analyses on the abscissa. The figure is not drawn to scale. 84

3.2 (a)-(b) Symmetric (004) RSMs obtained from heterostructures A35 and B, respectively. The alignment of the ε-Ge RLCs (black dotted) with the InGaAs and InAlAs virtual substrates confirms pseudomorphic epitaxy. (c)-(d) Asymmetric (115) RSMs obtained from heterostructures A [38] and B, respectively. The strained (R=0, dotted black) and relaxed (R=1, dotted red) lines are shown. The slight misalignment of the ε-Ge RLCs with the InAlAs RLC is indicated (dotted red). 91

3.3 Projection of symmetric (004) RSM spectra to $\Delta\theta = \Delta(2\theta)/2$ axis recorded from heterostructures C and D. The peak positions of the ε-Ge epilayers were found using weighted Gaussian fits to the projection spectra. The Bragg peak positions (°) and full width at half maximum (FWHM) (arcsec, $''$) values obtained from the fits are included in the legend box. 95

3.4 Raman spectra obtained from heterostructures A and B overlapped with Raman spectra recorded from (001)Ge substrate. Peak positions were found using Lorentzian fits to the spectra. The inset shows the strain relationship between the recorded Raman spectra and the tensile strain calculated using $\Delta\omega = b \cdot \varepsilon_{\parallel}$, where $\boldsymbol{b}$ and $\varepsilon_{\parallel}$ denote the fitting parameter and in-plane strain, respectively. The error margins for strain estimation are indicated by the shaded regions. In-plane tensile strain, $\varepsilon_{\parallel}$, estimated from XRD (Table 3.1) are also indicated by the corresponding symbols. 98

3.5 (a) and (c) Atomic force micrographs of $20\mu m \times 20\mu m$ representative regions obtained from heterostructures A and B, respectively. The orthogonal directions $\langle 110 \rangle$ are indicated. (b) and (d) Line profile scans showing the height variations along the orthogonal directions. Orthogonal R_q values for heterostructure B are not reported in (d) due to absence of observable cross-hatch. 102

3.6 μ-PCD transient curves recorded from (a) Heterostructures A [38] and B and (b) Heterostructures C and D, respectively. The effective lifetime is obtained in each case by fitting an exponential regression to the principal mode of decay (solid black). 109

4.1 Schematic representation of the heterostructures analyzed in this study. Heterostructure C serves as the *unstrained* control sample with 270 nm epitaxial Ge on vicinal $2°\langle 110 \rangle$ (001)GaAs substrates, with AlAs as an intermediate buffer. For heterostructures A and B, respectively, 30 nm of 1.53% and 1.68% biaxially tensile strained epitaxial Ge was grown on InGaAs virtual substrates. The boron doping concentration ($N_A \approx N_B$, where N_A denotes the acceptor concentration) for all heterostructures was confirmed *via* Hall measurements of van der Pauw structures to be $N_B \approx 7 \times 10^{19}\ cm^{-3}$. 133

4.2 (a)-(b) Symmetric (004) RSMs recorded from heterostructures A and B, respectively. The dotted orange lines connect the RLCC of the InGaAs VS and the ε-Ge epilayer used for characterization. The dotted black lines are provided to indicate the expected position of the Ge epilayer RLCC in the absence of tilt. (c)-(d) Asymmetric (115) RSM scans recorded from heterostructures A and B, respectively, with the dotted black and orange lines having the same significance as described previously. The dotted red line (R=1) signifies the trajectory along which the InGaAs VS RLCCs would be positioned if they were fully relaxed. 139

4.3 (a) Cross-sectional low magnification bright-field TEM recorded heterostructure B showing the full stack. (b) High-resolution cross-sectional bright-field TEM recorded from heterostructure B, showing a representative ε-Ge/$In_{0.25}Ga_{0.75}As$ heterointerface region. The dotted yellow lines indicate the 10 nm $\times$ 10 nm regions of interest (ROIs) analyzed. The inset presents the FFT pattern ($\mathfrak{F}(\omega)$) derived from the entire region. The presence of an abrupt and coherent interface is evident by the difference in atomic factor contrast between Ge and $In_{0.25}Ga_{0.75}As$. A stacking fault is identifiable in this figure along the projected $\langle 112 \rangle$ directions. (c)-(e) Inverse FFT patterns ($\mathfrak{F}^{-1}(\mathfrak{F}(\omega))$) corresponding to ROI-1, ROI-2 and ROI-3, respectively, obtained by selectively masking the $(1\bar{1}1)$ planes from the FFT pattern displayed in the inset of Figure 4.3(b). The dotted yellow line in Figure 4.3(e) signifies the area of the two-monolayer twin observed in ROI-3. 143

4.4 (a) High-resolution cross-sectional bright-field TEM micrograph from a representative region of ε-Ge/In$_{0.25}$Ga$_{0.75}$As heterointerface recorded from heterostructure B. The dotted yellow lines highlight the 10 nm $\times$ 10 nm ROIs analyzed. The variation in thickness, indicative of surface roughness, is represented by the dotted white lines, along with the corresponding measured thickness. (b)-(c) FFT ($\mathfrak{F}(\omega)$) diffraction patterns derived from ROI-4 and ROI-5, respectively. (d)-(e) Inverse FFT patterns ($\mathfrak{F}^{-1}(\mathfrak{F}(\omega))$) from ROI-4, obtained by selectively masking $(11\bar{1})$ and $(1\bar{1}1)$ diffraction points, respectively, with no lattice plane discontinuities observed. (f)-(g) Inverse FFT patterns from ROI-5, also obtained by selectively masking $(11\bar{1})$ and $(1\bar{1}1)$ diffraction points, respectively, where lattice discontinuity is noted only along the $(11\bar{1})$ planes, as indicated by the additional dotted white line. (h) Inverse FFT pattern obtained by mapping all diffraction points from ROI-5, clearly illustrating the stacking fault ribbon, with the 90° leading and 30° trailing PDs highlighted, as explained in the main text. The slip plane $(11\bar{1})$ is marked by the dotted yellow line. 146

4.5 Typical μ-PCD transient decay curves recorded from heterostructures A, B and C, as illustrated in Figure 4.1. The effective minority carrier lifetime, τ_{eff}, is indicated for each trace. The traces have been normalized to the peak intensity and vertically shifted for clarity. 151

4.6 (a) Depicts a representative supercell utilized for the atomistic modeling of B dopant atoms in a (001) oriented Ge. The dimensions of the supercell are defined as $x = y = 3 \times a_{[110]}$ and $z = 2 \times a_{[001]}$, to preserve periodic boundary conditions. The dotted black line illustrates one such [110] oriented unit cell, each of which consists of either 4 Ge atoms, or 3 Ge atoms and 1 B atom. (b) Outlines the qualitative model employed for this study along the [001] direction, based on the assumption that $2r = \sqrt{a_{[110]}^2 + \left(\frac{a_{[001]}}{2}\right)^2} \approx \sqrt{a_{[110]}^2 + \left(\frac{a_{[110]}}{\sqrt{2}}\right)^2}$. The calculated changes in bond lengths are referenced against the geometry optimized *undoped*, *unstrained* bulk Ge supercell. It should be noted that tetragonal distortion induced by the III-V strain template is not considered in this qualitative model. 157

5.1 Summary of key findings in this research work. μ-PCD measured τ_{eff} values are plotted against the in-plane biaxial tensile strain, ε. 181

List of Tables

2.1 Summary of strain properties of ε-Ge and In composition of $In_xGa_{1-x}As$ VSs extracted from symmetric (004) and asymmetric (115) HR-XRD RSM analyses. 53

2.2 Summary of extracted parameters from HR-XRD, XTEM and μ-PCD measurements, including τ_{eff} and goodness of fit (R^2) achieved from *unstrained* Ge and ε-Ge. The microwave pump source wavelength for μ-PCD measurements, carried out at 300 K, was kept constant at $\lambda = 1500$ nm for all samples. 63

3.1 Summary of extracted parameters from HR-XRD, XTEM and μ-PCD measurements, including τ_{eff} and goodness of fit (R^2) achieved from *unstrained* Ge and ε-Ge. The microwave pump source wavelength for μ-PCD measurements, carried out at 300 K, was kept constant at $\lambda = 1500$ nm for all samples. 93

4.1 Benchmarking effective minority carrier lifetimes (τ_{eff}) of ε-Ge epilayers measured using μ-PCD technique. The microwave pump source wavelength for all reported measurements, carried out at 300 K, was kept constant at $\lambda = 1500$ nm. 155

4.2 Summary of extracted parameters obtained from atomistic simulation of *undoped* and **B**-doped *unstrained* and *tensile strained* Ge supercells 160

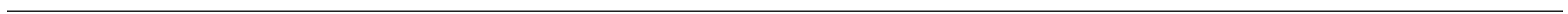

Chapter 1:

Introduction

1.1 Brief History of Silicon and its Impact on the Semiconductor Industry

The seminal development of the point-contact transistor in the year 1948 is generally acknowledged as a pivotal inflection point in the evolutionary trajectory of semiconductor physics and electronic device engineering. The phenomenon of superconductivity was initially empirically characterized through experimental observations by Heike Kamerlingh Onnes in 1911 at the Leiden Cryogenics Laboratory, thereby predating the formal recognition of semiconducting materials as a distinct electronic phase of condensed matter. Prior to this, in 1882, Thomas Alva Edison identified thermionic emission phenomena, commonly denoted as the Edison effect, representing the earliest documented experimental evidence of electron emission in thermally stimulated materials. Building upon this foundational knowledge base, John Ambrose Fleming introduced the vacuum tube rectification device in 1904—specifically, the thermionic diode—marking the first experimentally validated electronic rectification

component, which contributed substantially to the development of early wireless communication systems employing amplitude modulation techniques. The exigency for miniaturized, high-gain electronic amplification modules during the subsequent decades, particularly in the context of WWII military technology, catalyzed extensive research initiatives in solid-state physics and quantum electrodynamics, providing the theoretical underpinning necessary for practical device implementation. Under the scientific leadership of William Shockley and Alan Holden at Bell Laboratories, systematic investigations into solid-state amplification mechanisms commenced circa 1938, with the overarching aim of fabricating a compact, reliable, solid-state electron amplifier to supplant bulky vacuum tube technology. This research culminated in the successful realization of the first operative bipolar point-contact transistor in 1947—developed collaboratively by John Bardeen, Walter Brattain, and William Shockley—using a germanium substrate as the semiconducting medium. Subsequently, in 1948, William Shockley engineered an enhanced configuration—the bipolar junction transistor (BJT)—which closely approximates modern BJT architectures. BJTs maintained dominance in integrated circuit manufacturing until the advent and proliferation of complementary metal-oxide-semiconductor (CMOS) technology, which eventually displaced BJTs in many mainstream applications due to their superior power efficiency and scalability. Following this initial breakthrough, numerous subsequent discoveries profoundly influenced the semiconductor industry and the broader field of electronic systems. Notably, silicon emerged as the semiconductor substrate of choice following Morris Tanenbaum's demonstration of a silicon-based junction transistor in 1954; silicon's advantageous properties—including superior thermal conductivity, thermomechanical stability, and reduced intrinsic noise at operational conditions—firmly

established its preeminence in semiconductor device fabrication.

Modern electronic systems are fundamentally driven by advanced semiconductor device architectures. Silicon's pivotal role underpins the exponential growth observed in micro- and nano-electronic technologies, enabled by aggressive device scaling strategies rooted in the principles of Moore's Law. These strategies involve systematic reduction of key geometric parameters—such as channel length, gate oxide thickness, and doping profiles—to decrease transistor footprint area. This dimensional minimization facilitates increased integration density and circuit complexity, thereby accelerating computational performance and functional capabilities. Gordon Moore's predictive formulation [1] posited that the number of transistors integrated on a monolithic chip would double approximately every two years, resulting in proportional improvements in digital logic throughput, switching speed, and functional density, while concurrently diminishing dynamic power dissipation. Empirical validation of Moore's Law persisted until at least the early 21st century. Initial microprocessors contained on the order of several thousand transistors—approximately 2,300—whereas contemporary microprocessors integrate a few billion transistors, a feat made feasible through sequential scaling cycles, process innovations, and advanced lithographic techniques that enable sub-10 nanometer feature dimensions.

1.2 Silicon Bottleneck in CMOS and Considerations for New Channel Materials

The previously delineated aggressive dimensional reduction paradigm in complementary metal-oxide-semiconductor (CMOS) device fabrication introduced a series of complex technical challenges that necessitated the development and integration of advanced process innovations. Between the 90 nm and subsequent nodes, significant modifications included the implementation of strain engineering techniques aimed at the modulation of carrier mobility; notably, in the 2003 milestone, strain-induced mobility enhancement was concretely employed within the 90 nm technology node [2] to satisfy the performance criteria delineated by the International Technology Roadmap for Semiconductors (ITRS). Concurrently, the conventional gate dielectric material—silicon dioxide (SiO_2)—was systematically supplanted with high-permittivity (high-κ) dielectric materials to mitigate the otherwise prohibitive gate leakage currents that arose due to quantum tunneling phenomena in ultra-thin dielectric layers. This dielectric engineering was complemented by the reintroduction of metal gate technology, specifically the high-κ metal gate (HKMG) stack, which effectively stabilized threshold voltage (V_{TH}) control metrics at the 45 nm node [3]. The technological paradigm shift at the 22 nm technology node involved the transition from planar two-dimensional (2D) MOSFET architectures to three-dimensional fin field-effect transistors (FinFETs). These FinFETs exhibited enhanced electrostatic control, resulting in increased drain current (IDS) and elevated I_{ON}/I_{OFF} ratios—parameters representing the dynamic (drive) current and the static (leakage) current, respectively [4]. This architectural evolution was pivotal in counteracting the deceleration of scaling progress. Despite these advances, CMOS

technology derived from crystalline silicon channels is nearing the physical and dopant activation limits, presenting a saturation in further dimensional downscaling [5–7]. The exponential increase in power density associated with further device shrinking has necessitated the development of advanced thermal management techniques, including highly efficient cooling methodologies and innovative packaging strategies. These constraints have impelled the research community and industry stakeholders to pursue alternative device architectures, as well as exploration into novel channel materials—such as compound semiconductors or two-dimensional materials—to sustain the trajectory of performance enhancement [7–9].

1.3 Application in Electronic Devices: Germanium as a Channel Material

In the context of assessing the feasibility of emergent channel semiconducting materials for integration into next generation nano-electronic architectures, a comprehensive set of quantitative and qualitative criteria must be rigorously fulfilled. These criteria encompass the electronic band structure parameters—specifically, the material's fundamental bandgap (E_g), which correlates directly with the device's operating voltage window, as well as the intrinsic charge carrier mobilities for both electrons (μ_e) and holes (μ_h). Additional critical parameters include the thermal stability margins across the operational temperature spectrum and the material's compatibility metrics with established CMOS fabrication processing workflows [8]. Over the past several decades, III-V compound semiconductor alloys have garnered significant research attention owing

to their superior electronic transport characteristics, which provide substantial enhancements over monolithic Si-based devices across various performance metrics [9–12]. As illustrated in Figure 1.1, which depicts the experimental and theoretical bulk electron mobility across a range of elemental and compound semiconductors—including Si, Ge, and select III-V materials—the data indicate that III-V compounds demonstrate markedly elevated electron mobility values relative to silicon.

Quantitatively, InAs and InSb exhibit electron mobilities that surpass those of bulk Si by approximately three orders of magnitude, emphasizing their potential for high-speed digital and analog applications. Furthermore, high-electron-mobility transistors (HEMTs) fabricated with alloys such as indium gallium arsenide (InGaAs)—a trinary alloy derived from InAs and GaAs—have demonstrated exceptional radio frequency (RF) and microwave frequency performance metrics, with cutoff frequencies ($f_{T,max}$) on the order of approximately 1 terahertz [13–15]. These findings underscore the importance of material selection in achieving the desired high-frequency operational thresholds.

Current mainstream semiconductor technology predominantly employs the CMOS architecture, which integrates paired n-type (n-MOS) and p-type (p-MOS) field-effect transistors (FETs). Since the device drive current density (J) is directly proportional to charge carrier mobility (μ), as expressed by $\vec{J} \propto \mu_{h,e} \cdot \vec{E}$ (where $\vec{E}$ is the applied electric field), reduction in hole mobility (μ_h) results in proportional degradation of p-MOS drive capability. Empirical data from Si-based nodes reveal that the ratio of maximum attainable drive current densities $\left(\left|\vec{J}_{max}\right|\right)$ between n-MOS and p-MOS transistors typically approaches a magnitude of approximately 3:1 under standard fabrication conditions. In contemplating alternative channel materials to supplant silicon, the ratio

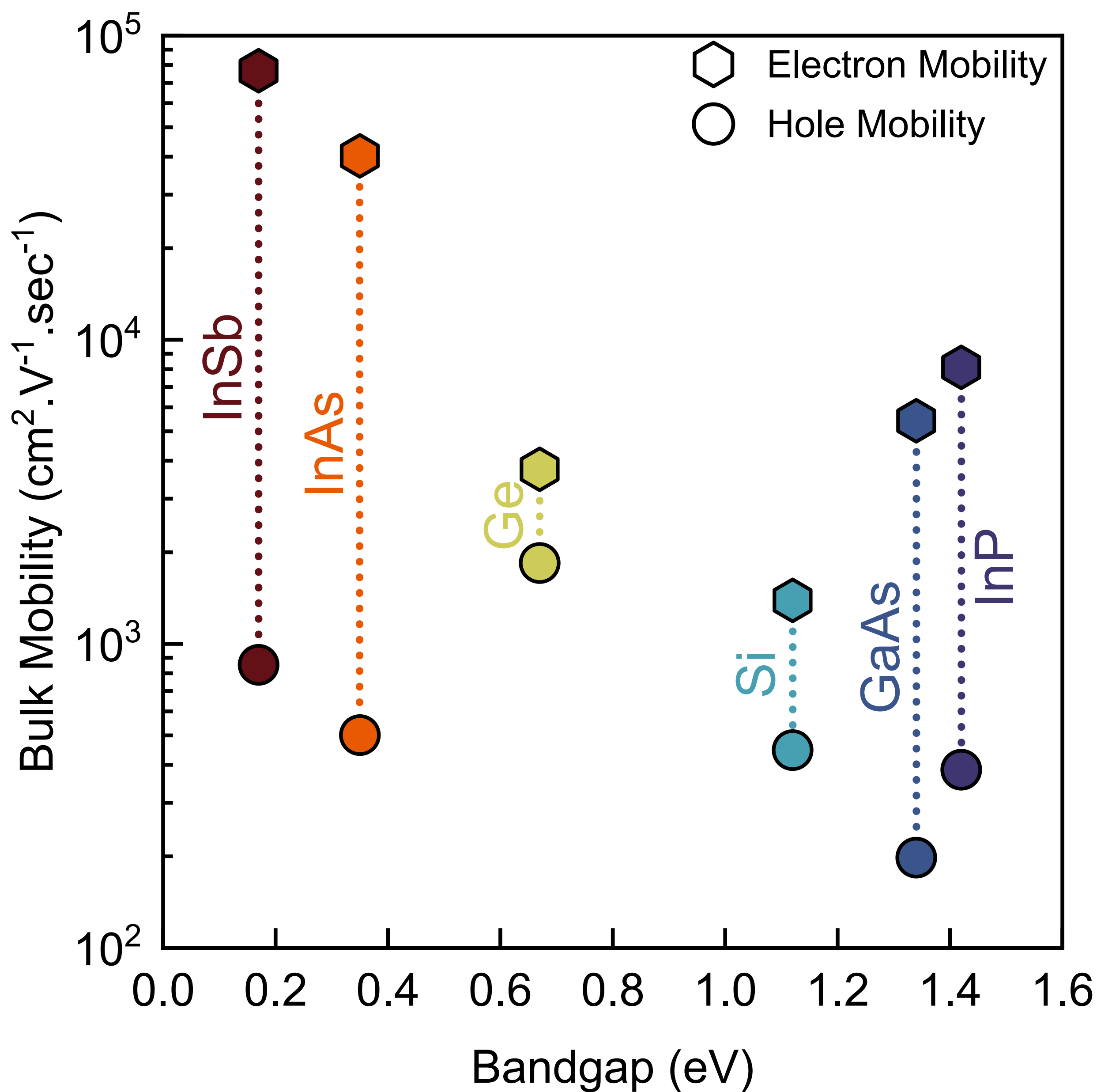

Figure 1.1: Bandgap *vs.* bulk mobility landscape of Si, Ge and common III-V materials. Used with permission of Springer Nature [8].

of electron to hole mobilities (μ_e/μ_h) becomes a paramount consideration to ensure balanced device current drive capabilities and circuit-level complementarities. The mobility ratio threshold should ideally remain below approximately three to prevent excessive performance asymmetry. Inspection of the mobility landscape in Figure 1.1 indicates pronounced disparities between μ_h and μ_e in various III-V semiconductors, primarily attributed to their distinct band structural properties—specifically, the high effective hole masses (m_h^*) associated with the valence band states, which inversely influence μ_h via the relation $\mu_h \propto 1/m_h^*$. These high effective hole masses underpin the significantly lower hole mobilities observed in these materials.

While potential engineering strategies—such as band structure engineering, strain application, or heterostructure design—might mitigate mobility imbalance effects, comprehensive consideration of additional intrinsic and extrinsic material properties is imperative. Notably, III-V semiconductor interfaces often exhibit elevated interface state densities (D_{it}), which are known to detrimentally influence key device parameters, including drive ON-current (I_{ON}), standby leakage (I_{OFF}), threshold voltage stability (V_{th}), subthreshold slope (SS), and subthreshold swing The spatial distribution and energetic density of interface states critically modulate their impact on device reliability, subthreshold characteristics, and overall switching performance.

In contrast, Ge presents a compelling alternative, as evidenced in Figure 1.1, due to its relatively balanced hole and electron mobility, with μ_h approximately fourfold and μ_e roughly double those observed in Si. This near symmetry in charge transport parameters spurred extensive research endeavors [8, 16–35], targeting the elucidation of Ge's fundamental electronic properties and its integration potential into advanced device

architectures. Nonetheless, achieving device-quality Ge films with performance rivaling state-of-the-art silicon remains complex [36–45], as discussed in subsequent sections.

1.4 Application in Photonics: Rise of Silicon Photonics and Germanium for Optical Sources

While the previous section briefly addressed the importance of exploring alternative materials for logic-based electronics, a significant area of current research is focused on Ge and Ge-based optoelectronic devices [42, 46–52]. One critical aspect of electronic devices is the logical performance of transistors, which determines their technological capabilities. However, transistors are typically embedded within complex package solutions, where the active logic elements occupy only a few microns of the entire stack. The majority of the package comprises multiple metallic interconnect layers oriented orthogonally, which facilitate intra- and inter-chip communication. As transistor dimensions are scaled down to enhance logic density, the metal interconnect layers also require miniaturization, particularly within the Back End of Line (BEOL) processing stages.

Reducing the size of these interconnects—commonly made of copper—introduces challenges such as increased heat generation and parasitic impedance, which can lead to signal delays [53, 54]. At higher data transmission frequencies, issues like signal crosstalk and attenuation further compromise signal integrity. The transition from 2D to 3D CMOS architecture has exacerbated heat dissipation challenges, as the decreased surface area limits thermal management capabilities. Consequently, the industry has adopted

multi-core processors with intra-chip communication channels to mitigate heat-related issues, though this approach increases architectural complexity. Nonetheless, these strategies serve as interim solutions, underscoring the need for innovative approaches to overcome copper's performance limitations.

Simultaneously, there is a growing demand for higher bandwidths driven by the proliferation of electronic devices. Data centers, in particular, invest billions annually to manage heating as they process vast amounts of information, often reaching zettabyte scale. Among the proposed solutions, transitioning from electronic to photonic communication represents a promising avenue [54, 55]. Researchers have demonstrated the advantages of optical interconnects for intra- and inter-chip data transfer and within data centers [56–58]. Photons, as information carriers, possess neither charge nor mass, enabling significant improvements in heat management, signal integrity, and transmission delays. However, one of the major challenges remains the development of efficient, high-performance, low-threshold, monolithically integrated optical sources—a critical component that is currently lacking [59]. Recent advancements have showcased integrated on-chip communication, although these demonstrations often rely on external optical sources [60]. III-V semiconductor materials are known for their high radiative recombination efficiency, and heterogeneous integration of III-V lasers onto silicon substrates presents an attractive alternative [61]. Some recent developments highlight the potential benefits of this approach [62–64]; however, the complexity associated with hetero-integration within existing silicon CMOS manufacturing processes limits practical adoption [61]. Therefore, a key innovation for advancing both electronic and photonic applications is the development of a silicon CMOS-compatible, monolithically integrated

group-IV laser.

Si is the inevitable primary candidate for CMOS-compatible photonic source integration due to its well-characterized semiconducting properties established since the inception of semiconductor technology. However, intrinsic limitations stem from its electronic band structure, specifically the lack of a local conduction band minimum at the Γ point, resulting in an indirect bandgap [46, 50, 65]. Effective realization of Si-based lasers necessitates leveraging quantum confinement effects—such as in nanostructures—to modify the electronic states and facilitate radiative recombination predominantly via the X valley [65]. As an indirect bandgap material, Si exhibits inherently low radiative recombination efficiency, impeding optical gain. While Si waveguides provide efficient optical confinement and guiding, the indirect transition mechanism restricts net optical amplification. Furthermore, interface coupling losses continue to limit device efficiency and output power. Consequently, Ge, despite its indirect bandgap nature, has become increasingly attractive for integrated optoelectronic applications, owing to its compatibility with Si CMOS infrastructure and potential for bandgap engineering to enhance optical emission characteristics [65–69].

1.5 Germanium Optical Sources: Strategies and Applications

Although Ge is an indirect bandgap semiconductor, the primary distinction between Si and Ge resides in the energy offset between the conduction band minima. Specifically, the conduction band minimum in Ge, corresponding to the fundamental bandgap, is

located at approximately 0.67 eV above the valence band maximum at the L point along the ⟨111⟩ crystallographic direction. Additionally, Ge exhibits a local conduction band minimum at the Γ point ($\vec{k} = 0$ in the $\vec{E} vs. \vec{k}$ diagram) with an energy approximately 140 meV higher than the L-point minimum. This intrinsic bandstructure characteristic endows Ge with significant potential for transition to a direct bandgap configuration through targeted bandstructure engineering and other modulation techniques. Substantial research has explored methods to achieve a direct bandgap in Ge, primarily via (i) structural modifications such as application of uniaxial or biaxial tensile strain [70–78], alloying with Sn (tin) to form GeSn alloys [51, 79–82], and the fabrication of engineered nanostructures [79, 83–90], and (ii) electronic doping strategies, including heavy n-doping to modify the band occupation and transition probabilities [91–93]. Recent experimental demonstrations have successfully achieved lasing in Ge-based heterostructures through individual or combination of these band engineering approaches. Crucially, integration of Ge into existing silicon CMOS fabrication processes is highly feasible, as silicon-germanium ($Si_{1-x}Ge_x$) alloys are already employed since previous CMOS nodes [4]. Therefore, transitioning to Ge-based components is unlikely to necessitate substantial modifications to current semiconductor manufacturing infrastructure.

Mechanical stress applied to Ge epilayers causes deformation of the crystal lattice, which can be related to the change in band structure via deformation potentials governed by the deformation potential theory [94, 95]. The expected band structure differs with application of different types of strain—uniaxial/biaxial/triaxial compressive/tensile—and typically requires computational models to predict the effect. Particularly for uniaxial/biaxial tensile

strained Ge, the different deformation rates of the L and Γ valleys in the conduction band, with the latter being faster [96], permits the reduction of the energy difference between L and Γ valleys, $\Delta E_{\Gamma \to L} \approx 140meV$, leading to the transformation from an indirect to a direct bandgap material. Theoretical frameworks estimate different levels of uniaxial and biaxial tensile strain (≃1.5%) for this transformation, also known as '*crossover point*' [76]. Mechanical tensile strain also affects the valence band of Ge, splitting the light-hole (LH) and heavy hole (HH) bands in a way that the LH band is displaced upward and HH band is displaced downward [95, 97]. It is immediately evident that implementation of such high levels of tensile strain requires precise and robust growth techniques to avoid introduction of defects in the epilayers. The upcoming section briefly discusses the importance of maintaining crystalline quality and the pressing need for improving material quality to realize Ge-based optical sources.

1.6 Minority Carrier Lifetime as a Metric for Material Quality

With tensile-strained Ge established as a strong replacement of Si in emerging electronic and photonic applications, we turn our attention to the key to realizing Ge integration – the growth of high-fidelity tensile strained crystalline Ge epilayers. One of the key parameters that can be used as quick determinant for material quality is minority carrier lifetime; epilayers characterized by defects and disorder will exhibit degraded lifetime, and vice versa. While compressively-strained Ge on Si1-xGex buffers has received fair amount of investigation in the past, comparatively less research efforts

have been undertaken regarding the material quality and carrier dynamics in ε-Ge/InGaAs, ε-Ge/InAlAs and III-V/IV/III-V material systems. Notably, this gap in literature can be attributed to the extensive list of challenges which include (i) controlling InAs alloy concentration in the InGaAs or InAlAs strain templates such that desired tensile strain is achieved without exceeding the critical layer thickness, h_c, [98, 99] (ii) engineering atomically abrupt IV/III-V and III-V/IV/III-V heterointerfaces where elevated temperatures for growth almost always result in hetero-interfacial diffusion, (iii) antiphase boundaries (APDs) stemming from polar III-V growth on non-polar IV [100], and (iv) non-uniform buffer relaxation dynamics and its implications on the active epilayer [101–105]. For these reasons, this research work utilizes solid-source molecular beam epitaxy (MBE) for the pseudomorphic growth of ε-Ge/InGaAs, ε-Ge/InAlAs, InGaAs/ ε-Ge/InGaAs and heavy boron-doped ε-Ge/InGaAs, with the aim to enhance the understanding of these material systems. Although further details are provided regarding the relationship between material quality and effective carrier lifetime, τ_{eff}, in the subsequent chapters, a rudimentary description is provided here as a precursor to the succeeding discussion.

Ge epitaxial films typically exhibit poor lifetime compared to its bulk counterpart, which can be attributed to poor film quality riddled with defects [106–108]. Poor carrier lifetimes directly affect the performance of device operation and impose a performance bottleneck. Defects in materials, in all their forms and location within the film, act as strong Shockley-Read-Hall (SRH) recombination centers, participating in trapping and emission of carriers. By computational modeling, it has been shown that a defect-limited lifetime, τ_{SRH}, needs to be at least 100 ns in order to fully utilize the benefits of strain [109]. The importance

of this requirement comes from the fact that [110]:

$$\frac{1}{\tau_{eff}} = \frac{1}{\tau_{radiative}} + \frac{1}{\tau_{non-radiative}} \tag{1.1}$$

Consequently, τ_{eff} becomes limited by $\tau_{non-radiative}$ in defective epitaxial films, affecting device performance. The non-radiative part in Eqn (1.1), in general, consists of two primary components, SRH recombination statistics and Auger recombination statistics. SRH recombination is the fundamental process by which excess carriers, electrons and holes, generated inside a semiconductor material recombine at defect states, impurity states or trap states which have dedicated energy levels within the bandgap of the semiconductor material. Multiple phonons are required to achieve this recombination process. Consequently, the energy that is released when a carrier recombines non-radiatively by SRH recombination is dissipated in the form of heat. On the other hand, this dissipated energy may also be captured by another carrier, where the third carrier can lose its excess energy non-radiatively to thermal vibrations or phonons. This modification of the SRH recombination is called Auger recombination. Auger recombination typically becomes important for highly doped, near degenerate semiconductors, and has been neglected in this work, given the carrier density is below the threshold for Auger recombination in the samples studied. The primary carrier dynamics is then governed by SRH recombination statistics. Notably, since every semiconductor material is *defective*, SRH recombination is active in all cases. It then becomes apparent that improving material crystallinity would suppress the non-radiative SRH recombination and enhance the radiative component.

1.7 Aim of this Work and Dissertation Outline

The purpose of this body of work is to provide a comprehensive understanding of ε-Ge grown via III-V metamorphic buffers, namely InGaAs and InAlAs, with respect to material quality, and assess the viability of achieving high levels of strain while maintaining crystallinity of the material for application in emerging electronic and photonic applications. This dissertation is aimed at comprehensive understanding of (i) design and systematic structural characterization of ε-Ge/InGaAs, ε-Ge/InAlAs, InGaAs/ε-Ge/InGaAs heterostructures, including buffer strain relaxation, epilayer strain state, surface morphology and material crystallinity, (ii) impact of strain on the active Ge epilayers and (iii) understanding the impact of doping in the presence of tensile strain on active Ge epilayers, with the common lens of carrier dynamics in each heterostructure. This body of work should provide a systematic understanding of this material system and guide the development and advancement of future electronic and photonic devices.

Chapter 1 discusses the relevance of Ge and ε-Ge in the context of electronic and photonic applications, while summarizing the necessity of improving material quality to enhance device performance.

Chapter 2 presents a systematic investigation of the design and materials characterization of *unstrained* Ge grown on GaAs via AlAs as an intermediate buffer, and ε-Ge grown via InGaAs metamorphic buffers with various levels of strain imparted to the Ge epilayers. High-resolution x-ray diffraction measurements were performed to identify the strain levels present within the ε-Ge epilayers. The heterointerface quality, coherence, abruptness and crystallinity was further investigated using cross-sectional

high-resolution transmission electron microscopy for different levels of tensile strain imparted to Ge. Finally, the carrier dynamics in the *unstrained* and ε-Ge epilayers was systematically investigated using microwave-reflectance photoconductance decay measurements.

Chapter 3 is an extension of Chapter 2, where a systematic comparative investigation is carried out to assess the viability and efficacy of strain templates for Ge, namely InAlAs and InGaAs buffers. A similar approach to Chapter 2 is followed here, with extensive materials design and characterization of the strain state and buffer relaxation properties of ε-Ge/InGaAs and ε-Ge/InAlAs using high-resolution x-ray diffraction and corroborating the findings using Raman spectroscopy. Additionally, the surface morphology, which is a direct lens for relaxation during growth, is investigated using atomic force microscopy. This chapter provides key metrics for the determination of the superior buffer for imparting strain to Ge epilayers. Furthermore, drawing from our previous works, we investigate the feasibility of InGaAs overlayer growth as a means to emulate separate confinement heterostructures for application in developing Ge-based optical sources. Finally, the carrier dynamics of each heterostructure is investigated using microwave-reflectance photoconductance decay measurements to study the effective lifetime.

Chapter 4 discusses an important aspect of tailoring semiconductor materials to specific applications – doping. In this chapter, systematic investigation of in-situ heavy boron doping of *unstrained* and ε-Ge/InGaAs heterostructures is undertaken, and to the best of the author's knowledge, is the first investigative work performed on heavy boron doping of ε-Ge epilayers. The chapter starts with a strain state estimation of ε-Ge

epilayers by high-resolution x-ray diffraction measurements, followed by the heterostructure coherence, abruptness and defect morphology investigation by cross-sectional high-resolution transmission electron microscopy. Using microwave-reflectance photoconductance decay measurements, carrier dynamics is studied and provides key insights into the effects of heavy doping incorporation in ε-Ge epilayers. Finally, the observations are independently investigated using atomistic modeling, which provides important conclusions and pathways for incorporating heavy doping in ε-Ge epilayers.

Finally, Chapter 5 provides a brief summary of the key findings in this body of work and highlights the key takeaways, while outlining future prospects and avenues of research.

Bibliography

[1] G. E. Moore, "Cramming More Components onto Integrated Circuits," *Proceedings of the IEEE*, vol. 86, no. 1, pp. 82–85, 1998, ISSN: 1558-2256. DOI: 10.1109/JPROC.1998.658762.

[2] T. Ghani, M. Armstrong, C. Auth, M. Bost, P. Charvat, G. Glass, T. Hoffmann, K. Johnson, C. Kenyon, J. Klaus, B. McIntyre, K. Mistry, A. Murthy, J. Sandford, M. Silberstein, S. Sivakumar, P. Smith, K. Zawadzki, S. Thompson, and M. Bohr, "A 90nm High Volume Manufacturing Logic Technology Featuring Novel 45nm Gate Length Strained Silicon Cmos Transistors," in *IEEE International Electron Devices Meeting 2003*, pp. 11.6.1–11.6.3. DOI: 10.1109/IEDM.2003.1269442.

[3] K. Mistry, C. Allen, C. Auth, B. Beattie, D. Bergstrom, M. Bost, M. Brazier, M. Buehler, A. Cappellani, R. Chau, C.-H. Choi, G. Ding, K. Fischer, T. Ghani, R. Grover, W. Han, D. Hanken, M. Hattendorf, J. He, J. Hicks, R. Huessner, D. Ingerly, P. Jain, R. James, L. Jong, S. Joshi, C. Kenyon, K. Kuhn, K. Lee, H. Liu, J. Maiz, B. McIntyre, P. Moon, J. Neirynck, S. Pae, C. Parker, D. Parsons, C. Prasad, L. Pipes, M. Prince, P. Ranade, T. Reynolds, J. Sandford, L. Shifren, J. Sebastian, J. Seiple, D. Simon, S. Sivakumar, P. Smith, C. Thomas, T. Troeger, P. Vandervoorn, S. Williams, and K. Zawadzki, "A 45nm Logic Technology with High-k+Metal Gate Transistors, Strained Silicon, 9 Cu Interconnect Layers, 193nm Dry Patterning, and 100% Pb-free Packaging," in *2007 IEEE International Electron Devices Meeting*, 2007, pp. 247–250. DOI: 10.1109/IEDM.2007.4418914.

[4] C. Auth, C. Allen, A. Blattner, D. Bergstrom, M. Brazier, M. Bost, M. Buehler, V. Chikarmane, T. Ghani, T. Glassman, R. Grover, W. Han, D. Hanken, M. Hattendorf, P. Hentges, R. Heussner, J. Hicks, D. Ingerly, P. Jain, S. Jaloviar, R. James, D. Jones, J. Jopling, S. Joshi, C. Kenyon, H. Liu, R. McFadden, B. McIntyre, J. Neirynck, C. Parker, L. Pipes, I. Post, S. Pradhan, M. Prince, S. Ramey, T. Reynolds, J. Roesler, J. Sandford, J. Seiple, P. Smith, C. Thomas, D. Towner, T. Troeger, C. Weber, P. Yashar, K. Zawadzki, and K. Mistry, "A 22nm High Performance and Low-Power Cmos Technology Featuring Fully-Depleted Tri-Gate Transistors, Self-Aligned Contacts and High Density Mim Capacitors," in *2012 Symposium on VLSI Technology (VLSIT)*, IEEE, Jun. 2012, pp. 131–132, ISBN: 2158-9682. DOI: 10.1109/vlsit.2012.6242496.

[5] R. Chau, B. Doyle, S. Datta, J. Kavalieros, and K. Zhang, "Integrated Nanoelectronics for the Future," *Nature Materials*, vol. 6, no. 11, pp. 810–812, Nov. 2007, ISSN: 1476-4660. DOI: 10.1038/nmat2014.

[6] M. T. Bohr and I. A. Young, "CMOS Scaling Trends and Beyond," *IEEE Micro*, vol. 37, no. 6, pp. 20–29, Nov. 2017, ISSN: 0272-1732. DOI: 10.1109/mm.2017.4241347.

[7] A. P. Jacob, R. Xie, M. G. Sung, L. Liebmann, R. T. P. Lee, and B. Taylor, "Scaling Challenges for Advanced CMOS Devices," *International Journal of High Speed Electronics and Systems*, vol. 26, no. 01n02, p. 1 740 001, 2017. DOI: 10.1142/s0129156417400018.

[8] R. Pillarisetty, “Academic and Industry Research Progress in Germanium Nanodevices,” *Nature*, vol. 479, no. 7373, pp. 324–328, Nov. 2011, ISSN: 1476-4687. DOI: 10.1038/nature10678.

[9] J. A. del Alamo, “Nanometre-Scale Electronics with III–V Compound Semiconductors,” *Nature*, vol. 479, no. 7373, pp. 317–323, 2011, ISSN: 1476-4687. DOI: 10.1038/nature10677.

[10] R. Chau, S. Datta, and A. Majumdar, “Opportunities and Challenges of III-V Nanoelectronics for Future High-Speed, Low-Power Logic Applications,” in *IEEE Compound Semiconductor Integrated Circuit Symposium, 2005. CSIC ’05.*, IEEE, 2005, 4 pp. ISBN: 2374-8443. DOI: 10.1109/csics.2005.1531740.

[11] S. Takagi, R. Zhang, J. Suh, S.-H. Kim, M. Yokoyama, K. Nishi, and M. Takenaka, “III–V/Ge Channel MOS Device Technologies in Nano CMOS Era,” *Japanese Journal of Applied Physics*, vol. 54, no. 6S1, 06FA01, 2015, ISSN: 1347-4065 0021-4922. DOI: 10.7567/JJAP.54.06FA01.

[12] M. Heyns, A. Alian, G. Brammertz, M. Caymax, Y. C. Chang, L. K. Chu, B. D. Jaeger, G. Eneman, F. Gencarelli, G. Groeseneken, G. Hellings, A. Hikavyy, T. Y. Hoffmann, M. Houssa, C. Huyghebaert, D. Leonelli, D. Lin, R. Loo, W. Magnus, C. Merckling, M. Meuris, J. Mitard, L. Nyns, T. Orzali, R. Rooyackers, S. Sioncke, B. Soree, X. Sun, A. Vandooren, A. S. Verhulst, B. Vincent, N. Waldron, G. Wang, W. E. Wang, and L. Witters, “Advancing CMOS beyond the Si Roadmap with Ge and III/V Devices,” in *2011 International Electron Devices Meeting*, pp. 13.1.1–13.1.4, ISBN: 2156-017X. DOI: 10.1109/IEDM.2011.6131543.

[13] D. H. Kim and J. A. d. Alamo, “30-nm InAs PHEMTs with $f_T = 644\ GHz$ and $f_{max} = 681\ GHz$,” *IEEE Electron Device Letters*, vol. 31, no. 8, pp. 806–808, Aug. 2010, ISSN: 1558-0563. DOI: 10.1109/LED.2010.2051133.

[14] D.-H. Kim, J. A. del Alamo, P. Chen, W. Ha, M. Urteaga, and B. Brar, “50-nm E-mode $In_{0.7}Ga_{0.3}As$ PHEMTs on 100-nm InP substrate with $f_{max} > 1$ THz,” in *2010 International Electron Devices Meeting*, IEEE, Dec. 2010, pp. 30.6.1–30.6.4, ISBN: 2156-017X. DOI: 10.1109/iedm.2010.5703453.

[15] A. Leuther, S. Koch, A. Tessmann, I. Kallfass, T. Merkle, H. Massler, R. Loesch, M. Schlechtweg, S. Saito, and O. Ambacher, “20 nm Metamorphic HEMT with 660 GHz f_T,” in *IPRM 2011 - 23rd International Conference on Indium Phosphide and Related Materials*, IEEE, 2012, pp. 1–4, ISBN: 1092-8669. DOI: 10.1109/iciprm.2012.6403365.

[16] K. L. Wang and P. V. Gray, “Fabrication and Characterization of Germanium ion implanted IGFET’s,” *IEEE Transactions on Electron Devices*, vol. 22, no. 6, pp. 353–355, 1975, ISSN: 0018-9383. DOI: 10.1109/t-ed.1975.18137.

[17] S. C. Martin, L. M. Hitt, and J. J. Rosenberg, “p-channel Germanium mosfets with High Channel Mobility,” *IEEE Electron Device Letters*, vol. 10, no. 7, pp. 325–326, 1989, ISSN: 0741-3106. DOI: 10.1109/55.29667.

[18] M. L. Lee, C. W. Leitz, Z. Cheng, A. J. Pitera, T. Langdo, M. T. Currie, G. Taraschi, E. A. Fitzgerald, and D. A. Antoniadis, “Strained Ge channel p-type metal–oxide–semiconductor field-effect transistors grown on $Si_1 - xGex/Si$ virtual substrates,” *Applied Physics Letters*, vol. 79, no. 20, pp. 3344–3346, 2001, ISSN: 0003-6951. DOI: 10.1063/1.1417515.

[19] C. Chi On, K. Hyoungsub, D. Chi, B. B. Triplett, P. C. McIntyre, and K. C. Saraswat, “A sub-400°C Germanium MOSFET Technology with high-κ dielectric and metal gate,” in *Digest. International Electron Devices Meeting*, pp. 437–440. DOI: 10.1109/IEDM.2002.1175872.

[20] B. J. Cho, C. H. Huang, M. Y. Yang, A. Chin, W. Chen, C. Zhu, and M. F. Li, “Very low defects and high performance Ge On Insulator p MOSFETs with Al2O3 gate dielectrics,” in *Symposium on VLSI Technology*, Japan Soc. Applied Phys, pp. 119–120. DOI: 10.1109/vlsit.2003.1221114.

[21] E. Kasper and S. Heim, “Challenges of High Ge Content Silicon Germanium Structures,” *Applied surface science*, vol. 224, no. 1-4, pp. 3–8, 2004, ISSN: 0169-4332. DOI: 10.1016/j.apsusc.2003.08.022.

[22] S. J. Whang, S. J. Lee, G. Fei, W. Nan, C. X. Zhu, P. Ji Sheng, T. Lei Jun, and D. L. Kwong, “Germanium p- & n-MOSFETs fabricated with novel surface passivation (plasma-PH_3 and thin AlN) and TaN/HfO_2 gate stack,” in *IEDM Technical Digest. IEEE International Electron Devices Meeting, 2004.*, pp. 307–310. DOI: 10.1109/IEDM.2004.1419140.

[23] T. Krishnamohan, Z. Krivokapic, K. Uchida, Y. Nishi, and K. C. Saraswat, “Low defect ultra-thin fully strained-Ge MOSFET on relaxed Si with high mobility and low band-to-band-tunneling (BTBT),” in *Digest of Technical Papers. 2005 Symposium on VLSI Technology, 2005.*, pp. 82–83, ISBN: 2158-9682. DOI: 10.1109/.2005.1469221.

[24] O. Weber, Y. Bogumilowicz, T. Ernst, J. M. Hartmann, F. Ducroquet, F. Andrieu, C. Dupre, L. Clavelier, C. L. Royer, N. Cherkashin, M. Hytch, D. Rouchon, H.

Dansas, A. M. Papon, V. Carron, C. Tabone, and S. Deleonibus, “Strained Si and Ge MOSFETs with high-κ/metal gate stack for high mobility dual channel CMOS,” in *IEEE InternationalElectron Devices Meeting, 2005. IEDM Technical Digest.*, pp. 137–140, ISBN: 2156-017X. DOI: 10.1109/IEDM.2005.1609288.

[25] C. O. Chui, F. Ito, and K. C. Saraswat, “Nanoscale Germanium MOS dielectrics Part I: Germanium oxynitrides,” *IEEE Transactions on Electron Devices*, vol. 53, no. 7, pp. 1501–1508, 2006, ISSN: 0018-9383. DOI: 10.1109/ted.2006.875808.

[26] C. O. Chui, H. Kim, D. Chi, P. C. McIntyre, and K. C. Saraswat, “Nanoscale germanium MOS Dielectrics Part II high-κ /gate dielectrics,” *IEEE Transactions on Electron Devices*, vol. 53, no. 7, pp. 1509–1516, 2006, ISSN: 0018-9383. DOI: 10.1109/ted.2006.875812.

[27] K. Saraswat, C. O. Chui, T. Krishnamohan, D. Kim, A. Nayfeh, and A. Pethe, “High Performance Germanium MOSFETSs,” *Materials Science and Engineering: B*, vol. 135, no. 3, pp. 242–249, 2006, ISSN: 0921-5107. DOI: 10.1016/j.mseb.2006.08.014.

[28] D. Kuzum, A. J. Pethe, T. Krishnamohan, Y. Oshima, Y. Sun, J. P. McVittie, P. A. Pianetta, P. C. McIntyre, and K. C. Saraswat, “Interface-Engineered Ge (100) and (111), N- and P-FETs with High Mobility,” in *2007 IEEE International Electron Devices Meeting*, pp. 723–726, ISBN: 2156-017X. DOI: 10.1109/IEDM.2007.4419048.

[29] Y. Kamata, “High-K/Ge MOSFETsfor Future Nanoelectronics,” *Materials Today*, vol. 11, no. 1, pp. 30–38, 2008, ISSN: 1369-7021. DOI: 10.1016/S1369-7021(07)70350-4.

[30] J. Mitard, B. De Jaeger, F. E. Leys, G. Hellings, K. Martens, G. Eneman, D. P. Brunco, R. Loo, J. C. Lin, D. Shamiryan, T. Vandeweyer, G. Winderickx, E. Vrancken, C. H. Yu, K. De Meyer, M. Caymax, L. Pantisano, M. Meuris, and M. M. Heyns, "Record ION/IOFF performance for 65nm Ge pMOSFET and novel Si passivation scheme for improved EOT scalability," in *2008 IEEE International Electron Devices Meeting*, 2008, pp. 1–4. DOI: 10.1109/IEDM.2008.4796837.

[31] L. Gomez, C. N. Chléirigh, P. Hashemi, and J. L. Hoyt, "Enhanced Hole Mobility in High Ge Content Asymmetrically Strained-SiGe p-MOSFETs," *IEEE Electron Device Letters*, vol. 31, no. 8, pp. 782–784, 2010, ISSN: 1558-0563. DOI: 10.1109/LED.2010.2050574.

[32] R. Pillarisetty, B. Chu-Kung, S. Corcoran, G. Dewey, J. Kavalieros, H. Kennel, R. Kotlyar, V. Le, D. Lionberger, M. Metz, N. Mukherjee, J. Nah, W. Rachmady, M. Radosavljevic, U. Shah, S. Taft, H. Then, N. Zelick, and R. Chau, "High mobility strained germanium quantum well field effect transistor as the p-channel device option for low power ($V_c c = 0.5$ V) III–V CMOS architecture," in *2010 International Electron Devices Meeting*, pp. 6.7.1–6.7.4, ISBN: 2156-017X. DOI: 10.1109/IEDM.2010.5703312.

[33] R. Zhang, T. Iwasaki, N. Taoka, M. Takenaka, and S. Takagi, "High mobility Ge pMOSFETs with nm thin EOT using $Al_2O_3/GeO_x/Ge$ gate stacks fabricated by plasma post oxidation," in *2011 Symposium on VLSI Technology - Digest of Technical Papers*, IEEE, 2012, pp. 56–57, ISBN: 2158-9682. DOI: 10.1109/vlsit.2012.6242511.

[34] Q. Xie, S. Deng, M. Schaekers, D. Lin, M. Caymax, A. Delabie, X.-P. Qu, Y.-L. Jiang, D. Deduytsche, and C. Detavernier, "Germanium surface passivation and atomic layer deposition of high-κ dielectrics—a tutorial review on Ge-based MOS capacitors," *Semiconductor Science and Technology*, vol. 27, no. 7, p. 074 012, 2012, ISSN: 0268-1242. DOI: 10.1088/0268-1242/27/7/074012.

[35] A. Toriumi and T. Nishimura, "Germanium CMOS potential from material and process perspectives: Be more positive about Germanium," *Japanese Journal of Applied Physics*, vol. 57, no. 1, p. 010 101, Oct. 2017. DOI: 10.7567/JJAP.57.010101.

[36] E. A. Fitzgerald, Y.-H. Xie, M. L. Green, D. Brasen, A. R. Kortan, J. Michel, Y.-J. Mii, and B. E. Weir, "Totally relaxed GexSi1-x layers with low threading dislocation densities grown on Si substrates," *Applied Physics Letters*, vol. 59, no. 7, pp. 811–813, 1991, ISSN: 0003-6951. DOI: 10.1063/1.105351.

[37] L. Colace, G. Masini, F. Galluzzi, G. Assanto, G. Capellini, L. Di Gaspare, E. Palange, and F. Evangelisti, "Metal–semiconductor–metal near-infrared light detector based on epitaxial Ge/Si," *Applied Physics Letters*, vol. 72, no. 24, pp. 3175–3177, 1998, ISSN: 0003-6951. DOI: 10.1063/1.121584.

[38] M. T. Currie, S. B. Samavedam, T. A. Langdo, C. W. Leitz, and E. A. Fitzgerald, "Controlling threading dislocation densities in Ge on Si using graded SiGe layers and chemical-mechanical polishing," *Applied Physics Letters*, vol. 72, no. 14, pp. 1718–1720, 1998, ISSN: 0003-6951. DOI: 10.1063/1.121162.

[39] H.-C. Luan, D. R. Lim, K. K. Lee, K. M. Chen, J. G. Sandland, K. Wada, and L. C. Kimerling, "High-quality Ge epilayers on Si with low threading-dislocation

densities," *Applied Physics Letters*, vol. 75, no. 19, pp. 2909–2911, 1999, ISSN: 0003-6951. DOI: 10.1063/1.125187.

[40] J. L. Liu, S. Tong, Y. H. Luo, J. Wan, and K. L. Wang, "High-quality Ge films on Si substrates using Sb surfactant-mediated graded SiGe buffers," *Applied Physics Letters*, vol. 79, no. 21, pp. 3431–3433, 2001, ISSN: 0003-6951. DOI: 10.1063/1.1421092.

[41] A. Nayfeh, C. O. Chui, K. C. Saraswat, and T. Yonehara, "Effects of hydrogen annealing on heteroepitaxial-Ge layers on Si: Surface roughness and electrical quality," *Applied Physics Letters*, vol. 85, no. 14, pp. 2815–2817, 2004, ISSN: 0003-6951. DOI: 10.1063/1.1802381.

[42] J. Michel, J. Liu, and L. C. Kimerling, "High-performance Ge-on-Si photodetectors," *Nature Photonics*, vol. 4, no. 8, pp. 527–534, 2010, ISSN: 1749-4893. DOI: 10.1038/nphoton.2010.157.

[43] V. A. Shah, A. Dobbie, M. Myronov, and D. R. Leadley, "Reverse graded SiGe/Ge/Si buffers for high-composition virtual substrates," *Journal of Applied Physics*, vol. 107, no. 6, 2010, ISSN: 0021-8979. DOI: 10.1063/1.3311556.

[44] J. Liu, R. Camacho-Aguilera, J. T. Bessette, X. Sun, X. Wang, Y. Cai, L. C. Kimerling, and J. Michel, "Ge-on-Si optoelectronics," *Thin Solid Films*, vol. 520, no. 8, pp. 3354–3360, 2012, ISSN: 0040-6090. DOI: 10.1016/j.tsf.2011.10.121.

[45] J. Liu, L. C. Kimerling, and J. Michel, "Monolithic Ge-on-Si lasers for large-scale electronic–photonic integration," *Semiconductor Science and Technology*, vol. 27, no. 9, p. 094 006, 2012, ISSN: 0268-1242. DOI: 10.1088/0268-1242/27/9/094006.

[46] R. Soref, "The Past, Present, and Future of Silicon Photonics," *IEEE Journal of Selected Topics in Quantum Electronics*, vol. 12, no. 6, pp. 1678–1687, 2006, ISSN: 1558-4542. DOI: 10.1109/JSTQE.2006.883151.

[47] E. Kasper, M. Kittler, M. Oehme, and T. Arguirov, "Germanium tin: silicon photonics toward the mid-infrared [Invited]," *Photonics Research*, vol. 1, no. 2, pp. 69–76, Jul. 2013, ISSN: 2327-9125. DOI: 10.1364/PRJ.1.000069.

[48] P. Chaisakul, D. Marris-Morini, J. Frigerio, D. Chrastina, M.-S. Rouifed, S. Cecchi, P. Crozat, G. Isella, and L. Vivien, "Integrated Germanium Optical Interconnects on Silicon Substrates," *Nature Photonics*, vol. 8, no. 6, pp. 482–488, 2014, ISSN: 1749-4893. DOI: 10.1038/nphoton.2014.73.

[49] J. Liu, "Monolithically Integrated Ge-on-Si Active Photonics," *Photonics*, vol. 1, no. 3, pp. 162–197, 2014, ISSN: 2304-6732. DOI: 10.3390/photonics1030162.

[50] G. T. Reed, G. Z. Mashanovich, F. Y. Gardes, D. J. Thomson, Y. Hu, J. Soler-Penades, M. Nedeljkovic, A. Khokar, P. Thomas, C. Littlejohns, A. Ahmad, S. Reynolds, R. Topley, C. Mitchell, S. Stankovic, P. R. Wilson, L. Ke, T. M. B. Masaud, A. Tarazona, and H. Chong, "Silicon Photonics," in *2014 7th International Silicon-Germanium Technology and Device Meeting (ISTDM)*, pp. 5–6. DOI: 10.1109/ISTDM.2014.6874661.

[51] S. Wirths, R. Geiger, N. von den Driesch, G. Mussler, T. Stoica, S. Mantl, Z. Ikonic, M. Luysberg, S. Chiussi, J. M. Hartmann, H. Sigg, J. Faist, D. Buca, and D. Grützmacher, "Lasing in direct-bandgap GeSn alloy grown on Si," *Nature Photonics*, vol. 9, no. 2, pp. 88–92, 2015, ISSN: 1749-4893. DOI: 10.1038/nphoton.2014.321.

[52] V. Reboud, A. Gassenq, J. M. Hartmann, J. Widiez, L. Virot, J. Aubin, K. Guilloy, S. Tardif, J. M. Fédéli, N. Pauc, A. Chelnokov, and V. Calvo, "Germanium Based Photonic Components toward a Full Silicon/Germanium Photonic Platform," *Progress in Crystal Growth and Characterization of Materials*, vol. 63, no. 2, pp. 1–24, 2017, ISSN: 0960-8974. DOI: 10.1016/j.pcrysgrow.2017.04.004.

[53] D. A. B. Miller, "Rationale and challenges for optical interconnects to electronic chips," *Proceedings of the IEEE*, vol. 88, no. 6, pp. 728–749, 2000, ISSN: 1558-2256. DOI: 10.1109/5.867687.

[54] D. A. B. Miller, "Optical interconnects to electronic chips," *Applied Optics*, vol. 49, no. 25, F59–F70, 2010. DOI: 10.1364/AO.49.000F59.

[55] K. Saraswat, C. Hoyeol, P. Kapur, and K. Kyung-Hoae, "Performance comparison between copper, carbon nanotube, and optical interconnects," in *2008 IEEE International Symposium on Circuits and Systems (ISCAS)*, pp. 2781–2784, ISBN: 2158-1525. DOI: 10.1109/ISCAS.2008.4542034.

[56] M. R. Feldman, S. C. Esener, C. C. Guest, and S. H. Lee, "Comparison between optical and electrical interconnects based on power and speed considerations," *applied optics*, vol. 27, no. 9, pp. 1742–1751, 1988, ISSN: 1559-128X. DOI: 10.1364/ao.27.001742.

[57] J. Shin, C.-S. Seo, A. Chellappa, M. Brooke, A. Chatterjee, and N. Jokerst, "Comparison of electrical and optical interconnect," in *Electronic Components and Technology Conference*, IEEE, pp. 1067–1072, ISBN: 0569-5503. DOI: 10.1109/ectc.2003.1216422.

[58] C. Hoyeol, P. Kapur, and K. C. Saraswat, “Power comparison between high-speed electrical and optical interconnects for interchip communication,” *Journal of Lightwave Technology*, vol. 22, no. 9, pp. 2021–2033, 2004, ISSN: 1558-2213. DOI: 10.1109/JLT.2004.833531.

[59] S. Saito, K. Oda, T. Takahama, K. Tani, and T. Mine, “Germanium fin light-emitting diode,” *Applied Physics Letters*, vol. 99, no. 24, 2011, ISSN: 0003-6951. DOI: 10.1063/1.3670053.

[60] C. Sun, M. T. Wade, Y. Lee, J. S. Orcutt, L. Alloatti, M. S. Georgas, A. S. Waterman, J. M. Shainline, R. R. Avizienis, S. Lin, B. R. Moss, R. Kumar, F. Pavanello, A. H. Atabaki, H. M. Cook, A. J. Ou, J. C. Leu, Y.-H. Chen, K. Asanović, R. J. Ram, M. A. Popović, and V. M. Stojanović, “Single-chip microprocessor that communicates directly using light,” *Nature*, vol. 528, no. 7583, pp. 534–538, 2015, ISSN: 1476-4687. DOI: 10.1038/nature16454.

[61] D. A. B. Miller, “Hybrid SEED-massively parallel optical interconnections for silicon ICs,” in *Proceedings of Second International Workshop on Massively Parallel Processing Using Optical Interconnections*, pp. 2–7. DOI: 10.1109/MPPOI.1995.528621.

[62] H. Guan, A. Novack, T. Galfsky, Y. Ma, S. Fathololoumi, A. Horth, T. N. Huynh, J. Roman, R. Shi, M. Caverley, Y. Liu, T. Baehr-Jones, K. Bergman, and M. Hochberg, “Widely-tunable, narrow-linewidth III-V/silicon hybrid external-cavity laser for coherent communication,” *Optics Express*, vol. 26, no. 7, pp. 7920–7933, 2018. DOI: 10.1364/OE.26.007920.

[63] B. Szelag, K. Hassan, L. Adelmini, E. Ghegin, P. Rodriguez, F. Nemouchi, P. Brianceau, E. Vermande, A. Schembri, D. Carrara, P. Cavalié, F. Franchin, M. C. Roure, L. Sanchez, C. Jany, and S. Olivier, "Hybrid III–V/Silicon Technology for Laser Integration on a 200-mm Fully CMOS-Compatible Silicon Photonics Platform," *IEEE Journal of Selected Topics in Quantum Electronics*, vol. 25, no. 5, pp. 1–10, 2019, ISSN: 1558-4542. DOI: 10.1109/JSTQE.2019.2904445.

[64] W.-Q. Wei, A. He, B. Yang, Z.-H. Wang, J.-Z. Huang, D. Han, M. Ming, X. Guo, Y. Su, J.-J. Zhang, and T. Wang, "Monolithic integration of embedded III-V lasers on SOI," *Light: Science & Applications*, vol. 12, no. 1, p. 84, 2023, ISSN: 2047-7538. DOI: 10.1038/s41377-023-01128-z.

[65] S. Saito, F. Y. Gardes, A. Z. Al-Attili, K. Tani, K. Oda, Y. Suwa, T. Ido, Y. Ishikawa, S. Kako, S. Iwamoto, and Y. Arakawa, "Group IV Light Sources to Enable the Convergence of Photonics and Electronics," *Frontiers in Materials*, vol. Volume 1 - 2014, 2014, ISSN: 2296-8016. DOI: 10.3389/fmats.2014.00015.

[66] J. Liu, X. Sun, R. Camacho-Aguilera, L. C. Kimerling, and J. Michel, "Ge-on-Si laser operating at room temperature," *Optics Letters*, vol. 35, no. 5, pp. 679–681, 2010. DOI: 10.1364/OL.35.000679.

[67] R. E. Camacho-Aguilera, Y. Cai, N. Patel, J. T. Bessette, M. Romagnoli, L. C. Kimerling, and J. Michel, "An electrically pumped germanium laser," *Optics express*, vol. 20, no. 10, pp. 11 316–11 320, 2012, ISSN: 1094-4087. DOI: 10.1364/iprsn.2012.im3a.4.

[68] Y. Ishikawa and S. Saito, "Ge-on-Si photonic devices for photonic-electronic integration on a Si platform," *IEICE Electronics Express*, vol. 11, no. 24, pp. 20 142 008–20 142 008, 2014, ISSN: 1349-2543. DOI: 10.1587/elex.11.20142008.

[69] S. Saito, A. Z. Al-Attili, K. Oda, and Y. Ishikawa, "Towards monolithic integration of germanium light sources on silicon chips," *Semiconductor Science and Technology*, vol. 31, no. 4, p. 043 002, 2016, ISSN: 0268-1242. DOI: 10.1088/0268-1242/31/4/043002.

[70] R. Jakomin, M. d. Kersauson, M. E. Kurdi, L. Largeau, O. Mauguin, G. Beaudoin, S. Sauvage, R. Ossikovski, G. Ndong, M. Chaigneau, I. Sagnes, and P. Boucaud, "High quality tensile-strained n-doped germanium thin films grown on InGaAs buffer layers by metal-organic chemical vapor deposition," *Applied Physics Letters*, vol. 98, no. 9, p. 091 901, 2011. DOI: 10.1063/1.3559231.

[71] S. Gupta, B. Magyari-Köpe, Y. Nishi, and K. C. Saraswat, "Achieving direct band gap in germanium through integration of Sn alloying and external strain," *Journal of Applied Physics*, vol. 113, no. 7, 2013, ISSN: 0021-8979. DOI: 10.1063/1.4792649.

[72] N. Pavarelli, T. J. Ochalski, F. Murphy-Armando, Y. Huo, M. Schmidt, G. Huyet, and J. S. Harris, "Optical Emission of a Strained Direct-Band-Gap Ge Quantum Well Embedded Inside InGaAs Alloy Layers," *Physical Review Letters*, vol. 110, no. 17, p. 177 404, 2013, PRL. DOI: 10.1103/PhysRevLett.110.177404.

[73] M. Virgilio, C. L. Manganelli, G. Grosso, G. Pizzi, and G. Capellini, "Radiative recombination and optical gain spectra in biaxially strained n-type germanium,"

Physical Review B, vol. 87, no. 23, p. 235 313, 2013, PRB. DOI: 10.1103/PhysRevB.87.235313.

[74] D. S. Sukhdeo, D. Nam, J.-H. Kang, M. L. Brongersma, and K. C. Saraswat, "Direct bandgap germanium-on-silicon inferred from 5.7% ⟨100⟩ uniaxial tensile strain [Invited]," *Photonics Research*, vol. 2, no. 3, A8–A13, 2014. DOI: 10.1364/PRJ.2.0000A8.

[75] M. Clavel, D. Saladukha, P. S. Goley, T. J. Ochalski, F. Murphy-Armando, R. J. Bodnar, and M. K. Hudait, "Heterogeneously-Grown Tunable Tensile Strained Germanium on Silicon for Photonic Devices," *ACS Applied Materials & Interfaces*, vol. 7, no. 48, pp. 26 470–26 481, 2015, ISSN: 1944-8244. DOI: 10.1021/acsami.5b07385.

[76] D. Saladukha, M. B. Clavel, F. Murphy-Armando, G. Greene-Diniz, M. Grüning, M. K. Hudait, and T. J. Ochalski, "Direct and indirect band gaps in Ge under biaxial tensile strain investigated by photoluminescence and photoreflectance studies," *Physical Review B*, vol. 97, no. 19, p. 195 304, 2018, PRB. DOI: 10.1103/PhysRevB.97.195304.

[77] Q. Chen, L. Zhang, Y. Song, X. Chen, S. Koelling, Z. Zhang, Y. Li, P. M. Koenraad, J. Shao, C. S. Tan, S. Wang, and Q. Gong, "Highly Tensile-Strained Self-Assembled Ge Quantum Dots on InP Substrates for Integrated Light Sources," *ACS Applied Nano Materials*, vol. 4, no. 1, pp. 897–906, 2021. DOI: 10.1021/acsanm.0c03373.

[78] M. K. Hudait, F. Murphy-Armando, D. Saladukha, M. B. Clavel, P. S. Goley, D. Maurya, S. Bhattacharya, and T. J. Ochalski, "Design, Theoretical, and Experimental Investigation of Tensile-Strained Germanium Quantum-Well Laser

Structure," *ACS Applied Electronic Materials*, vol. 3, no. 10, pp. 4535–4547, 2021. DOI: 10.1021/acsaelm.1c00660.

[79] V. Reboud, A. Gassenq, N. Pauc, J. Aubin, L. Milord, Q. M. Thai, M. Bertrand, K. Guilloy, D. Rouchon, J. Rothman, T. Zabel, F. A. Pilon, H. Sigg, A. Chelnokov, J. M. Hartmann, and V. Calvo, "Optically pumped GeSn micro-disks with 16% Sn lasing at 3.1 μm up to 180K," *Applied Physics Letters*, vol. 111, no. 9, p. 092 101, 2017. DOI: 10.1063/1.5000353.

[80] J. Margetis, S. Al-Kabi, W. Du, W. Dou, Y. Zhou, T. Pham, P. Grant, S. Ghetmiri, A. Mosleh, B. Li, J. Liu, G. Sun, R. Soref, J. Tolle, M. Mortazavi, and S.-Q. Yu, "Si-Based GeSn Lasers with Wavelength Coverage of 2–3 μm and Operating Temperatures up to 180 K," *ACS Photonics*, vol. 5, no. 3, pp. 827–833, 2018. DOI: 10.1021/acsphotonics.7b00938.

[81] J. Chrétien, N. Pauc, F. A. Pilon, M. Bertrand, Q.-M. Thai, L. Casiez, N. Bernier, H. Dansas, P. Gergaud, E. Delamadeleine, R. Khazaka, H. Sigg, J. Faist, A. Chelnokov, V. Reboud, J.-M. Hartmann, and V. Calvo, "Gesn lasers covering a wide wavelength range thanks to uniaxial tensile strain," *ACS photonics*, vol. 6, no. 10, pp. 2462–2469, 2019, ISSN: 2330-4022. DOI: 10.1021/acsphotonics.9b00712.

[82] Y. Zhou, Y. Miao, S. Ojo, H. Tran, G. Abernathy, J. M. Grant, S. Amoah, G. Salamo, W. Du, and J. Liu, "Electrically injected GeSn lasers on Si operating up to 100 K," *Optica*, vol. 7, no. 8, pp. 924–928, 2020, ISSN: 2334-2536. DOI: 10.1364/optica.395687.

[83] J. R. Jain, A. Hryciw, T. M. Baer, D. A. B. Miller, M. L. Brongersma, and R. T. Howe, "A micromachining-based technology for enhancing germanium light

emission via tensile strain," *Nature Photonics*, vol. 6, no. 6, pp. 398–405, 2012, ISSN: 1749-4893. DOI: 10.1038/nphoton.2012.111.

[84] M. J. Süess, R. Geiger, R. A. Minamisawa, G. Schiefler, J. Frigerio, D. Chrastina, G. Isella, R. Spolenak, J. Faist, and H. Sigg, "Analysis of enhanced light emission from highly strained germanium microbridges," *Nature Photonics*, vol. 7, no. 6, pp. 466–472, 2013, ISSN: 1749-4893. DOI: 10.1038/nphoton.2013.67.

[85] A. Ghrib, M. El Kurdi, M. Prost, S. Sauvage, X. Checoury, G. Beaudoin, M. Chaigneau, R. Ossikovski, I. Sagnes, and P. Boucaud, "All-Around SiN Stressor for High and Homogeneous Tensile Strain in Germanium Microdisk Cavities," *Advanced Optical Materials*, vol. 3, no. 3, pp. 353–358, 2015, ISSN: 2195-1071. DOI: 10.1002/adom.201400369.

[86] A. Gassenq, S. Tardif, K. Guilloy, G. O. Dias, N. Pauc, I. Duchemin, D. Rouchon, J.-M. Hartmann, J. Widiez, J. Escalante, Y.-M. Niquet, R. Geiger, T. Zabel, H. Sigg, J. Faist, A. Chelnokov, F. Rieutord, V. Reboud, and V. Calvo, "Accurate strain measurements in highly strained Ge microbridges," *Applied Physics Letters*, vol. 108, no. 24, p. 241 902, 2016. DOI: 10.1063/1.4953788.

[87] R. W. Millar, K. Gallacher, J. Frigerio, A. Ballabio, A. Bashir, I. MacLaren, G. Isella, and D. J. Paul, "Analysis of Ge micro-cavities with in-plane tensile strains above 2%," *Optics Express*, vol. 24, no. 5, pp. 4365–4374, 2016. DOI: 10.1364/OE.24.004365.

[88] P. Zhou, X. Xu, S. Matsushita, K. Sawano, and T. Maruizumi, "Resonant light emission from uniaxially tensile-strained Ge microbridges," *Japanese Journal of*

Applied Physics, vol. 57, no. 4S, 04FH10, 2018, ISSN: 1347-4065. DOI: 10.7567/jjap.57.04fh10.

[89] F. T. Armand Pilon, A. Lyasota, Y. M. Niquet, V. Reboud, V. Calvo, N. Pauc, J. Widiez, C. Bonzon, J. M. Hartmann, A. Chelnokov, J. Faist, and H. Sigg, "Lasing in strained Germanium Microbridges," *Nature Communications*, vol. 10, no. 1, p. 2724, 2019, Armand Pilon, F T Lyasota, A Niquet, Y-M Reboud, V Calvo, V Pauc, N Widiez, J Bonzon, C Hartmann, J M Chelnokov, A Faist, J Sigg, H eng Research Support, Non-U.S. Gov't England 2019/06/22 Nat Commun. 2019 Jun 20;10(1):2724. doi: 10.1038/s41467-019-10655-6., ISSN: 2041-1723 (Electronic) 2041-1723 (Linking). DOI: 10.1038/s41467-019-10655-6.

[90] S. Qin, J. Sun, J. Jiang, Y. Zhang, M. Cheng, L. Yu, K. Wang, L. Kai, H. Shi, and Q. Huang, "Monolithic integrated emitting-detecting configuration based on strained Ge microbridge," *Nanophotonics*, vol. 10, no. 11, pp. 2847–2857, 2021, ISSN: 2192-8614. DOI: 10.1515/nanoph-2021-0122.

[91] X. Sun, J. Liu, L. C. Kimerling, and J. Michel, "Toward a germanium laser for integrated silicon photonics," *IEEE Journal of Selected Topics in Quantum Electronics*, vol. 16, no. 1, pp. 124–131, 2009, ISSN: 1077-260X. DOI: 10.1109/jstqe.2009.2027445.

[92] H. Wen and E. Bellotti, "Rigorous theory of the radiative and gain characteristics of silicon and germanium lasing media," *Physical Review B*, vol. 91, no. 3, p. 035 307, 2015, ISSN: 1098-0121. DOI: 10.1103/physrevb.91.035307.

[93] S. Bao, D. Kim, C. Onwukaeme, S. Gupta, K. Saraswat, K. H. Lee, Y. Kim, D. Min, Y. Jung, and H. Qiu, "Low-threshold optically pumped lasing in highly strained

germanium nanowires," *Nature communications*, vol. 8, no. 1, p. 1845, 2017, ISSN: 2041-1723. DOI: 10.1038/s41467-017-02026-w.

[94] C. G. Van de Walle, "Band lineups and deformation potentials in the model-solid theory," *Physical review B*, vol. 39, no. 3, p. 1871, 1989, ISSN: 0163-1829. DOI: 10.1103/physrevb.39.1871.

[95] M. E. Kurdi, G. Fishman, S. Sauvage, and P. Boucaud, "Band structure and optical gain of tensile-strained germanium based on a 30 band $\vec{k} \cdot \vec{p}$ formalism," *Journal of Applied Physics*, vol. 107, no. 1, p. 013 710, 2010. DOI: 10.1063/1.3279307.

[96] M. El Kurdi, H. Bertin, E. Martincic, M. de Kersauson, G. Fishman, S. Sauvage, A. Bosseboeuf, and P. Boucaud, "Control of direct band gap emission of bulk germanium by mechanical tensile strain," *Applied Physics Letters*, vol. 96, no. 4, 2010, ISSN: 0003-6951. DOI: 10.1063/1.3297883.

[97] C. Boztug, J. R. Sánchez-Pérez, F. Cavallo, M. G. Lagally, and R. Paiella, "Strained-Germanium Nanostructures for Infrared Photonics," *ACS nano*, vol. 8, no. 4, pp. 3136–3151, 2014, ISSN: 1936-0851. DOI: 10.1021/nn404739b.

[98] J. W. Matthews and A. E. Blakeslee, "Defects in epitaxial multilayers: I. Misfit dislocations," *Journal of Crystal Growth*, vol. 27, pp. 118–125, 1974, ISSN: 0022-0248. DOI: 10.1016/S0022-0248(74)80055-2.

[99] R. People and J. C. Bean, "Calculation of critical layer thickness versus lattice mismatch for Ge_xSi_{1-x}/Si strained-layer heterostructures," *Applied Physics Letters*, vol. 47, no. 3, pp. 322–324, 1985, ISSN: 0003-6951. DOI: 10.1063/1.96206.

[100] H. Kroemer, “Polar-on-nonpolar epitaxy,” *Journal of Crystal Growth*, vol. 81, no. 1-4, pp. 193–204, 1987, ISSN: 0022-0248. DOI: 10.1016/0022-0248(87)90391-5.

[101] G. Whaley and P. Cohen, “Relaxation of strained InGaAs during molecular beam epitaxy,” *Applied physics letters*, vol. 57, no. 2, pp. 144–146, 1990, ISSN: 0003-6951. DOI: 10.1063/1.103966.

[102] C. W. Snyder, B. G. Orr, D. Kessler, and L. M. Sander, “Effect of strain on surface morphology in highly strained InGaAs films,” *Physical review letters*, vol. 66, no. 23, p. 3032, 1991, ISSN: 0031-9007. DOI: 10.1103/physrevlett.66.3032.

[103] R. S. Goldman, H. H. Wieder, and K. L. Kavanagh, “Correlation of anisotropic strain relaxation with substrate misorientation direction at InGaAs/GaAs (001) interfaces,” *Applied physics letters*, vol. 67, no. 3, pp. 344–346, 1995, ISSN: 0003-6951. DOI: 10.1063/1.115439.

[104] R. S. Goldman, K. L. Kavanagh, H. H. Wieder, S. N. Ehrlich, and R. M. Feenstra, “Effects of GaAs substrate misorientation on strain relaxation in $In_xGa_{1-x}As$ films and multilayers,” *Journal of Applied Physics*, vol. 83, no. 10, pp. 5137–5149, 1998, ISSN: 0021-8979. DOI: 10.1063/1.367331.

[105] M. K. Hudait, Y. Lin, and S. A. Ringel, “Strain relaxation properties of $InAs_yP_{1-y}$ metamorphic materials grown on InP substrates,” *Journal of Applied Physics*, vol. 105, no. 6, 2009, ISSN: 0021-8979. DOI: 10.1063/1.3098232.

[106] J. J. Sheng, D. Leonhardt, S. M. Han, S. W. Johnston, J. G. Cederberg, and M. S. Carroll, “Empirical correlation for minority carrier lifetime to defect density profile in germanium on silicon grown by nanoscale interfacial engineering,” *Journal of*

Vacuum Science & Technology B, vol. 31, no. 5, p. 051 201, 2013. DOI: 10.1116/1.4816488.

[107] R. Geiger, J. Frigerio, M. J. Süess, D. Chrastina, G. Isella, R. Spolenak, J. Faist, and H. Sigg, "Excess Carrier Lifetimes in Ge Layers on Si," *Applied Physics Letters*, vol. 104, no. 6, p. 062 106, 2014. DOI: 10.1063/1.4865237.

[108] D. Nam, J.-H. Kang, M. L. Brongersma, and K. C. Saraswat, "Observation of Improved Minority Carrier Lifetimes in High-Quality Ge-On-Insulator Using Time-Resolved Photoluminescence," *Optics Letters*, vol. 39, no. 21, pp. 6205–6208, 2014. DOI: 10.1364/ol.39.006205.

[109] D. S. Sukhdeo, S. Gupta, K. C. Saraswat, B. Dutt, and D. Nam, "Impact of minority carrier lifetime on the performance of strained Germanium light sources," *Optics Communications*, vol. 364, pp. 233–237, 2016, (Raj), ISSN: 0030-4018. DOI: 10.1016/j.optcom.2015.11.060.

[110] D. K. Schroder, *Semiconductor Material and Device Characterization*. John Wiley & Sons, 2015, ISBN: 0471739065. DOI: 10.1002/0471749095.

This page left intentionally blank

Chapter 2:

Interplay between Strain and Thickness on Effective Carrier Lifetime of Buffer Mediated Epitaxial Germanium probed by Photoconductance Decay Technique

The following chapter has been reproduced from Ref. **S. Bhattacharya, S. W. Johnston, S. Datta, and M. K. Hudait, "Interplay Between Strain and Thickness on the Effective Carrier Lifetime of Buffer-Mediated Epitaxial Germanium Probed by the Photoconductance Decay Technique,"** ***ACS Applied Electronic Materials*****, vol. 5, no. 6, pp. 3190–3197, May 2023, ISSN: 2637-6113. DOI:** 10.1021/acsaelm.3c00256 *with minor changes* [1]. The author acknowledges epitaxial growth facilitation by M. Clavel, and S. W. Johnston for photoconductance decay measurements.

We report contactless effective minority carrier lifetime of epitaxially grown ***unstrained*** **and in-plane ⟨110⟩ biaxially tensile strained (001)**

germanium (ε-Ge) epilayers measured using microwave-reflectance photoconductance decay measurements. Strained Ge epilayers were grown using In$_x$Ga$_{1-x}$As linearly-graded buffers on (001) GaAs substrates. Using homogeneous excitation of *unstrained* Ge epilayers, thickness-dependent separation of minority carrier lifetime components under low injection conditions yielded bulk lifetime of 114 $\pm$ 2 ns and low surface recombination velocity of 21.3 $\pm$ 0.04 cm/s. More notably, effective minority carrier lifetime (τ_{eff}) of $>$100 ns from sub-50 nm 1.6% tensile strained Ge epilayers showed no degradation relative to the *unstrained* counterpart. Detailed material characterization using x-ray diffractometry revealed successful strain transfer of 0.61% and 0.89% to the Ge epilayers *via* In$_x$Ga$_{1-x}$As metamorphic buffers and confirm pseudomorphic growth. Lattice coherence observed at the ε-Ge epilayer and In$_x$Ga$_{1-x}$As buffer heterointerfaces *via* transmission electron microscopy substantiate the prime material quality achieved. The relatively high carrier lifetimes achieved are an indicator of excellent material quality and provide a path forward to realize low-threshold Ge laser sources.

2.1 Introduction

The demand for high-speed large-bandwidth communication capabilities is a direct consequence of the increasing accessibility of computational devices. With the capabilities of traditional copper interconnects nearing performance saturation due to aggressive down-scaling, researchers have been seeking optical alternatives for low-power, cost-efficient intra- and inter-chip communication [2–5]. Extensive research efforts have been attempted to realize silicon (Si)-based monolithically integrated optoelectronic circuits alongside concurrent complementary metal-oxide-semiconductor (CMOS) electronics [6]. However, the widespread adoption of Si-based optoelectronics is limited by its inherent indirect bandgap that inhibits radiative efficiency [7]. On the other hand, there is a simultaneous need for a paradigm shift to higher mobility channel materials for the upcoming technology nodes as the performance limits of Si-based electronic devices are nearing a saturation point [8]. III-V materials have been investigated heavily in the past few decades and exhibit superior electron mobility and optical properties owing to low electron effective mass and direct bandgaps, respectively [9]. However, due to the sheer nature of CMOS devices where both n-channel and p-channel MOS devices are required to implement current electronic circuits, III-V materials offer little advantage over Si owing to the stark disparity in the electron and hole mobilities, with the hole mobility being several times lower than the electron mobility [9]. It is therefore imperative to find a suitable material choice that can act as a common bridge between electronic and optical devices [10, 11]. This is where germanium (Ge), another group-IV element, with its pseudo-direct bandgap and excellent compatibility with the current Si CMOS technology, has garnered serious attention as an alternative for realization of

integrated optical sources [12–16]. Several approaches such as application of uniaxial or biaxial strain engineering [17–20], band structure engineering [14, 21], tin (Sn) alloying [22–25], and recently demonstrated micro-disk and nanomembrane structures [26–29] have been researched to achieve direct bandgap Ge and Ge1-ySny, potentially showing promise for enhanced radiative properties. Despite the promising benefits, epitaxial Ge-on-Si is still typically characterized by high defect density and consequently suffers from poor defect-limited carrier lifetimes which hovers in the range of only a few tens of nanoseconds [18, 30, 31]. This has an adverse effect on the radiative emission efficiency and hinders progress in realization of low-threshold Ge optical sources. Improving material quality is thus imperative to ensure taking advantage of the aforementioned techniques to unlock enhanced emission capabilities [32].

In this work, we employ the ability of III-V metamorphic buffers to transfer variable strain to group-IV epitaxial thin-films while maintaining prime epitaxial quality [33–35]. We use solid-source molecular beam epitaxy (MBE) to demonstrate precise strain transfer *via* $In_xGa_{1\text{-}x}As$ metamorphic linearly graded buffer (LGB) stressor to achieve pseudomorphic epitaxy of in-plane $\langle 110 \rangle$ biaxially tensile strained Ge (ε-Ge) on typical (001) GaAs substrates. Exceptional crystallinity of the non-capped Ge epilayers with imparted strain of 0.61% and 0.89% is verified by high-resolution x-ray diffraction (HR-XRD) analyses, devoid of short- and long-order defects as evidenced by cross-sectional high-resolution transmission electron microscopy (HR-XTEM). Furthermore, we use non-contact microwave-reflectance photoconductance decay (μ-PCD) technique to probe the effective minority carrier lifetime, an important performance merit for material quality, of the ε-Ge epilayers alongside *unstrained*

Ge/AlAs/GaAs as control. We find, using thickness-dependent separation of lifetime components, a respectable bulk lifetime (τ_{bulk}) of $\approx$ 114 $\pm$ 2ns and a low surface recombination velocity (S) of $\approx$ 21.3 $\pm$ 0.04cm/sec from the control. Finally, the characteristic lifetime obtained from ε-Ge epilayers show no degradation insomuch that the exhibited lifetimes are similar to the lifetimes of the control of comparable thickness. We anticipate this demonstration of superior strained epitaxy in this work will serve as a path forward towards the goal of realizing low-threshold Ge optical sources.

2.2 Experimental Section

2.2.1 Materials Synthesis

The *unintentionally doped unstrained* and ε-Ge heterostructures studied in this work were grown on epi-ready, semi-insulating (SI) GaAs(001) substrates, with a typical 2° offcut toward $\langle 110 \rangle$, in a dual-chamber solid-source MBE with isolated group III-V and group IV reactors, connected using a transfer chamber kept under ultra-high vacuum. The isolation is intended to minimize the prospect of atomic interdiffusion at the group IV/group III-V heterointerfaces during epitaxial growth at elevated temperatures of the group IV material post group III-V material growth. The progression of the growth runs was monitored at crucial growth phases using an *in-situ* reflection high-energy electron diffraction (RHEED) module housed inside the III-V growth chamber. Prior to each growth run, substrate oxide desorption was performed at elevated temperatures of $\simeq$750°C under an arsenic (As_2) overpressure of $\simeq 10^{-5}$ Torr, and confirmed by clear, long streak

patterns observed on RHEED. Following oxide desorption, each growth run was cooled down to 650°C for a GaAs overgrowth of 250 nm. For the control sample, unstrained Ge/AlAs/GaAs, the GaAs overgrowth was followed by AlAs growth at 650°C. For the ε-Ge/In$_x$Ga$_{1-x}$As heterostructures, the initial GaAs overgrowth was followed by growing linearly-graded In$_x$Ga$_{1-x}$As metamorphic buffers in the range of 400 nm – 550 nm, intended to bridge the lattice mismatch and effectively minimizing defect and dislocation formation and propagation between the ε-Ge/In$_x$Ga$_{1-x}$As heterointerfaces and the GaAs substrate. The In composition in the linearly-graded metamorphic buffer was graded from 3% to 11.5% (0.61% ε-Ge) and 17.3% (0.89% ε-Ge), followed by an overshoot and reverse grading to promote relaxation of the In$_x$Ga$_{1-x}$As virtual substrates (VSs) immediately before growth of 750 nm of the respective constant composition In$_{0.115}$Ga$_{0.885}$As (0.61% ε-Ge) and In$_{0.173}$Ga$_{0.827}$As (0.89% ε-Ge) VSs. Post constant In composition In$_x$Ga$_{1-x}$As VS growth (ε-Ge/In$_x$Ga$_{1-x}$As heterostructures) and AlAs growth (unstrained Ge/AlAs/GaAs), and cooling to 150°C under As$_2$ overpressure, the substrates were transferred to the group IV growth chamber *via* the transfer chamber kept under ultra-high vacuum. Finally, epitaxial Ge growth was achieved at 400°C at a growth rate of 0.067 Å/sec for varied durations to achieve the heterostructures studied in this work, and the labeled schematics of these heterostructures are shown in Figures 2.1(a)-(c). We previously reported comprehensive details of the material synthesis scheme elsewhere [36].

2.2.2 Materials Characterization

Ex-situ symmetric (004) $\omega - 2\theta$ rocking curves (RCs), and symmetric (004) and asymmetric (115) reciprocal space maps (RSMs) were recorded to investigate the

crystallinity of the *unstrained* and ε-Ge heterostructures, indium (In) composition in the $In_xGa_{1-x}As$ VSs and the strain state of the Ge epilayers in the strained heterostructures. These scans were recorded on a PANalytical X'Pert Pro diffractometer equipped with a monochromatic Cu Kα_1 (λ = 1.540597 Å) x-ray source, and PIXcel and proportional detectors. Due to the angular proximity of the diffraction maxima from the epilayers in the *unstrained* heterostructure, high-resolution triple-axis configuration was used to record the RCs and RSMs from this sample. Low- and high-resolution bright-field cross-sectional transmission electron micrographs were obtained using a JEOL 2100 system to investigate short- and long-range structural characteristics of the heterostructures and lattice coherence and uniformity at the ε-Ge epilayer and $In_xGa_{1-x}As$ heterointerfaces. Finally, the effective minority carrier lifetimes of the Ge epilayers from each heterostructure were measured using conventional non-contact microwave-reflectance photoconductance decay method (μ-PCD) at the National Renewable Energy Laboratory (NREL) at 300 K. The samples used for measurement were cleaved into 1 cm $\times$ 1 cm pieces and placed below a waveguide (WR42 at 20 GHz, 0.43 cm $\times$ 1.07 cm) facing upward, and subjected to a Q-switched neodymium-doped yttrium aluminum garnet (Nd:YAG) laser source (λ = 1500 nm) with a repetition rate of 10 pulses per second and a pulse width of 5 ns. The laser power was kept constant at 20 mW, measured using a power meter with an absorption disk of 2 cm in diameter. This resulted in a photon flux of the order of $\approx 2 \times 10^{17}$ photons/sec, yielding a low injection level of the order of $\approx 9 \times 10^{13}/cm^3 \cdot sec$. The intensity of the beam flux at the wavelength used for measurement in this work completely fills the waveguide and illuminates majority of the sample area. To prepare the required samples for the thickness-dependent separation of bulk lifetime and surface lifetime components, the

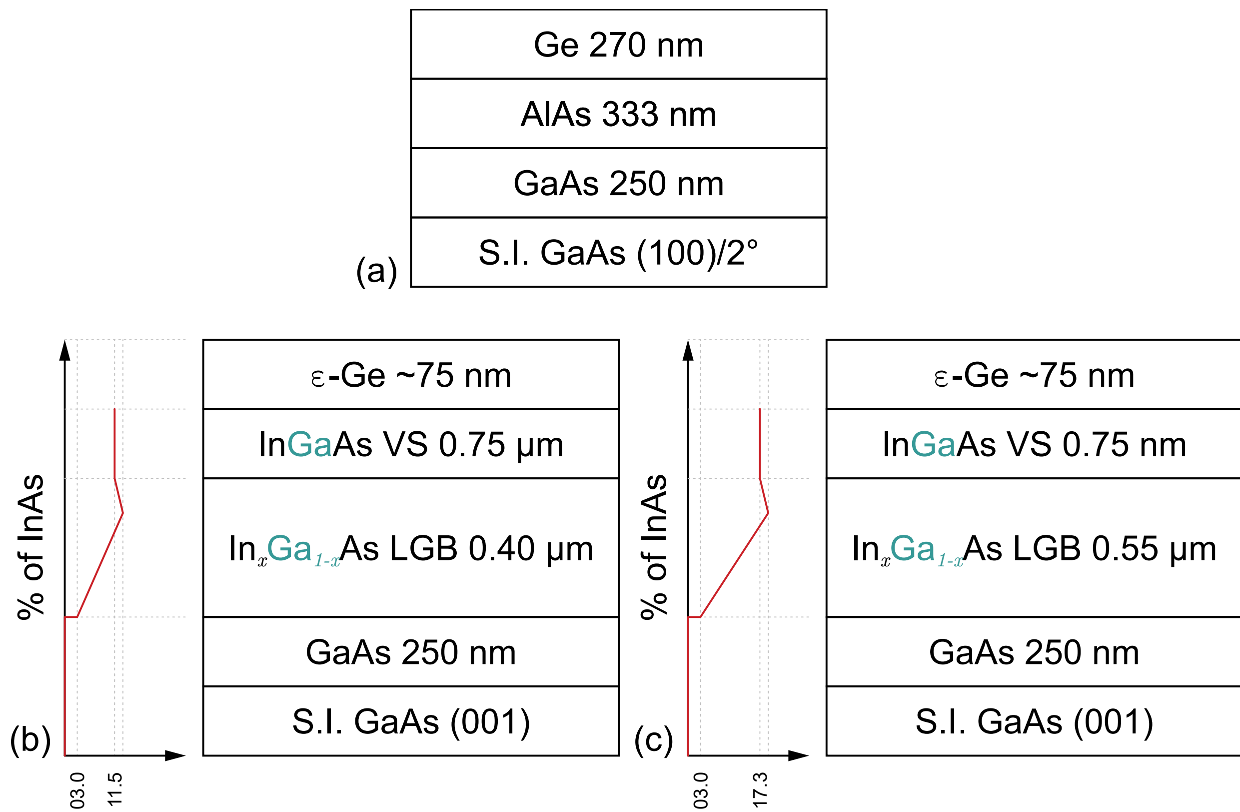

Figure 2.1: Cross sectional schematics of the heterostructures studied in this work, namely (a) *unstrained* Ge/AlAs/GaAs, (b) 0.61% ε-Ge/$In_{0.115}Ga_{0.885}As$, and (c) 0.89% ε-Ge/$In_{0.173}Ga_{0.827}As$.

unstrained Ge/AlAs/GaAs sample was cleaved into several pieces of the aforementioned dimensions. Immediately following a standard de-grease, the sample pieces were treated for varied duration in NH_4OH:H_2O_2:H_2O (1:2:200), exhibiting an etch rate of $\approx$ 2 *nm/sec*, to achieve the desired thicknesses.

2.3 Results and Discussion

2.3.1 Strain Analysis *via* HR-XRD

Figure 2.2(a) shows the ex-situ measured symmetric (004) $\omega - 2\theta$ RCs for the unstrained Ge/AlAs/GaAs, ε-Ge/$In_{0.115}Ga_{0.885}As$ and ε-Ge/$In_{0.173}Ga_{0.827}As$ heterostructures. In the ε-Ge heterostructures, the Ge peaks are shifted toward higher Bragg angles relative to the GaAs substrate peak in line with in-plane tensile strain imparted by the underlying $In_xGa_{1-x}As$ buffers. As such, the intended higher strain transfer is confirmed by the 0.89% ε-Ge epilayer peak appearing at a higher diffraction angle relative to the 0.61% ε-Ge epilayer peak. Staying within the realms of tetragonal distortion, this observation directly translates to a compressed out-of-plane lattice parameter ($a_\perp$) for the ε-Ge epilayers as a result of the imparted strain from the underlying $In_xGa_{1-x}As$ buffer. Similarly, the difference in out-of-plane lattice parameters of the constant In composition $In_xGa_{1-x}As$ VSs manifests as the difference in horizontal angular separation of the $In_xGa_{1-x}As$ peaks relative to the GaAs peak. The humps observed toward the farthest left are contributions from the overshoot In composition in the graded $In_xGa_{1-x}As$ buffers, intended to facilitate relaxation of the $In_xGa_{1-x}As$ VSs.

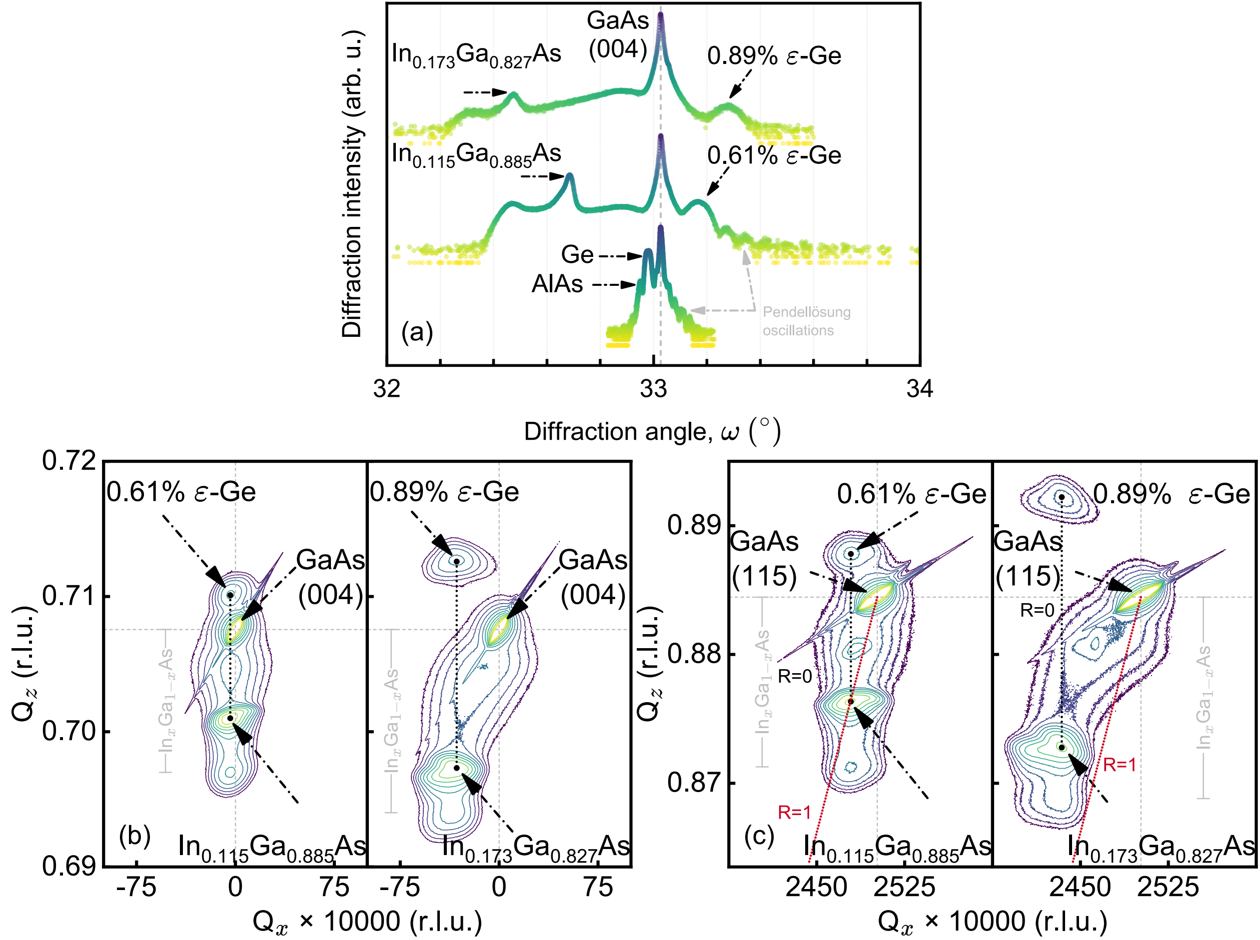

Figure 2.2: (a) Symmetric (004) RC of the *unstrained* and ε-Ge heterostructures, obtained *via* x-ray analysis. Pendellösung oscillations observed clearly in the unstrained and 0.61% ε-Ge epilayer, and partially in the 0.89% ε-Ge epilayer, indicate superior material quality. (b)-(c) Symmetric (004) and asymmetric (115) RSMs of the strained heterostructures, respectively. Here, *r.l.u.* represents reciprocal lattice unit (Å^{-1}). The RLCs for the corresponding layers are labeled accordingly.

Comprehensive quantification of the ε-Ge lattice parameters and In composition in the $In_xGa_{1-x}As$ VSs was done using symmetric (004) and asymmetric (115) RSMs recorded from the ε-Ge/$In_{0.115}Ga_{0.885}As$ and ε-Ge/$In_{0.173}Ga_{0.827}As$ heterostructures, shown in Figure 2.2(b)-(c), respectively. The tensile strain imparted to the Ge epilayers induces a change in the Bragg angle and is evident from the shifted ε-Ge reciprocal lattice centroids (RLC) above the GaAs RLC along Q_z. The difference in imparted strain manifests as difference in vertical angular separation of the Ge RLCs relative to the GaAs substrate RLC as shown in Figures 2.2(b)-(c). Moreover, from the asymmetric (115) RSMs in Figure 2.2(c), it can be observed that the Ge epilayer RLCs are fairly well aligned along Q_x with the corresponding constant In composition $In_xGa_{1-x}As$ VS RLCs. This observation, in conjunction with the symmetry of the centroids along the Q_x and Q_z axes, suggests a coherent strained epitaxy characterized by minimal mosaicity and lattice parameter aberration [33]. Furthermore, from the relatively confined and symmetric $In_xGa_{1-x}As$ RLCs, it can be propounded that the defects owing to lattice mismatch were restricted within the metamorphic $In_xGa_{1-x}As$ LGBs, corroborated by TEM analyses discussed below. The ε-Ge lattice parameters and In composition in the $In_xGa_{1-x}As$ buffer layers were quantified following the process outlined in Ref. [37]. The in-plane strain of a film, $\varepsilon_{\parallel}$, can be expressed as:

$$\varepsilon_{\parallel} = \frac{a_{\parallel} - a_{relaxed}}{a_{relaxed}} \tag{2.1}$$

where $a_{\parallel}$ and $a_{relaxed}$ are the in-plane and relaxed film lattice parameters, respectively. Using the typical value of $a_{relaxed} = 5.658$ Å for Ge, the strain state of the Ge epilayers

were found to be 0.61% and 0.89%, respectively, for the ε-Ge/$In_{0.115}Ga_{0.885}As$ and ε-Ge/$In_{0.173}Ga_{0.827}As$ heterostructures. The quantification of the In composition in the $In_xGa_{1-x}As$ layers and the lattice parameters of the Ge epilayers is presented in Table 2.1. We note here that the accurate analysis of the degree of relaxation of the $In_xGa_{1-x}As$ VSs, specifically in the ε-Ge/$In_{0.173}Ga_{0.827}As$ heterostructure, could be obscured and under-reported in the presence of moderate tilt as observed from symmetric (004) RSMs in Figure 2.2(c), and as such, is not reported here. The relaxed lattice parameters of the ε-Ge epilayers were found to be 5.6597 Å and 5.6570 Å, which are in close alignment with the standard theoretical value of 5.658 Å found in literature. The intended increase in strain transfer from the buffer is evident from the $a_{\parallel}$ ($a_{\perp}$) values from Table 2.1, increasing (decreasing) from 5.6864 Å (5.6329 Å) to 5.7014 Å (5.6127 Å), consistent with biaxial tetragonal distortion of the Ge lattice. It should also be noted that Vegard's law and the calculated relaxed lattice constants were used in conjunction to determine the In composition in the constant composition $In_xGa_{1-x}As$ VSs, as shown in Table 2.1.

Table 2.1: Summary of strain properties of ε-Ge and In composition of $In_xGa_{1-x}As$ VSs extracted from symmetric (004) and asymmetric (115) HR-XRD RSM analyses.

epilayer	lattice parameters			InAs molar fraction	ε
	$a_\perp$	$a_\parallel$	$a_{relaxed}$		
	(Å)	(Å)	(Å)	(%)	(%)
$In_{0.115}Ga_{0.885}As$	5.7065	5.6924	5.6998	11.5	-
ε-Ge	5.6329	5.6864	5.6597	-	0.61
$In_{0.173}Ga_{0.827}As$	5.7369	5.7083	5.7231	17.3	-
ε-Ge	5.6127	5.7014	5.6570	-	0.89

2.3.2 Structural Characterization *via* HR-XTEM

Low- and high-magnification cross-sectional TEM micrographs of the ε-Ge/$In_xGa_{1-x}As$ heterostructures were recorded to gain further insight into the structural quality and lattice coherence across the ε-Ge/$In_xGa_{1-x}As$ heterointerfaces. Figures 2.3(a)-(b) depict the cross-sectional, bright-field, low-magnification TEM micrographs, respectively, of the extended layer stack of the ε-Ge/$In_{0.115}Ga_{0.885}As$ and ε-Ge/$In_{0.173}Ga_{0.827}As$ heterostructures. The relatively thin metamorphic $In_xGa_{1-x}As$ LGBs can be seen to absorb majority of the dislocations within the first few hundreds of nanometers, and as such, the constant composition $In_{0.115}Ga_{0.885}As$ and $In_{0.173}Ga_{0.827}As$ VSs exhibit high-quality growth with minimal defect density, which are undetectable at such low magnification. Figures 2.3(c)-(d) show cross-sectional, bright-field high-magnification TEM micrographs of the ε-Ge/$In_{0.115}Ga_{0.885}As$ and

ε-Ge/$In_{0.173}Ga_{0.827}As$ heterointerfaces, providing a closer look at the heterointerfaces, where no extended defects from the underlying buffer template or microstructural ordering anomaly is observed, revealing a coherent and ordered heterointerface transitioning from the VSs to the active Ge epilayers. Furthermore, the contrast difference arising from the difference in atomic factor of Ge and $In_xGa_{1-x}As$ VSs accentuates the presence of an abrupt heterointerface, suggesting minimal interface interdiffusion. Additionally, noise-filtering Fast Fourier Transform (FFT) method was performed on the visible 45 nm $\times$ 45 nm areas of Figures 2.3(c)-(d), shown in the respective insets, showing the absence of satellite reflections in the resulting diffractograms. This alone indicates that the diffraction points in the respective diffractograms are contributions from a distinct lattice parameter across the entire heterointerface, thus reinforcing the pseudomorphic nature of Ge heteroepitaxy. Not just that, region-wise FFT exclusively computed from 10 nm $\times$ 10 nm areas of the representative regions reiterate the same observation. Figures 2.3(e)-(g) and Figures 2.3(h)-(j) show the representative areas of the respective ε-Ge epilayers, ε-Ge/$In_xGa_{1-x}As$ heterointerfaces and $In_xGa_{1-x}As$ VSs regions indicated by white arrows), where FFT was computed exclusively. The absence of satellite peaks in these diffractograms as well as the vertically aligned diffraction points across the heterointerfaces provide ancillary support for the contribution of a distinct coherent lattice parameter along the length of the heterointerfaces, indicating successful strained pseudomorphic epitaxy, corroborating the preceding XRD analysis.

2.3.3 Material Quality Characterization *via* μ-PCD

The defect-limited carrier lifetime (τ_{eff}), dominated by Shockley-Read-Hall (SRH) carrier dynamics, is strongly dependent on material quality. As such, materials with high defect density exhibit poor carrier lifetime due to the loss of carriers to these defects [30, 38]. To that end, the effective minority carrier lifetimes of the unintentionally doped Ge epilayers in the heterostructures studied in this work were analyzed using the conventional non-contact μ-PCD method. Being a *non-contact* characterization technique, it circumvents the effects of microfabrication steps and performs as a diagnostic tool in material analysis in the early stages of device research [39–41]. Additionally, this technique facilitates probing the dynamics of minority carriers deep inside the bulk, where bulk recombination processes dominate the observed lifetime, thus providing exclusive insight into the material quality [42]. Excess photocarriers, generated when subjecting an optical source onto a sample, induce a change in the local conductance of the material. On removal of the source, these excess carriers return to their pre-illumination, quiescent equilibrium state *via* multiple recombination processes. Recording this change in local conductance using a microwave source probe over time yields a decay transient, characterizing the decay of excess carrier concentration, which constitutes a summation of infinite modes, $\boldsymbol{m}$, where each mode contributes a characteristic lifetime, τ_m, to the overall lifetime [43]. Luke and Cheng [44] worked out the analytical solutions of the carrier dynamics within a semiconducting material in response to interaction with an optical source, under low-level injection. The authors showed that the higher order terms in the lifetime expression disappear rapidly post removal of the source [44]. The effective lifetime, τ_{eff}, is then dominated by the principal

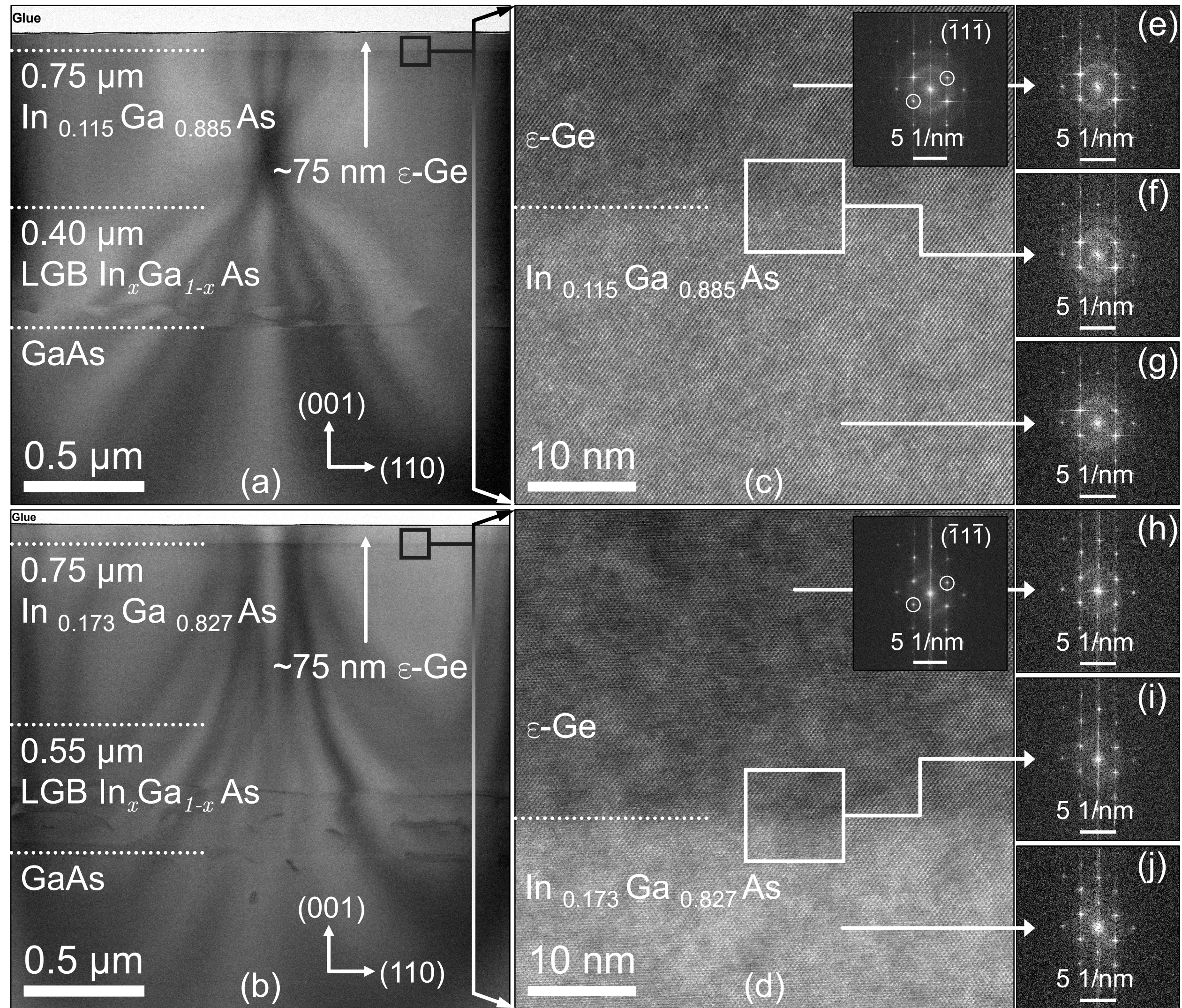

Figure 2.3: Low-magnification cross-sectional bright-field TEM micrographs obtained from (a) ε-Ge/$In_{0.115}Ga_{0.885}As$ and (b) ε-Ge/$In_{0.173}Ga_{0.827}As$ heterostructures, respectively, showing the extended stack. High-magnification cross-sectional bright-field micrographs from (c) ε-Ge/$In_{0.115}Ga_{0.885}As$ and (d) ε-Ge/$In_{0.173}Ga_{0.827}As$ heterostructures, respectively, showing the heterointerfaces. The insets show the corresponding FFT patterns from the entire visible area. Exclusive FFT patterns generated from each individual region in (c) and (d), are shown in (e-g) and (h-j), respectively. The diffractograms show no peak splitting, indicating contribution from a single lattice parameter across the heterointerfaces.

mode of decay, τ_0, which contains information about bulk recombination lifetime and surface recombination lifetime. Neglecting non-linear recombination processes, otherwise present under high injection conditions, τ_{eff} can be expressed as a summation of the non-radiative bulk lifetime (τ_{bulk}) and surface lifetime (τ_S) components as follows [44]:

$$\frac{1}{\tau_{eff}} = \frac{1}{\tau_{bulk}} + \frac{1}{\tau_S} \tag{2.2}$$

In the limits of effectively small epilayer thickness, d, and when the condition $S \ll \frac{2D}{d}$ is satisfied, $\tau_S \approx \frac{2S}{d}$, and Eqn 2.2 can be rewritten as [45, 46]:

$$\frac{1}{\tau_{eff}} = \frac{1}{\tau_{bulk}} + \frac{2S}{d} \tag{2.3}$$

where, D is the minority carrier diffusion coefficient under low injection and d is the length of the epilayer (*i.e.* thickness) along the growth direction. The factor of 2 in Eqn 2.3 stems from the symmetric treatment of the top and bottom interfaces in Ref. [44], in contrast to the asymmetric treatment in other noted works [47, 48]. From Eqn 2.3, it can be propounded that when $1/\tau_{eff}$ is plotted against $2/d$ recorded over samples of varied thicknesses, d, τ_{bulk} and S can be quantified from the y-intercept and slope, respectively, provided that the surface conditions remain unaltered. At the excitation wavelength ($\lambda = 1500\ nm$) of the laser source used in this work, the absorption coefficient (α) of Ge ($\approxeq 2.5 \times 10^4/cm$) ensures homogenous excitation of the Ge epilayers, while the underlying layers remain transparent to the source excitation, thus providing exclusive insight into the carrier dynamics of the Ge epilayers. It is assumed that one electron-hole

pair is generated for each photon impinging on the samples. Typical μ-PCD transients recorded from different thicknesses of the *unstrained* Ge/AlAs/GaAs heterostructure are shown in Figure 2.4(a) along with the corresponding exponential fits used to extract the effective lifetime, τ_{eff}, as explained shortly. The initial rapid roll-off in the transients is due to the quickly diminishing higher order terms in the lifetime expression, and the extension of this region is dependent upon the shape of the source [44]. The latter part of the traces, the principal mode of decay, can be fitted with an exponential regression to yield the effective lifetime, τ_{eff}. The parallel nature of the traces in Figure 2.4(a) indicates minimal effect of the chemical processing step on the surface conditions of the epilayers. Figure 2.4(b) shows $1/\tau_{eff}$ plotted against $2/d$, which yielded values of $\approx 114 \pm 2$ ns and $\approx 21.3 \pm 0.04$ cm/sec for τ_{bulk} and S, respectively. We recently reported effective lifetime of >100 ns on *unstrained* epitaxial Ge grown on a III-V buffer template in our previous work as well [49]. The condition of $S \ll \frac{2D}{d}$ is readily satisfied in this case, considering $D \approx$ 9 cm^2/sec, extracted from Hall measurements (*not shown here*), which enables the determination of τ_{bulk} from Eqn 2.3. Discussion regarding the accuracy of S following from Ref. [50] for the condition of $\frac{S \cdot d}{D} \leq 0.25$ (*satisfied in this case*) indicates that the extracted S value is accurate to within 4% over the entire range of S values.

It was previously shown by numerical modeling that achieving $\tau_{bulk} \geq 100$ ns in *strained* epitaxial Ge is critical to enable low-threshold Ge lasers, with threshold currents as low as 10×10^3 A/cm^2 being possible at 2% biaxial tensile strain and 1×10^{19} $/cm^3$ doping density [32]. To that end, typical μ-PCD transient curves were recorded from 270 nm *unstrained* Ge/AlAs/GaAs, 75 nm 0.61% ε-Ge/$In_{0.115}Ga_{0.885}As$, 75 nm 0.89% ε-Ge/$In_{0.173}Ga_{0.827}As$ and 30 nm 1.6% ε-Ge/$In_{0.24}Ga_{0.76}As$ heterostructures, shown along with their exponential

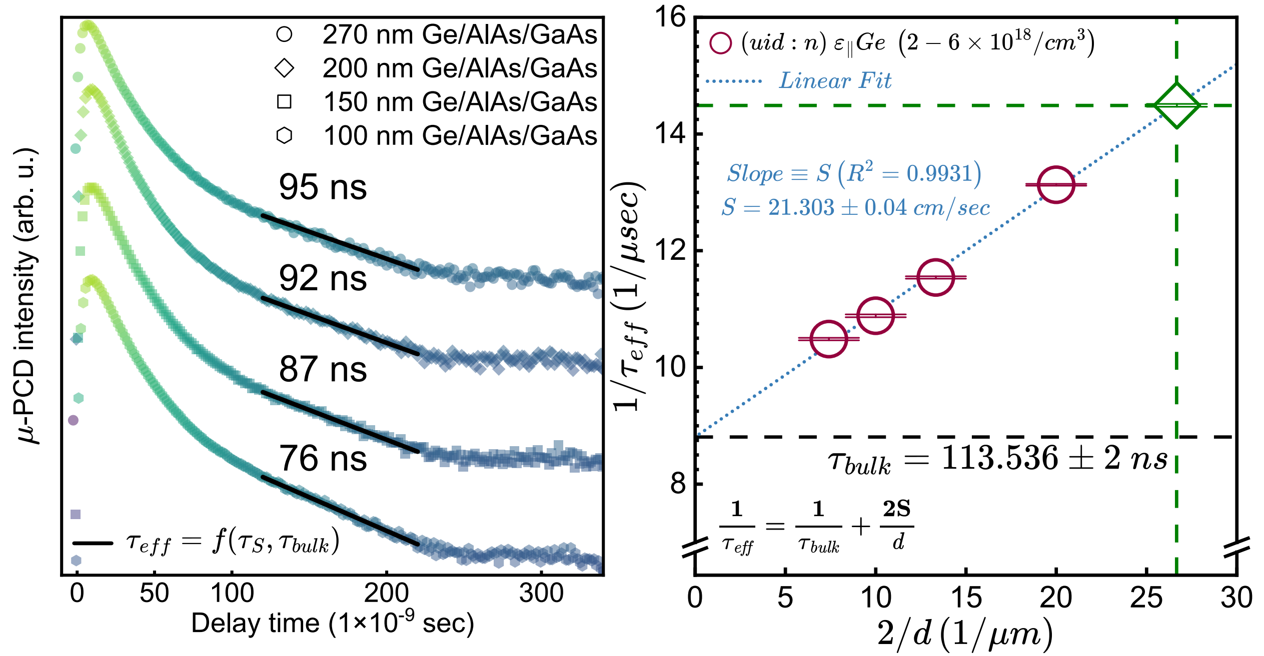

Figure 2.4: (a) Typical transient μ-PCD curves obtained from varying thicknesses of the *unstrained* Ge/AlAs/GaAs heterostructure. τ_{eff} values labeled alongside the curves are obtained by fitting the principal mode of decay with an exponential regression. (b) Extracted τ_{eff} (unfilled circles) are plotted against $2/d$, where d is the epilayer thickness, showing the linear fit according to $1/\tau_{eff} = 1/\tau_{bulk} + 2S/d$. Separation of the lifetime components yielded $\tau_{bulk} = 114 \pm 2\ ns$ and $S = 21.3 \pm 0.04\ cm/sec$. Given the good fitting ($R^2 = 0.9931$), a point on the linear fit corresponding to $d = 75\ nm$ (*green diamond*) yielding $\tau_{eff} \approx 69\ ns$ was extracted to eliminate thickness effect while comparing lifetime performance of ε-Ge epilayers. The traces shown in Figure 2.4 (a) are normalized and vertically shifted for viewing clarity.

fits in Figure 2.5(a). The extracted τ_{eff} values are plotted against the imparted in-plane biaxial strain (ε) in Figure 2.5(b), and the results are summarized in Table 2.2. The epilayer thickness effect on lifetime is readily observed (indicated by the *black* arrow in Figure 2.5(b), with the 270 nm Ge epilayer exhibiting higher τ_{eff} than the 100 nm Ge epilayer [51]. This observation can be attributed to the surface component of the principal mode of decay exhibiting longer lifetime in thicker samples, in line with the minority carriers decaying over a longer period of time [44]. It is well known that as increasing strain is engineered in an epilayer, a compromise in epilayer thickness (d) has to be made to maintain the thickness under the critical layer thickness, h_c, to avoid introducing energetically favorable misfit dislocations. Figure 2.5(b) includes the theoretically calculated h_c values on the alternate coordinate axis, based on the strain energy-balance model developed by People and Bean [52], validating that the thicknesses of the Ge epilayers studied in this work are kept within the theoretical h_c limit to ensure minimal defect formation due to epilayer relaxation. From Figure 2.5(b), one can also observe an increase in τ_{eff} obtained from heterostructures with increased imparted strain, with the only apparent anomaly of slightly lower τ_{eff} exhibited by 75 nm 0.61% ε-Ge than the 100 nm *unstrained* Ge epilayer. This observation could be explained as follows: from Figure 2.5(b), a data point taken on the linear fit corresponding to $d = 75\ nm$ for the *unstrained* Ge epilayer yields $\tau_{eff} \approx 69\ ns$ (*see green diamond in* Figure 2.4(b) *and* Figure 2.5(b)), which is close to $\tau_{eff} \approx 70\ ns$ exhibited by the 0.61% ε-Ge sample, thus alluding to epilayer thickness effect on lifetime [51]. This observation coincides with 270 nm *unstrained* Ge/AlAs/GaAs exhibiting higher τ_{eff} than the etched 100 nm counterpart from the same sample.

The effect of tensile strain on the band structure and carrier dynamics of epitaxial Ge

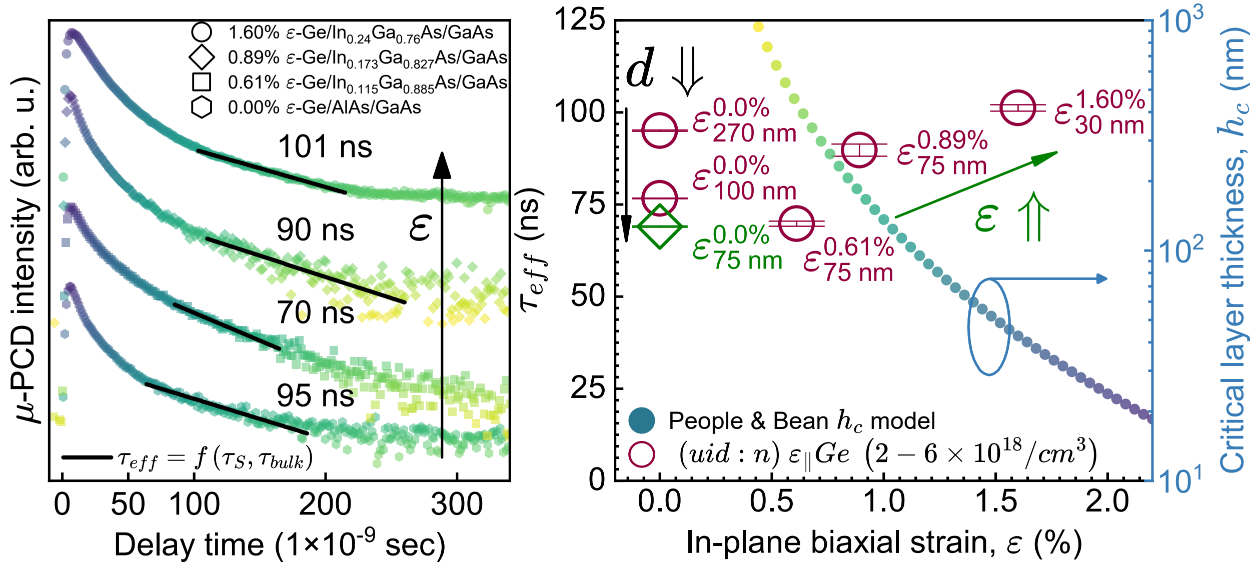

Figure 2.5: (a) Typical transient μ-PCD curves obtained from 270 nm *unstrained* Ge/AlAs/GaAs, 75 nm 0.61% ε-Ge/$In_{0.115}Ga_{0.885}As$, 75 nm 0.89% ε-Ge/$In_{0.173}Ga_{0.827}As$ and 30 nm 1.6% ε-Ge/In0.24Ga0.76As heterostructures. The traces have been normalized and vertically shifted for clarity. (b) Extracted τ_{eff} shown in (a) and extracted from etched 100 nm *unstrained* Ge/AlAs/GaAs (*see Figure 2.4(b)*) plotted against the imparted in-plane tensile strain (ε) to Ge epilayers, 0% indicating *unstrained* epilayers. The alternate y-axis shows the critical layer thickness, h_c, calculated based on the People and Bean strain energy-balance model [52]. The thickness effect on τ_{eff} is also shown (black arrow, pointing downward) indicating the reduction in τ_{eff} with decreasing thickness. A point taken on the fit of Figure 2.4(b) corresponding to $d = 75\ nm$ yielding $\tau_{eff} \approx 69\ ns$ (*green diamond*) is also indicated, which was used to eliminate thickness effect when comparing τ_{eff} between *strained* and *unstrained* Ge epilayers. The observed increase in τ_{eff} as strain is increased is indicated using the green arrow pointing upward at an angle.

has been elucidated in notable theoretical works, showing improved mobility as a combined consequence of reduced photon scattering and reduction in conductivity mass [53, 54]. Recently, we reported numerical and experimental 2× mobility enhancement in 1.6% ε-Ge/$In_{0.24}Ga_{0.76}As$ heterostructures compared to the *unstrained* counterpart [55]. We emphasize here that while the spatial resolution of μ-PCD measurements is **insufficient** to resolve local changes in doping and strain, μ-PCD is sensitive to changes in local conductance induced by the generation of excess photocarriers [56]. As such, with enhancement in mobility induced by tensile strain, the exhibited τ_{eff} could potentially see an improvement in the absence of severe defects originating during heteroepitaxy, consistent with the results shown in this work. Additionally, from the increasing τ_{eff}, it can be posited that the strained heterostructures possibly have similar τ_{bulk}, as their *unstrained* counterpart, corroborating the prime material quality shown in this work. This is an important result in terms of material quality benchmarking, and can propel further research into device quality epitaxial Ge to fully harness the benefits of methods, mentioned previously, to enhance the emission performance of Ge-based photonic devices. These results corroborate our findings about the pseudomorphic nature of the epitaxial Ge growth from the XTEM and HR-XRD analyses, thus providing a pathway for integration of (001) biaxially tensile strained Ge on Si *via* III-V buffer technology.

Table 2.2: Summary of extracted parameters from HR-XRD, XTEM and μ-PCD measurements, including τ_{eff} and goodness of fit (R^2) achieved from *unstrained* Ge and ε-Ge. The microwave pump source wavelength for μ-PCD measurements, carried out at 300 K, was kept constant at $\lambda = 1500$ nm for all samples.

sample information			lifetime parameters		
heterostructure	Ge epilayer thickness (nm)	ε from XRD (%)	extracted lifetime, τ_{eff} (ns)	error ($\pm$ ns)	coefficient of determination (R^2)
Ge/AlAs/GaAs	270	0.00	95.37	0.1894	0.9794
	200		91.87	0.0343	0.9821
	150		86.84	0.1546	0.9887
	100		76.64	0.1116	0.9926
ε-Ge/$In_{0.145}Ga_{0.855}As$	75	0.61	68.46	1.1633	0.9509
ε-Ge/$In_{0.173}Ga_{0.827}As$	75	0.89	89.75	1.6840	0.9031
ε-Ge/$In_{0.24}Ga_{0.76}As$	~30	1.60	101.20	0.8667	0.9817

2.4 Conclusion

To summarize, we have performed extensive structural investigation of ε-Ge grown *via* $In_xGa_{1-x}As$ metamorphic buffer technology on GaAs substrate. HR-XRD analyses showed excellent crystalline quality and pseudomorphic nature of the Ge epilayers. Quantification of the strain state of the Ge epilayers showed successful strain transfer of 0.61% and 0.89%, respectively, to ε-Ge grown on $In_{0.115}Ga_{0.885}As$ and $In_{0.173}Ga_{0.827}As$ virtual substrates. High-resolution and high-magnification XTEM micrographs further corroborated the XRD analyses and showed abrupt ε-Ge/$In_xGa_{1-x}As$ heterointerfaces, devoid of short- and long-range lattice disorder. Contactless μ-PCD measurements recorded from *unstrained* Ge/AlAs/GaAs heterostructures exhibited $\tau_{bulk} \approx 114 \pm 2$ ns and $S \approx 21.3 \pm 0.04$ cm/sec. Furthermore, μ-PCD measurements from ε-Ge epilayers showed no degradation in τ_{eff}, despite thickness reduction necessitated by the application of in-plane biaxial tensile strain, providing support to the excellent material quality of the Ge epilayers. We attribute the increased τ_{eff} in ε-Ge epilayers to the enhancement of epilayer carrier mobility induced by the in-plane $\langle 110 \rangle$ biaxial tensile strain. The excellent material quality, coupled with the freedom to tailor strain state of the active Ge epilayer *via* III-V strain template, can propel extensive advancement in the emission efficiency of Ge optical sources. Ultimately, combining the excellent compatibility of Ge with the existing Si CMOS technology coupled with the lifetime improvements shown in this work can augment the benefits of other methods, mentioned previously, to realize low-threshold Ge lasers for photonic applications heterogeneously integrated on Si.

Bibliography

[1] S. Bhattacharya, S. W. Johnston, S. Datta, and M. K. Hudait, "Interplay Between Strain and Thickness on the Effective Carrier Lifetime of Buffer-Mediated Epitaxial Germanium Probed by the Photoconductance Decay Technique," *ACS Applied Electronic Materials*, vol. 5, no. 6, pp. 3190–3197, May 2023, ISSN: 2637-6113. DOI: 10.1021/acsaelm.3c00256.

[2] B. Jalali, S. Yegnanarayanan, T. Yoon, T. Yoshimoto, I. Rendina, and F. Coppinger, "Advances in Silicon-on-Insulator Optoelectronics," *IEEE Journal of Selected Topics in Quantum Electronics*, vol. 4, no. 6, pp. 938–947, 1998, ISSN: 1558-4542. DOI: 10.1109/2944.736081.

[3] P. Herve and S. Ovadia, "Optical Technologies for Enterprise Networks," *Intel Technology Journal*, vol. 8, no. 2, pp. 73–82, 2004, ISSN: 1535-864X.

[4] K. H. Koo, H. Cho, P. Kapur, and K. C. Saraswat, "Performance Comparisons Between Carbon Nanotubes, Optical, and Cu for Future High-Performance On-Chip Interconnect Applications," *IEEE Transactions on Electron Devices*, vol. 54, no. 12, pp. 3206–3215, 2007, ISSN: 1557-9646. DOI: 10.1109/TED.2007.909045.

[5] G. T. Reed, G. Z. Mashanovich, F. Y. Gardes, D. J. Thomson, Y. Hu, J. Soler-Penades, M. Nedeljkovic, A. Khokar, P. Thomas, C. Littlejohns, A. Ahmad, S. Reynolds, R. Topley, C. Mitchell, S. Stankovic, P. R. Wilson, L. Ke, T. M. B. Masaud, A. Tarazona, and H. Chong, "Silicon Photonics," in *2014 7th International Silicon-Germanium Technology and Device Meeting (ISTDM)*, pp. 5–6. DOI: 10.1109/ISTDM.2014.6874661.

[6] R. Soref and J. Larenzo, “All-silicon active and passive guided-wave components for $\lambda = 1.3$ and 1.6 μm,” *IEEE Journal of Quantum Electronics*, vol. 22, no. 6, pp. 873–879, 1986, ISSN: 1558-1713. DOI: 10.1109/JQE.1986.1073057.

[7] R. Soref, “The Past, Present, and Future of Silicon Photonics,” *IEEE Journal of Selected Topics in Quantum Electronics*, vol. 12, no. 6, pp. 1678–1687, 2006, ISSN: 1558-4542. DOI: 10.1109/JSTQE.2006.883151.

[8] R. Chau, B. Doyle, S. Datta, J. Kavalieros, and K. Zhang, “Integrated Nanoelectronics for the Future,” *Nature Materials*, vol. 6, no. 11, pp. 810–812, Nov. 2007, ISSN: 1476-4660. DOI: 10.1038/nmat2014.

[9] J. A. del Alamo, “Nanometre-Scale Electronics with III–V Compound Semiconductors,” *Nature*, vol. 479, no. 7373, pp. 317–323, 2011, ISSN: 1476-4687. DOI: 10.1038/nature10677.

[10] R. Pillarisetty, “Academic and Industry Research Progress in Germanium Nanodevices,” *Nature*, vol. 479, no. 7373, pp. 324–328, Nov. 2011, ISSN: 1476-4687. DOI: 10.1038/nature10678.

[11] K. J. Kuhn, “Considerations for Ultimate CMOS Scaling,” *IEEE Transactions on Electron Devices*, vol. 59, no. 7, pp. 1813–1828, 2012, ISSN: 1557-9646. DOI: 10.1109/TED.2012.2193129.

[12] K. Saraswat, D. Kim, T. Krishnamohan, D. Kuzum, A. K. Okyay, A. Pethe, and H.-Y. Yu, “Germanium for High Performance MOSFETs and Optical Interconnects,” *ECS Transactions*, vol. 16, no. 10, pp. 3–12, 2008, ISSN: 1938-5862 1938-6737. DOI: 10.1149/1.2986748.

[13] P. Chaisakul, D. Marris-Morini, J. Frigerio, D. Chrastina, M.-S. Rouifed, S. Cecchi, P. Crozat, G. Isella, and L. Vivien, "Integrated Germanium Optical Interconnects on Silicon Substrates," *Nature Photonics*, vol. 8, no. 6, pp. 482–488, 2014, ISSN: 1749-4893. DOI: 10.1038/nphoton.2014.73.

[14] J. Liu, "Monolithically Integrated Ge-on-Si Active Photonics," *Photonics*, vol. 1, no. 3, pp. 162–197, 2014, ISSN: 2304-6732. DOI: 10.3390/photonics1030162.

[15] M. Clavel, D. Saladukha, P. S. Goley, T. J. Ochalski, F. Murphy-Armando, R. J. Bodnar, and M. K. Hudait, "Heterogeneously-Grown Tunable Tensile Strained Germanium on Silicon for Photonic Devices," *ACS Applied Materials & Interfaces*, vol. 7, no. 48, pp. 26 470–26 481, 2015, ISSN: 1944-8244. DOI: 10.1021/acsami.5b07385.

[16] V. Reboud, A. Gassenq, J. M. Hartmann, J. Widiez, L. Virot, J. Aubin, K. Guilloy, S. Tardif, J. M. Fédéli, N. Pauc, A. Chelnokov, and V. Calvo, "Germanium Based Photonic Components toward a Full Silicon/Germanium Photonic Platform," *Progress in Crystal Growth and Characterization of Materials*, vol. 63, no. 2, pp. 1–24, 2017, ISSN: 0960-8974. DOI: 10.1016/j.pcrysgrow.2017.04.004.

[17] B. Dutt, D. S. Sukhdeo, D. Nam, B. M. Vulovic, Z. Yuan, and K. C. Saraswat, "Roadmap to an Efficient Germanium-on-Silicon Laser: Strain vs. *n*-Type Doping," *IEEE Photonics Journal*, vol. 4, no. 5, pp. 2002–2009, 2012, ISSN: 1943-0655. DOI: 10.1109/jphot.2012.2221692.

[18] D. Nam, J.-H. Kang, M. L. Brongersma, and K. C. Saraswat, "Observation of Improved Minority Carrier Lifetimes in High-Quality Ge-On-Insulator Using Time-

Resolved Photoluminescence," *Optics Letters*, vol. 39, no. 21, pp. 6205–6208, 2014. DOI: 10.1364/ol.39.006205.

[19] D. S. Sukhdeo, D. Nam, J.-H. Kang, M. L. Brongersma, and K. C. Saraswat, "Direct bandgap germanium-on-silicon inferred from 5.7% ⟨100⟩ uniaxial tensile strain [Invited]," *Photonics Research*, vol. 2, no. 3, A8–A13, 2014. DOI: 10.1364/PRJ.2.0000A8.

[20] M. K. Hudait, F. Murphy-Armando, D. Saladukha, M. B. Clavel, P. S. Goley, D. Maurya, S. Bhattacharya, and T. J. Ochalski, "Design, Theoretical, and Experimental Investigation of Tensile-Strained Germanium Quantum-Well Laser Structure," *ACS Applied Electronic Materials*, vol. 3, no. 10, pp. 4535–4547, 2021. DOI: 10.1021/acsaelm.1c00660.

[21] R. Geiger, T. Zabel, and H. Sigg, "Group IV Direct Band Gap Photonics: Methods, Challenges, and Opportunities," *Frontiers in Materials*, vol. 2, 2015, ISSN: 2296-8016. DOI: 10.3389/fmats.2015.00052.

[22] R. A. Soref and C. H. Perry, "Predicted band gap of the new semiconductor SiGeSn," *Journal of Applied Physics*, vol. 69, no. 1, pp. 539–541, 1991. DOI: 10.1063/1.347704.

[23] S. Wirths, R. Geiger, N. von den Driesch, G. Mussler, T. Stoica, S. Mantl, Z. Ikonic, M. Luysberg, S. Chiussi, J. M. Hartmann, H. Sigg, J. Faist, D. Buca, and D. Grützmacher, "Lasing in direct-bandgap GeSn alloy grown on Si," *Nature Photonics*, vol. 9, no. 2, pp. 88–92, 2015, ISSN: 1749-4893. DOI: 10.1038/nphoton.2014.321.

[24] V. Reboud, A. Gassenq, N. Pauc, J. Aubin, L. Milord, Q. M. Thai, M. Bertrand, K. Guilloy, D. Rouchon, J. Rothman, T. Zabel, F. A. Pilon, H. Sigg, A. Chelnokov, J. M. Hartmann, and V. Calvo, "Optically pumped GeSn micro-disks with 16% Sn lasing at 3.1 μm up to 180K," *Applied Physics Letters*, vol. 111, no. 9, p. 092 101, 2017. DOI: 10.1063/1.5000353.

[25] J. Margetis, S. Al-Kabi, W. Du, W. Dou, Y. Zhou, T. Pham, P. Grant, S. Ghetmiri, A. Mosleh, B. Li, J. Liu, G. Sun, R. Soref, J. Tolle, M. Mortazavi, and S.-Q. Yu, "Si-Based GeSn Lasers with Wavelength Coverage of 2–3 μm and Operating Temperatures up to 180 K," *ACS Photonics*, vol. 5, no. 3, pp. 827–833, 2018. DOI: 10.1021/acsphotonics.7b00938.

[26] A. Gassenq, K. Guilloy, G. O. Dias, N. Pauc, D. Rouchon, J.-M. Hartmann, J. Widiez, S. Tardif, F. Rieutord, J. Escalante, I. Duchemin, Y.-M. Niquet, R. Geiger, T. Zabel, H. Sigg, J. Faist, A. Chelnokov, V. Reboud, and V. Calvo, "1.9% bi-axial Tensile Strain in Thick Germanium Suspended Membranes Fabricated in Optical Germanium-On-Insulator Substrates for Laser Applications," *Applied Physics Letters*, vol. 107, no. 19, p. 191 904, 2015. DOI: 10.1063/1.4935590.

[27] A. Gassenq, S. Tardif, K. Guilloy, G. O. Dias, N. Pauc, I. Duchemin, D. Rouchon, J.-M. Hartmann, J. Widiez, J. Escalante, Y.-M. Niquet, R. Geiger, T. Zabel, H. Sigg, J. Faist, A. Chelnokov, F. Rieutord, V. Reboud, and V. Calvo, "Accurate strain measurements in highly strained Ge microbridges," *Applied Physics Letters*, vol. 108, no. 24, p. 241 902, 2016. DOI: 10.1063/1.4953788.

[28] R. W. Millar, K. Gallacher, J. Frigerio, A. Ballabio, A. Bashir, I. MacLaren, G. Isella, and D. J. Paul, "Analysis of Ge micro-cavities with in-plane tensile strains above 2%," *Optics Express*, vol. 24, no. 5, pp. 4365–4374, 2016. DOI: 10.1364/OE.24.004365.

[29] F. T. Armand Pilon, A. Lyasota, Y. M. Niquet, V. Reboud, V. Calvo, N. Pauc, J. Widiez, C. Bonzon, J. M. Hartmann, A. Chelnokov, J. Faist, and H. Sigg, "Lasing in strained Germanium Microbridges," *Nature Communications*, vol. 10, no. 1, p. 2724, 2019, Armand Pilon, F T Lyasota, A Niquet, Y-M Reboud, V Calvo, V Pauc, N Widiez, J Bonzon, C Hartmann, J M Chelnokov, A Faist, J Sigg, H eng Research Support, Non-U.S. Gov't England 2019/06/22 Nat Commun. 2019 Jun 20;10(1):2724. doi: 10.1038/s41467-019-10655-6., ISSN: 2041-1723 (Electronic) 2041-1723 (Linking). DOI: 10.1038/s41467-019-10655-6.

[30] J. J. Sheng, D. Leonhardt, S. M. Han, S. W. Johnston, J. G. Cederberg, and M. S. Carroll, "Empirical correlation for minority carrier lifetime to defect density profile in germanium on silicon grown by nanoscale interfacial engineering," *Journal of Vacuum Science & Technology B*, vol. 31, no. 5, p. 051 201, 2013. DOI: 10.1116/1.4816488.

[31] R. Geiger, J. Frigerio, M. J. Süess, D. Chrastina, G. Isella, R. Spolenak, J. Faist, and H. Sigg, "Excess Carrier Lifetimes in Ge Layers on Si," *Applied Physics Letters*, vol. 104, no. 6, p. 062 106, 2014. DOI: 10.1063/1.4865237.

[32] D. S. Sukhdeo, S. Gupta, K. C. Saraswat, B. Dutt, and D. Nam, "Impact of minority carrier lifetime on the performance of strained Germanium light sources," *Optics*

Communications, vol. 364, pp. 233–237, 2016, (Raj), ISSN: 0030-4018. DOI: 10.1016/j.optcom.2015.11.060.

[33] Y. Bai, K. E. Lee, C. Cheng, M. L. Lee, and E. A. Fitzgerald, "Growth of highly tensile-strained Ge on relaxed $In_xGa_{1-x}As$ by metal-organic chemical vapor deposition," *Journal of Applied Physics*, vol. 104, no. 8, 2008, ISSN: 0021-8979. DOI: 10.1063/1.3005886.

[34] R. Jakomin, M. d. Kersauson, M. E. Kurdi, L. Largeau, O. Mauguin, G. Beaudoin, S. Sauvage, R. Ossikovski, G. Ndong, M. Chaigneau, I. Sagnes, and P. Boucaud, "High quality tensile-strained n-doped germanium thin films grown on InGaAs buffer layers by metal-organic chemical vapor deposition," *Applied Physics Letters*, vol. 98, no. 9, p. 091 901, 2011. DOI: 10.1063/1.3559231.

[35] M. Hudait, M. Clavel, L. Lester, D. Saladukha, T. Ochalski, and F. Murphy-Armando, "Heterogeneously grown tunable group-IV laser on silicon," in *SPIE OPTO*, vol. 9755, SPIE, 2016, 97550Y. DOI: 10.1117/12.2218364.

[36] M. Clavel, P. Goley, N. Jain, Y. Zhu, and M. K. Hudait, "Strain-Engineered Biaxial Tensile Epitaxial Germanium for High-Performance Ge/InGaAs Tunnel Field-Effect Transistors," *IEEE Journal of the Electron Devices Society*, vol. 3, no. 3, pp. 184–193, 2015, ISSN: 2168-6734. DOI: 10.1109/JEDS.2015.2394743.

[37] J.-M. Chauveau, Y. Androussi, A. Lefebvre, J. D. Persio, and Y. Cordier, "Indium Content Measurements in Metamorphic High Electron Mobility Transistor Structures by Combination of X-Ray Reciprocal Space Mapping and Transmission Electron Microscopy," *Journal of Applied Physics*, vol. 93, no. 7, pp. 4219–4225, 2003. DOI: 10.1063/1.1544074.

[38] E. Gaubas, J. Vanhellemont, E. Simoen, I. Romandic, W. Geens, and P. Clauws, "Carrier lifetime dependence on doping, metal implants and excitation density in Ge and Si," *Physica B: Condensed Matter*, vol. 401-402, pp. 222–225, 2007, ISSN: 0921-4526. DOI: 10.1016/j.physb.2007.08.151.

[39] S. Deb and B. R. Nag, "Measurement of lifetime of carriers in semiconductors through microwave reflection," *Journal of Applied Physics*, vol. 33, no. 4, pp. 1604–1604, 1962, ISSN: 0021-8979 1089-7550. DOI: 10.1063/1.1728779.

[40] Y. Mada, "A Nondestructive Method for Measuring the Spatial Distribution of Minority Carrier Lifetime in Silicon Wafer," *Japanese Journal of Applied Physics*, vol. 18, no. 11, pp. 2171–2172, 1979, ISSN: 0021-4922. DOI: 10.1143/jjap.18.2171.

[41] M. Kunst and G. Beck, "The study of charge carrier kinetics in semiconductors by microwave conductivity measurements," *Journal of Applied Physics*, vol. 60, no. 10, pp. 3558–3566, 1986. DOI: 10.1063/1.337612.

[42] S. Johnston, K. Zaunbrecher, R. Ahrenkiel, D. Kuciauskas, D. Albin, and W. Metzger, "Simultaneous Measurement of Minority-Carrier Lifetime in Single-Crystal CdTe Using Three Transient Decay Techniques," *IEEE Journal of Photovoltaics*, vol. 4, no. 5, pp. 1295–1300, 2014, ISSN: 2156-3403. DOI: 10.1109/JPHOTOV.2014.2339491.

[43] K. Lauer, A. Laades, H. Übensee, H. Metzner, and A. Lawerenz, "Detailed analysis of the microwave-detected photoconductance decay in crystalline silicon," *Journal of Applied Physics*, vol. 104, no. 10, p. 104 503, 2008, ISSN: 0021-8979. DOI: 10.1063/1.3021459.

[44] K. L. Luke and L.-J. Cheng, “Analysis of the interaction of a laser pulse with a silicon wafer: Determination of bulk lifetime and surface recombination velocity,” *Journal of Applied Physics*, vol. 61, no. 6, pp. 2282–2293, 1987, ISSN: 0021-8979. DOI: 10.1063/1.337938.

[45] E. Yablonovitch and T. J. Gmitter, “A contactless minority lifetime probe of heterostructures, surfaces, interfaces and bulk wafers,” *Solid-State Electronics*, vol. 35, no. 3, pp. 261–267, 1992, ISSN: 0038-1101. DOI: 10.1016/0038-1101(92)90230-A.

[46] N. Derhacobian, J. T. Walton, P. N. Luke, Y. K. Wong, and C. S. Rossington, “Proper interpretation of photoconductive decay transients in semiconductors having finite surface recombination velocity,” *Journal of Applied Physics*, vol. 76, no. 8, pp. 4663–4669, 1994, ISSN: 0021-8979. DOI: 10.1063/1.357304.

[47] G. S. Kousik, Z. G. Ling, and P. K. Ajmera, “Nondestructive technique to measure bulk lifetime and surface recombination velocities at the two surfaces by infrared absorption due to pulsed optical excitation,” *Journal of Applied Physics*, vol. 72, no. 1, pp. 141–146, 1992, ISSN: 0021-8979. DOI: 10.1063/1.352174.

[48] Z. G. Ling, P. K. Ajmera, and G. S. Kousik, “Nondestructive measurement of bulk lifetime and surface recombination velocities,” in *Conference Record of the Twenty Third IEEE Photovoltaic Specialists Conference - 1993 (Cat. No.93CH3283-9)*, IEEE, pp. 360–363. DOI: 10.1109/PVSC.1993.347155.

[49] M. K. Hudait and S. W. Johnston, “Probing crystallographic orientation-specific carrier lifetimes in epitaxial Ge/AlAs and InGaAs/InP heterostructures,” *Materials*

Advances, vol. 3, no. 12, pp. 5034–5042, 2022, ISSN: 2633-5409. DOI: 10.1039/D2MA00260D.

[50] A. B. Sproul, "Dimensionless solution of the equation describing the effect of surface recombination on carrier decay in semiconductors," *Journal of Applied Physics*, vol. 76, no. 5, pp. 2851–2854, 1994, ISSN: 0021-8979. DOI: 10.1063/1.357521.

[51] E. Gaubas, M. Bauža, A. Uleckas, and J. Vanhellemont, "Carrier lifetime studies in Ge using microwave and infrared light techniques," *Materials Science in Semiconductor Processing*, vol. 9, no. 4, pp. 781–787, 2006, ISSN: 1369-8001. DOI: 10.1016/j.mssp.2006.08.023.

[52] R. People and J. C. Bean, "Calculation of critical layer thickness versus lattice mismatch for Ge_xSi_{1-x}/Si strained-layer heterostructures," *Applied Physics Letters*, vol. 47, no. 3, pp. 322–324, 1985, ISSN: 0003-6951. DOI: 10.1063/1.96206.

[53] M. E. Kurdi, G. Fishman, S. Sauvage, and P. Boucaud, "Band structure and optical gain of tensile-strained germanium based on a 30 band $\vec{k} \cdot \vec{p}$ formalism," *Journal of Applied Physics*, vol. 107, no. 1, p. 013 710, 2010. DOI: 10.1063/1.3279307.

[54] F. Murphy-Armando and S. Fahy, "Giant enhancement of n-type carrier mobility in highly strained germanium nanostructures," *Journal of Applied Physics*, vol. 109, no. 11, p. 113 703, 2011. DOI: 10.1063/1.3590334.

[55] M. B. Clavel, F. Murphy-Armando, Y. Xie, K. T. Henry, M. Kuhn, R. J. Bodnar, G. A. Khodaparast, D. Smirnov, J. J. Heremans, and M. K. Hudait, "Multivalley Electron Conduction at the Indirect-Direct Crossover Point in Highly Tensile-Strained Germanium," *Physical Review Applied*, vol. 18, no. 6, p. 064 083, 2022, PRAPPLIED. DOI: 10.1103/PhysRevApplied.18.064083.

[56] D. Klein, F. Wuensch, and M. Kunst, "The determination of charge-carrier lifetime in silicon," *physica status solidi (b)*, vol. 245, no. 9, pp. 1865–1876, 2008, ISSN: 0370-1972. DOI: 10.1002/pssb.200879544.

This page left intentionally blank

Chapter 3:

Elucidating the Role of InGaAs and InAlAs Buffers on Carrier Dynamics of Tensile Strained Germanium Double Heterostructures

The following chapter has been reproduced from Ref. **S. Bhattacharya, S. W. Johnston, R. J. Bodnar, and M. K. Hudait, "Elucidating the Role of InGaAs and InAlAs Buffers on Carrier Dynamics of Tensile-Strained Ge Double Heterostructures,"** ***ACS Applied Electronic Materials*****, vol. 6, no. 6, pp. 4247–4256, Jun. 2024, ISSN: 2637-6113. DOI:** 10.1021/acsaelm.4c00347 *with minor changes* [1]. The author acknowledges epitaxial growth facilitation by M. Clavel, and S. W. Johnston for photoconductance decay measurements.

Extensive research efforts of strained germanium (Ge) are currently underway due to its unique properties, namely (i) possibility of band gap and strain engineering to achieve direct band gap, thus exhibiting superior radiative properties and (ii) higher electron and hole mobilities than Si for

upcoming technology nodes. Realizing lasing structures is vital to leverage the benefits of tensile-strained Ge (ε-Ge). Here, we use a combination of different analytical tools to elucidate the effect of the InGaAs/InAlAs underlying and InGaAs overlaying heterostructures on the material quality and strain state of ε-Ge grown by molecular beam epitaxy. Using x-ray analysis, we show the constancy of tensile strain in sub-50 nm ε-Ge in a quantum-well (QW) heterostructure. Further, effective carrier lifetime using photoconductive decay as a function of buffer type exhibited high (low) defect-limited carrier lifetime of $\simeq$68 ns ($\simeq$13 ns) in 0.61% (0.66%) ε-Ge grown on InGaAs (InAlAs) buffer. These results correspond well with measured surface roughness of 1.289 nm (6.303 nm), consistent with surface effect of the ε-Ge/III-V heterointerface. Furthermore, reasonably high effective lifetime of $\simeq$78 ns is demonstrated in QW of $\simeq$30 nm 1.6% ε-Ge, a moderate reduction from $\simeq$99 ns in uncapped ε-Ge, alluding to surface effect of the overlying heterointerface. Thus, the above results highlight the prime quality of ε-Ge that can be achieved *via* III-V heteroepitaxy and paves a path for integrated Ge photonics.

3.1 Introduction

The recent resurgence of interest in germanium (Ge) in the academic, technological, and commercial communities can be attributed to its unique properties that can be applied to electronic and photonic applications [2, 3]. One such attractive property is the potential to use band gap engineering to achieve direct band gap photoluminescence in Ge [4–6]. In addition, Ge is compatible with the existing manufacturing infrastructure for silicon (Si), making it a popular alternative material for Si-compatible photonic applications [7]. In fact, introduced at the 90 nm node, Ge has since been alloyed with Si in the drain/source well regions to impart uniaxial strain to the Si channel region to improve channel mobility [8, 9]. In a significant development, Liu et al. reported optical gain at room temperature in Ge directly grown on Si [10]. This was made possible by leveraging the nominal $\simeq$ 0.2% tensile strain due to the difference in thermal expansion coefficients and heavy *n*-type doping. With the increasing need for optical alternatives for intra- and inter-chip communication following the saturation of performance increases in traditional copper interconnects [11–13], Ge offers to bridge the gap with its improved radiative recombination efficiency [14, 15]. On the other hand, the concurrent rise in demand for high-mobility channel materials to enhance logic performance in the approaching sub-3 nm technology nodes, which exceeds the capabilities of Si, is encouraging increased interest in Ge due to its intrinsically higher electron and hole mobilities than Si [2, 7].

Due to the pseudo-direct bandgap of Ge, researchers have employed several different methodologies to enhance the radiative efficiency *via* strain engineering [16–18], band-structure modification [19, 20], Sn-alloying [21], innovative structures for lasing in the

form of nanomembranes [22, 23], micro-cavities [24] and micro-disks [25–27], and more recently, direct epitaxial Ge growth on $In_{0.52}Al_{0.48}As$ lattice-matched to InP [28], resulting in the formation of self-assembled Ge quantum dots (QDs). However, despite the reported success of some of these techniques to enhance radiative emission in Ge and Ge-based materials, most of these techniques suffer from incompatibility with the development of group-IV based lasing structures due to the lack of tunability of the electronic and optical confinement, and/or due to complex microfabrication or growth processes, hindering large-scale integrability. On the other hand, one widely researched strategy for integration of Ge on Si has been using III-V metamorphic buffers, which can yield lower dislocation densities and improved crystalline quality [29, 30]. The concomitant benefit of utilizing III-V metamorphic buffers is the flexibility of tuning the underlying lattice parameters to impart strain, tensile and compressive, to the active Ge epilayer to achieve strain and bandgap engineering, as well as providing tunability of optical confinement [29, 31, 32]. Ternary (Ga, Al)-InAs-based buffers have been effectively utilized in the epitaxial growth of Ge for this purpose on on-axis and vicinal Si and III-V substrates. It has been shown previously that thick GaAs grown directly on Si can be used to block propagating threading dislocations from reaching the surface [33, 34], which can then act as the starting surface for growing epitaxial films with high crystalline quality. Maximizing the potential of strain and band gap engineering of Ge for photonic applications requires the material system to be compatible with the development of quantum well (QW) heterostructures [35]. Ideally, this entails including a cladding layer on either side with a large bandgap and optical refractive indices distinct from the active layer, for appropriate optical gain and optical confinement, respectively. That said, the present literature lacks the effect of the dual heterointerfaces in such QW heterostructures on the material properties and carrier recombination dynamics

of strain-engineered Ge.

In this work, we have undertaken a comparative analysis of the structural properties and carrier dynamics of pseudomorphic tensile strained Ge (ε-Ge) integrated on vicinal (001)GaAs substrates *via* III-V buffers. Metamorphic InGaAs and InAlAs buffers grown using solid source molecular beam epitaxy (MBE) were used to impart strain to the overlying epitaxial Ge, and our results demonstrate pseudomorphic tensile strained Ge epitaxy, verified by high-resolution x-ray diffraction analyses. We present a detailed characterization of the relaxation dynamics in the buffers and its effect on the surface morphology of the ε-Ge using atomic force microscopy and x-ray analyses. Furthermore, we demonstrate the constancy of Ge strain state post overlayer growth on the top, a structure which emulates a practical QW lasing heterostructure. Finally, we demonstrate the reasonably high defect-limited effective carrier lifetimes achieved in InGaAs/ε-Ge/InGaAs and ε-Ge/InGaAs heterostructures compared to ε-Ge/InAlAs, simultaneously providing substantial evidence for the viability of strain engineered Ge based optical sources and photonic devices.

3.2 Experimental Section

3.2.1 Materials Synthesis

The heterostructures studied in this work, shown in Figure 3.1, were grown using solid source MBE using isolated group III-V and group-IV chambers, connected *via* ultra-high vacuum chamber. Linearly graded metamorphic $In_xGa_{1-x}As$ and $In_xAl_{1-x}As$ buffers were grown on epi-ready semi-insulating vicinal (001)GaAs/2°[011] substrates due to their ability to promote enhanced relaxation as compared to step-graded and non-linear buffers [36]. The isolation of the growth chambers minimizes the possibility of atomic interdiffusion at the group-IV/group-III-V heterointerfaces during epitaxial growth. Each growth run was monitored using an in-situ reflection high-energy electron diffraction (RHEED) module inside the III-V growth chamber. Oxide desorption of each substrate was performed at (thermocouple temperature) ≃750°C maintaining a high arsenic (As_2) overpressure of $\sim$ 10^{-5} Torr to prevent degradation of III-V surface morphology. As such, subsequent growth was performed only after observation of long and clear (2×4) patterns on the RHEED screen, suggesting good oxide desorption. Linearly graded metamorphic $In_xGa_{1-x}As$ and $In_xAl_{1-x}As$ buffers in heterostructures A and B were grown at 525°C and 420°C, respectively, with the lower temperature used for the latter to balance the disparate adatom surface mobilities of indium (In) and aluminum (Al) as well as a lower growth rate, with an additional overshoot and inverse step to promote enhanced relaxation of the buffers. Linearly graded $In_xGa_{1-x}As$ buffers for heterostructures C and D were grown at 550°C with no overshoot. A growth pause and an additional annealing step at 540°C was used for heterostructure B to enhance

relaxation in the low-temperature grown buffer [37]. Both constant composition $In_{0.115}Ga_{0.885}As$ and $In_{0.145}Al_{0.855}As$ virtual substrates in heterostructure A and B were grown at 525°C, whereas $In_{0.24}Ga_{0.76}As$ virtual substrates in heterostructures C and D were grown at 550°C. Following immediate transfer to the group-IV chamber, unintentionally-doped epitaxial Ge was grown at 400°C at a nominal growth rate of $\simeq$0.067 Å/sec. For heterostructure D, a constant composition overlayer of $In_{0.24}Ga_{0.76}As$ was grown at 400°C to emulate a QW heterostructure, where lower temperature was used to prevent strain relaxation in the Ge epilayer.

3.2.2 Materials Characterization

Crystallinity, relaxation of the buffers, InAs composition in the constant composition virtual substrates and strain state of the epitaxial Ge layers were studied using high resolution x-ray diffraction (HR-XRD). Ex-situ symmetric (004) and asymmetric (115) reciprocal space maps and symmetric (004) rocking scans in the triple axis configuration were measured from each heterostructure using a PANalytical X'Pert Pro diffractometer equipped with PIXcel and proportional detectors, with a monochromatic Cu Kα_1 (λ = 1.540597 Å) x-ray source. Additional tensile strain estimation of epitaxial Ge layers was done using Raman spectroscopy in the backscattering (001) geometry on a JY Horiba LabRam HR800 system equipped with a 514.32 nm Ar^+ laser source, and the gratings of 1800 lines/mm were used during measurement. The laser power at the sample surface was $\simeq$10 mW. Surface morphology of the heterostructures was studied using a Bruker Dimension Icon atomic force microscopy (AFM) configured in the tapping mode. Subsequent stage tilt correction during AFM scans was performed using the native

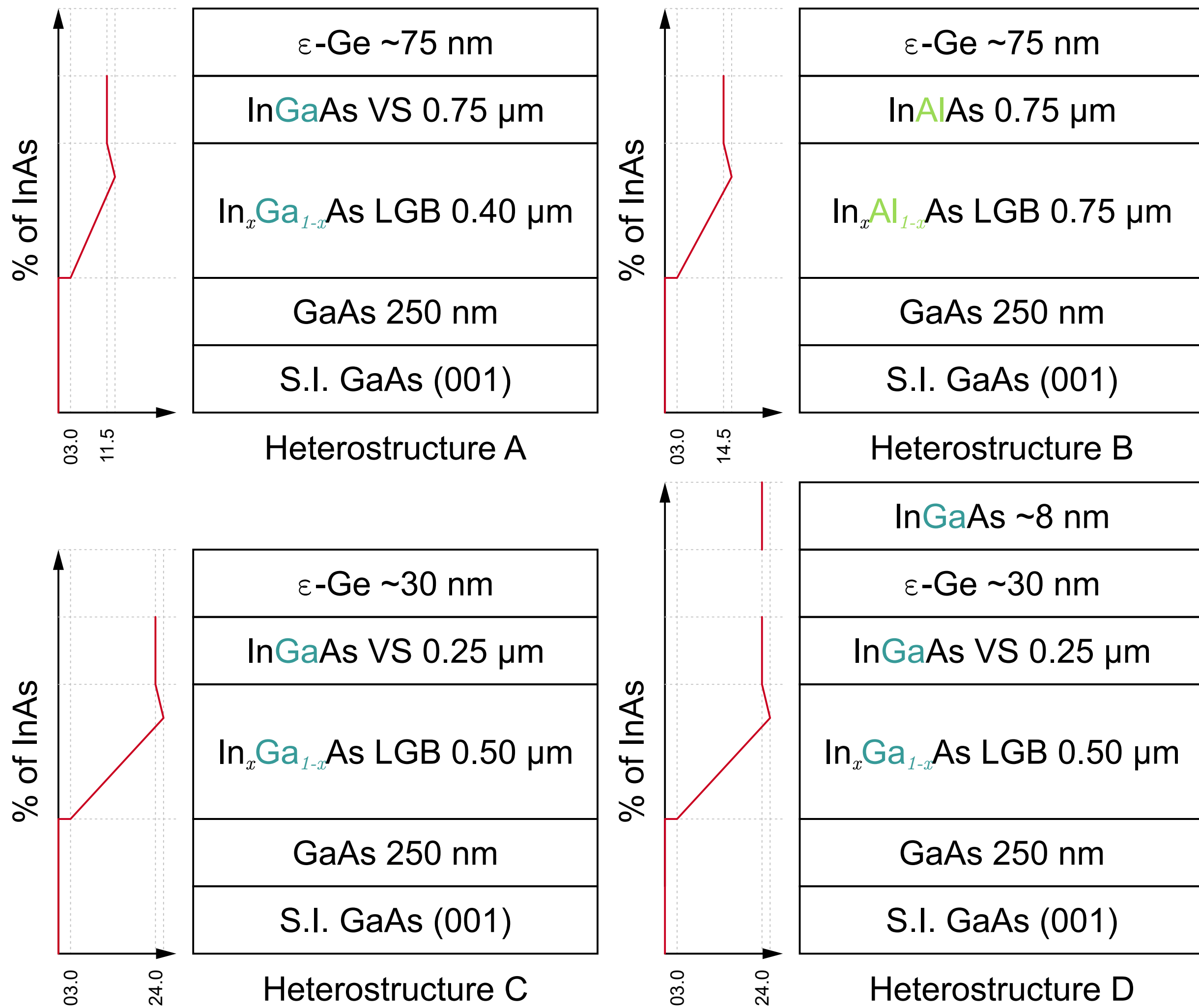

Figure 3.1: Representative schematics of the heterostructures studied in this work. Toward the left of each heterostructure, the InAs composition grading (solid red) with growth thickness is represented along with the estimated compositions from XRD analyses on the abscissa. The figure is not drawn to scale.

Nanoscope Analysis software package included in the Bruker AFM ecosystem. Finally, effective carrier lifetime of the strain engineered Ge epilayers were measured at room temperature ($\simeq$ 300 K) using a conventional microwave-reflectance photoconductive decay (μ-PCD) system at the National Renewable Energy Laboratory (NREL). Representative cleaved pieces of 1 cm $\times$ 1 cm from each heterostructure were placed under a waveguide (WR42 at 20 GHz, 0.43 cm $\times$ 1.07 cm) and optically excited using a Q-switched neodymium-doped yttrium aluminum garnet (Nd/YAG) laser. A wavelength (λ) of 1500 nm was chosen for the excitation to ensure homogenous excitation and photocarrier generation in the Ge epilayers. A nominal optical power of 20 mW was used, as measured by a power meter with an absorption disk diameter of 2 cm. A repetition rate of 10 pulses per second and pulse width of 5 ns was used. With the above, this resulted in a low injection level of 10^{14} cm$^{-3}\cdot$ sec^{-1}, calculated from the effective photon flux of 10^{17} sec^{-1}.

3.3 Results and Discussion

3.3.1 Analysis of strain state and InAs composition using HR-XRD

The schematics of the heterostructures investigated in this work are shown in Figure 3.1. Detailed crystalline and structural analysis was conducted on the heterostructures using HR-XRD measurements. Typical symmetric (004) and asymmetric (115) reciprocal space maps (RSMs) were recorded from each heterostructure for quantification of the

effective In incorporation in the virtual substrates and relaxation achieved in the buffer layers, and final strain state and crystalline quality of the ε-Ge epilayers. We have reported XRD measurements from heterostructure A in our previous work [38] and they are reported here to aid in direct comparison with heterostructure B.

3.3.1.1 Cation (Ga, Al) grading in InAs-based buffer

Plotted in reciprocal space coordinates, symmetric (004) RSMs recorded from heterostructures A and B are shown in Figures 3.2(a)-(b), respectively. For a symmetric (004) RSM, the iso-intensity contours from all epilayers should be aligned along the Q_x axis, in the absence of tilt or other finite crystal effects, as only the out-of-plane latticeparameter ($a_\perp$) is probed in this configuration. The reciprocal lattice contour centroids (RLCs) from the different epilayers would be displaced up or down while aligned along this axis. Figures 3.2(a)-(b) show a few important characteristics and distinctions between heterostructures A and B. First, the RLCs from the ε-Ge epilayers are vertically displaced above the GaAs RLCs in both heterostructures, suggesting a compressed in-plane lattice parameter, $a_\perp$, and stretched in-plane lattice parameter, $a_\parallel$, indicating successful transfer of tensile strain from the underlying buffer layers to Ge layer. Further, the difference in vertical position of the ε-Ge iso-intensity RLCs in the heterostructures indicates a slightly higher tensile strained Ge in heterostructure B than in heterostructure A. Another important observation is the difference in deviation of the epilayer RLCs from the $Q_x\,(00l) = 0$ line; larger deviations indicate larger amount of tilting with respect to the substrate orientation present in the epilayers. In this case, much larger tilting is observed in heterostructure B. This observation can shed light on

the relaxation dynamics originating during growth of the metamorphic buffers, which will be explored shortly. Finally, below the constant composition InGaAs and InAlAs RLCs, the observable RLCs are contributions from the overshoot composition layers incorporated to promote increased relaxation of the linearly graded buffers.

Since symmetric (004) reciprocal space maps yield information solely about the lattice spacing in the direction of growth, asymmetric (115) reciprocal space maps were also recorded from heterostructures A and B to obtain insight into the in-plane lattice spacing, $a_{\parallel}$. These scans are shown in Figures 3.2(c)-(d). The fully relaxed (R=1 in dotted red, denoting 100% relaxation) reference line is indicated as well. The RLCs of the individual epilayers should align along this line if the epilayers are fully relaxed and not tilted with respect to the substrate. Additionally, the fully strained line (R=0 dotted black, denoting fully strained epitaxy) is indicated as well to denote the vertical alignment of the Ge RLCs to the constant composition virtual substrate RLCs in each heterostructure. Due to the low angle of incidence used in an asymmetric scan, the corresponding RLCs of the epilayers are split further apart in the reciprocal space. In heterostructure A, the constant composition InGaAs virtual substrate RLC lies near the fully relaxed line, implying a high degree of symmetric relaxation. On the other hand, the large deviation of the constant composition InAlAs virtual substrate RLC in heterostructure B from the fully relaxed line suggests partial and/or asymmetric relaxation and presence of significant tilt in the film. However, it is important to note that the Ge epilayer RLC in heterostructure A is well aligned with the constant composition InGaAs virtual substrate RLCs along the Q_x axis, indicating that the Ge epilayer is pseudomorphically strained. We note that a minor misalignment of the Ge

epilayer with respect to the constant composition InAlAs virtual substrate in heterostructure B is present (*illustrated by the dotted red line connecting the epilayer RLCs*). The symmetric and confined nature of the RLCs of the constant composition virtual substrates indicate that defects generated from mismatched heteroepitaxy were generally contained within the linearly graded metamorphic buffers, thereby decreasing the propagation of dislocations to the Ge epilayers. Following the methodology outlined in refs [39] and [40], comprehensive quantification of the InAs molar fraction true to Vegard's law, residual strain in each constant composition virtual substrate, and tensile strain imparted to each Ge epilayer is carried out, and is reported in Table 3.1. The tensile strain for the Ge epilayers is determined to be $0.61 \pm 0.05\%$ and $0.66 \pm 0.05\%$, respectively, for heterostructure A and B, with the error being linked with finding the peak centroid for the corresponding epilayers. This agrees with the slightly larger vertical displacement of the Ge RLCs in heterostructure B compared to heterostructure A. A nominal InAs concentration of 11.5% and 14.5% is obtained from the constant composition InGaAs and InAlAs layers, respectively, which is again in line with the larger vertical displacement of the constant composition layer RLCs. The InAlAs constant composition virtual substrate, however, shows a higher degree of residual strain compared to the InGaAs constant composition virtual substrate. A moderately low tilt of $\simeq$142 arcsec is observed in heterostructure A, suggesting a symmetric buffer relaxation process during growth. The minor tilt is possibly due to the asymmetry originating from the difference in nucleation energy and glide velocity of group-V terminated α (along $\langle 1\bar{1}0 \rangle$) and group-III terminated β (along $\langle 110 \rangle$) dislocations [41, 42]. On the other hand, the observed tilt of $\simeq$1600 arcsec coupled with the high residual strain within the InAlAs metamorphic buffer suggests asymmetric strain relaxation and a large magnitude of

misfit dislocations with their Burgers vector aligned normal to the substrate orientation resulting in tilted epitaxy. Ternary $In_xAl_{1-x}As$ buffers are challenging to grow due to the large differences in adatom surface mobilities between Al and In, which naturally lends itself to increased difference in preferred nucleation and subsequent glide of α and β dislocations. Additionally, this disparity can lead to asymmetrical strain relaxation and therefore result in lattice tilt, as is observed in the case of heterostructure B. It is important to note that the presence of tilt can drastically distort the accurate measurement of strain state in the Ge epilayers *via* XRD. Thus, we have further assessed the strain in the Ge epilayers using Raman spectroscopy, as discussed in a subsequent section.

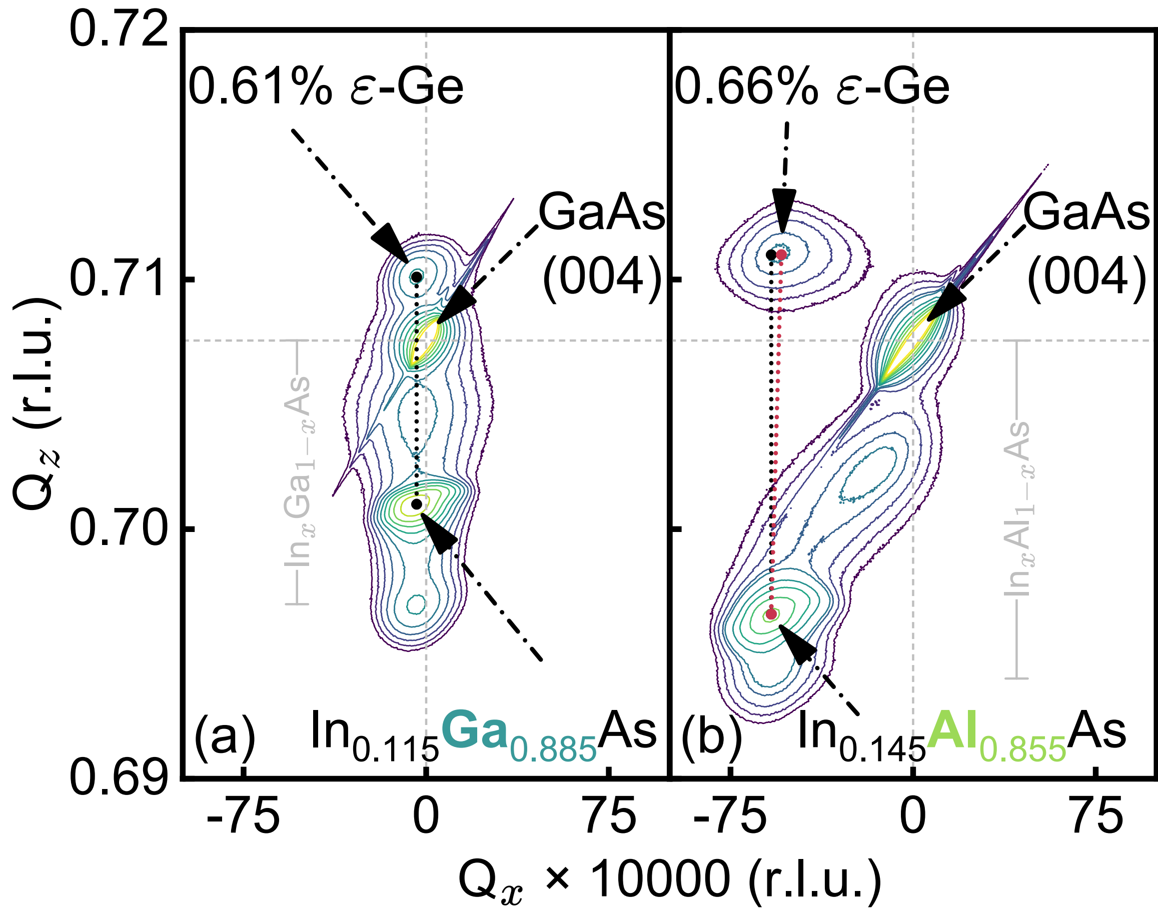

0.72
0.71
0.70
0.69
Q_z (r.l.u.)
0.61% ε-Ge
GaAs
(004)
In_xGa_1−xAs
(a)
In0.115Ga0.885As
0.66% ε-Ge
GaAs
(004)
In_xAl_1−xAs
(b)
In0.145Al0.855As
-75
0
75
-75
0
75
Q_x × 10000 (r.l.u.)

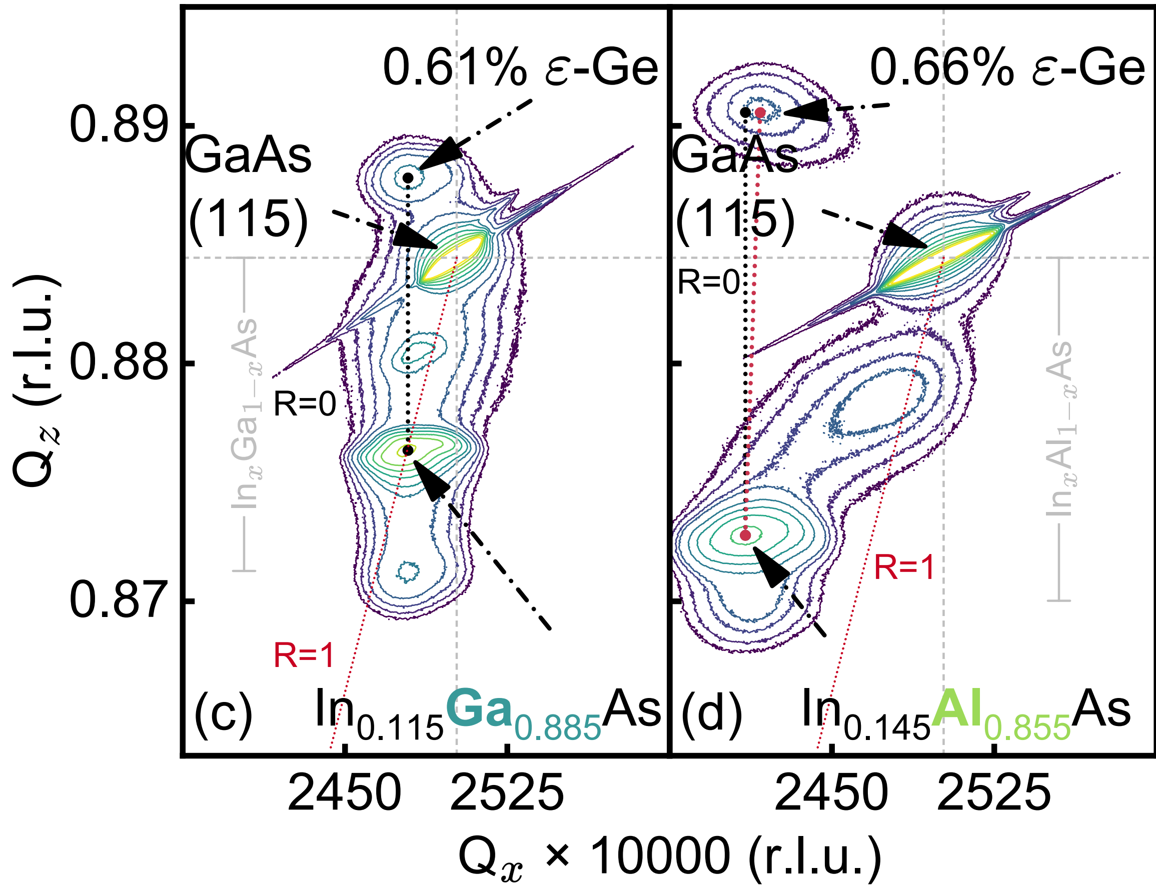

Figure 3.2: (a)-(b) Symmetric (004) RSMs obtained from heterostructures A35 and B, respectively. The alignment of the ε-Ge RLCs (black dotted) with the InGaAs and InAlAs virtual substrates confirms pseudomorphic epitaxy. (c)-(d) Asymmetric (115) RSMs obtained from heterostructures A [38] and B, respectively. The strained (R=0, dotted black) and relaxed (R=1, dotted red) lines are shown. The slight misalignment of the ε-Ge RLCs with the InAlAs RLC is indicated (dotted red).

3.3.1.2 Overlayer growth and strain state in (001) biaxially tensile strained Ge

As noted earlier, to actualize waveguides for the potential of optical communication, QW heterostructures are necessary such that the tensile strain engineered Ge epilayers are embedded between III-V cladding layers [35]. It is crucial to ensure that the Ge epilayer maintain the mechanical strain during the growth of the overlying layers. Therefore, to complement and compare to our previously published work [43], we have grown an InGaAs capping overlayer on top of the Ge epilayer to realize such a QW heterostructure. Symmetric (004) RSMs were recorded from heterostructures C and D, and the projection of the recorded intensities onto the $\Delta\theta$ axis is shown in Figure 3.3. Here, $\Delta\theta = \frac{\Delta(2\theta)}{2}$, and is the angular displacement of the epilayers with respect to the substrate, determined by their peak positions measured in Bragg scattering angle, 2θ. This way, the contributions to the contours from the different epilayers and the subsequent differences in peak positions can be directly observed and compared without the effect of tilt. We emphasize here that a lower temperature was utilized for growing the $In_{0.24}Ga_{0.76}As$ overlayer to ensure that the Ge epilayer does not relax during overlayer growth. As shown in Figure 3.3, the tensile strained Ge peaks from heterostructures C and D lie on the higher diffraction angles to the right of the GaAs substrate peak, in accordance with expansion (compression) of the $a_{\parallel}$ ($a_{\perp}$) lattice parameter because of the tensile strain imparted from the underlying buffer. The peak positions of the ε-Ge epilayers with respect to the GaAs substrate peak position (758.13108” (absolute 33.237°) and 800.69156” (absolute 33.249°), respectively, from heterostructure C and D) were determined using weighted Gaussian fits. A minimal difference of 42.56” in the Ge peak positions was observed, which results in $\left|\Delta a_{\perp,Het.C\ -Het.D}\right| = 0.00176$ Å, indicating

Table 3.1: Summary of extracted parameters from HR-XRD, XTEM and μ-PCD measurements, including τ_{eff} and goodness of fit (R^2) achieved from *unstrained* Ge and ε-Ge. The microwave pump source wavelength for μ-PCD measurements, carried out at 300 K, was kept constant at $\lambda = 1500$ nm for all samples.

		lattice parameters						tensile strain, ε		
het.	layer	$a_\perp$ (Å)	$a_\parallel$ (Å)	$a_{relaxed}$ (Å)	InAs molar fraction (%)	epilayer tilt (arcsec)	buffer relaxation (%)	XRD (%)	Raman (%)	theory (%)
A[38]	InGaAs	5.7065	5.6924	5.6998	11.5	-142	84			
	ε-Ge	5.6329	5.6864	5.6597		-115		0.61 ± 0.05	0.77 ± 0.08	0.74
B	InAlAs	5.7424	5.6954	5.7189	14.5	-1610	64			
	ε-Ge	5.6253	5.6910	5.6581		-1502		0.66 ± 0.05	0.82 ± 0.08	1.07

virtually no relaxation of the ε-Ge epilayer in heterostructure D, while also emphasizing the difference could stem from minor variations in InAs incorporation during growth of the InGaAs virtual substrates. Given that the strain state in the Ge epilayer remains unaltered post overlayer growth, one can expect coherent top and bottom heterointerfaces, and an essentially defect-free active ε-Ge epilayer. This marks a significant result in that strain engineered Ge QW heterostructures with tensile strains beyond the cross-over threshold [44] can be developed while maintaining prime material quality.

3.3.2 Strain State Estimation using Raman Spectroscopy

In addition to diffraction investigation, we employed Raman spectroscopy to measure the level of tensile strain in the Ge epilayers in heterostructures A and B. The effect of biaxial strain on phonon modes is extensively elucidated by Sui and Herman [45]. Essentially, biaxial strain in the (001) plane in diamond-cubic crystals causes the triply degenerate optical phonon modes at the center of the Brillouin zone to be split into a singlet and a doublet, with the eigenvectors perpendicular and parallel to the (001) plane, respectively. With the degeneracy lifted, an upshift (downshift) in the angular frequency of the singlet (doublet) is observed. In the (001) backscattering mode normally utilized in Raman spectroscopy, scattering from the doublet is forbidden by the principles of symmetry. As such, only the long-wavelength longitudinal optical (LO) mode is the active Raman mode detectable in this geometry. In addition, epilayer strain induces a shift of the singlet LO phonon frequency (Ω_s) and consequently, a shift in the Raman frequency is observed. Accordingly, this shift in the Raman active mode

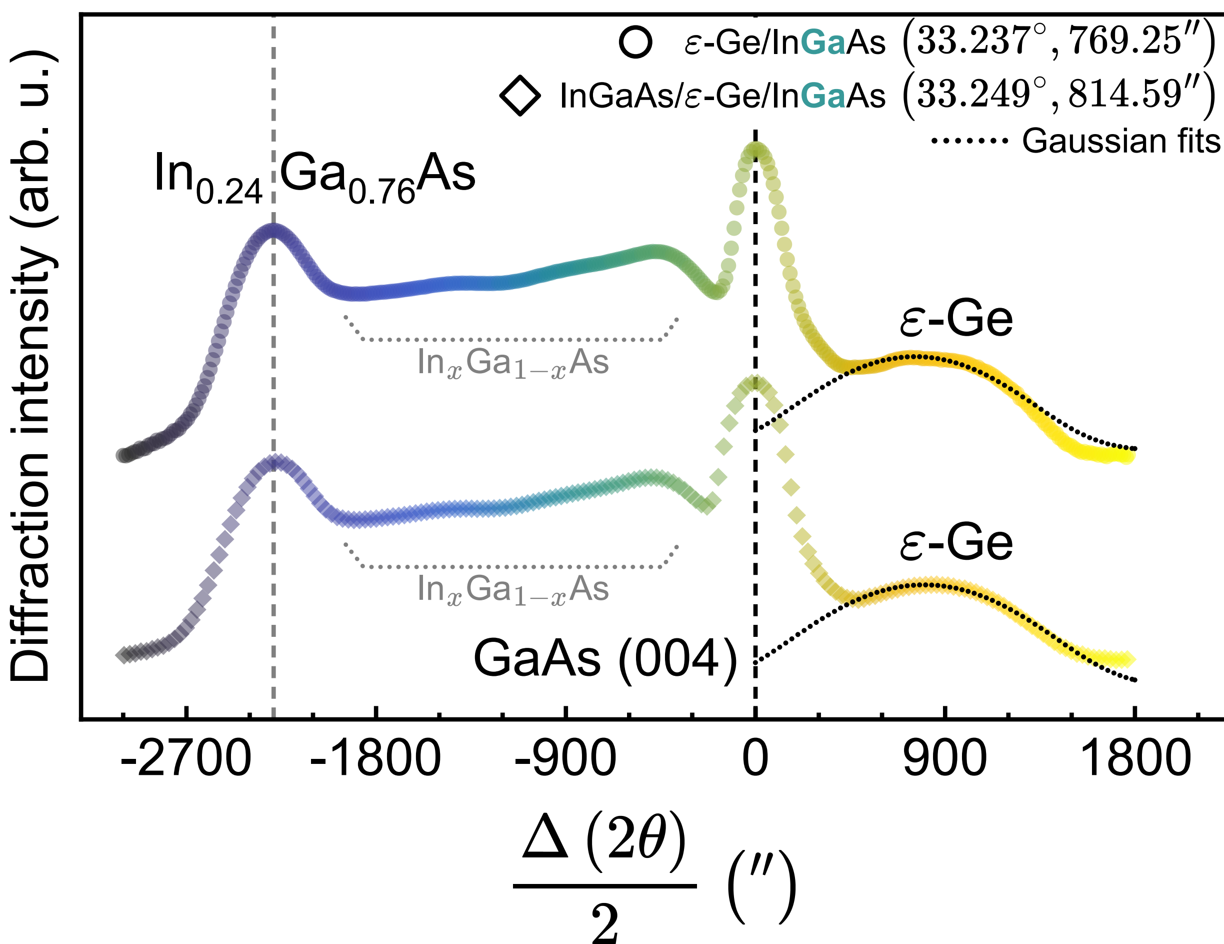

Figure 3.3: Projection of symmetric (004) RSM spectra to $\Delta\theta = \Delta(2\theta)/2$ axis recorded from heterostructures C and D. The peak positions of the ε-Ge epilayers were found using weighted Gaussian fits to the projection spectra. The Bragg peak positions (°) and full width at half maximum (FWHM) (arcsec, $''$) values obtained from the fits are included in the legend box.

frequency ($\Delta\omega$) because of (001) biaxial stress can be expressed in terms of stress tensors, σ_{xx} and σ_{yy}, and material specific elastic compliance tensor components S_{ij}, as follows:

$$\Delta\omega = \frac{1}{2\omega_0} \cdot [p \cdot S_{12} + q \cdot (S_{11} + S_{12})] \cdot \left(\sigma_{xx} + \sigma_{yy}\right). \tag{3.1}$$

Here, p and q are the optical phonon deformation potentials, and ω_0 is the frequency of the active Raman mode in the absence of mechanical stress. The relation can be further simplified to $\Delta\omega = b \cdot \varepsilon_{\parallel}$, given that $\sigma_{xx} = \sigma_{yy}$ in (001) biaxial stress, and that in such a formalism, the Raman shift is linear with strain, $\varepsilon_{\parallel}$. Here, $b = (q - p \cdot (C_{12}/C_{11}))/\omega_0$, where C_{ij} are material specific elastic constants and $\varepsilon_{\parallel}$ indicates in-plane strain. Such a simplification is made feasible under the assumption of a bi-isotropic tetragonal strain, which is the case in this study. Using material specific parameters from ref. [46], Fang *et al.* [47] calculated $b = -415 \pm 40$ cm^{-1}. Hence, a down shift (up shift) of the frequency of the Raman active mode should indicate the presence of tensile (compressive) strain within the material system. Figure 3.4 shows the measured Raman spectra obtained from heterostructures A and B, overlapped with Raman spectra obtained from (001) Ge substrate. Relative active Raman mode wavenumber offsets of -3.18 cm^{-1} and -3.41 cm^{-1} were obtained with respect to the (001) Ge substrate active Raman mode, respectively, from the Ge epilayers on heterostructures A and B. Accordingly, the effective tensile strain in the Ge epilayers were inferred to be $0.77 \pm 0.08\%$ and $0.82 \pm 0.08\%$, respectively. The term '*effective*' is used here to emphasize the difference in absolute values of strain estimated from XRD and Raman spectroscopy. The inset of Figure 3.4 demonstrates the relationship between the

measured relative shift and subsequently calculated tensile strain, and the estimated strain from XRD analysis. The shaded region represents the limits in estimates of strain from Raman spectroscopy arising from the uncertainty in the value of b, the fitting parameter. The results are also summarized in Table 3.1. As mentioned earlier, stemming from the anisotropic nature and different pathways of strain relaxation in the $In_xGa_{1-x}As$ and $In_xAl_{1-x}As$ metamorphic buffers, epilayer tilt might play a significant role in obscuring the accurate representation of measured strain *via* XRD. Since optical phonon modes contain information solely about the bond angles and bond lengths, and that in the presence of mechanical strain, bond angles and lengths are deformed, one could argue that relative shifts in Raman active modes might give a more realistic representation of strain in the epilayers. Considering a fully relaxed constant composition InGaAs and InAlAs, respectively, with InAs fraction of 11.5% and 14.5% as assessed from XRD (*close to the target compositions for this work*), the theoretical misfit can be derived to be $\varepsilon_{\parallel} \approx 0.74\%$ and $\varepsilon_{\parallel} \approx 1.07\%$, respectively. This brings about an intriguing observation; the strain state inferred from Raman spectroscopy in heterostructure A is closer to the theoretical misfit but deviates significantly in case of heterostructure B. Hoshina *et al.* [48] reported a comparable disparity between XRD and Raman spectroscopy in strain measurements, obtained from strained Ge grown on $In_xGa_{1-x}As$ metamorphic buffers. The authors observed that the deviation between XRD and Raman reported strain values was significantly higher in the high tensile strain region, starting around $\simeq$1% (001) biaxial strain. The phenomenological observation was explained based on the gradual relaxation of the strained Ge epilayers grown on InGaAs metamorphic buffers with thicknesses exceeding the critical layer thickness, h_c. The Ge epilayers in heterostructures A and B in this work are grown well within the critical layer thickness,

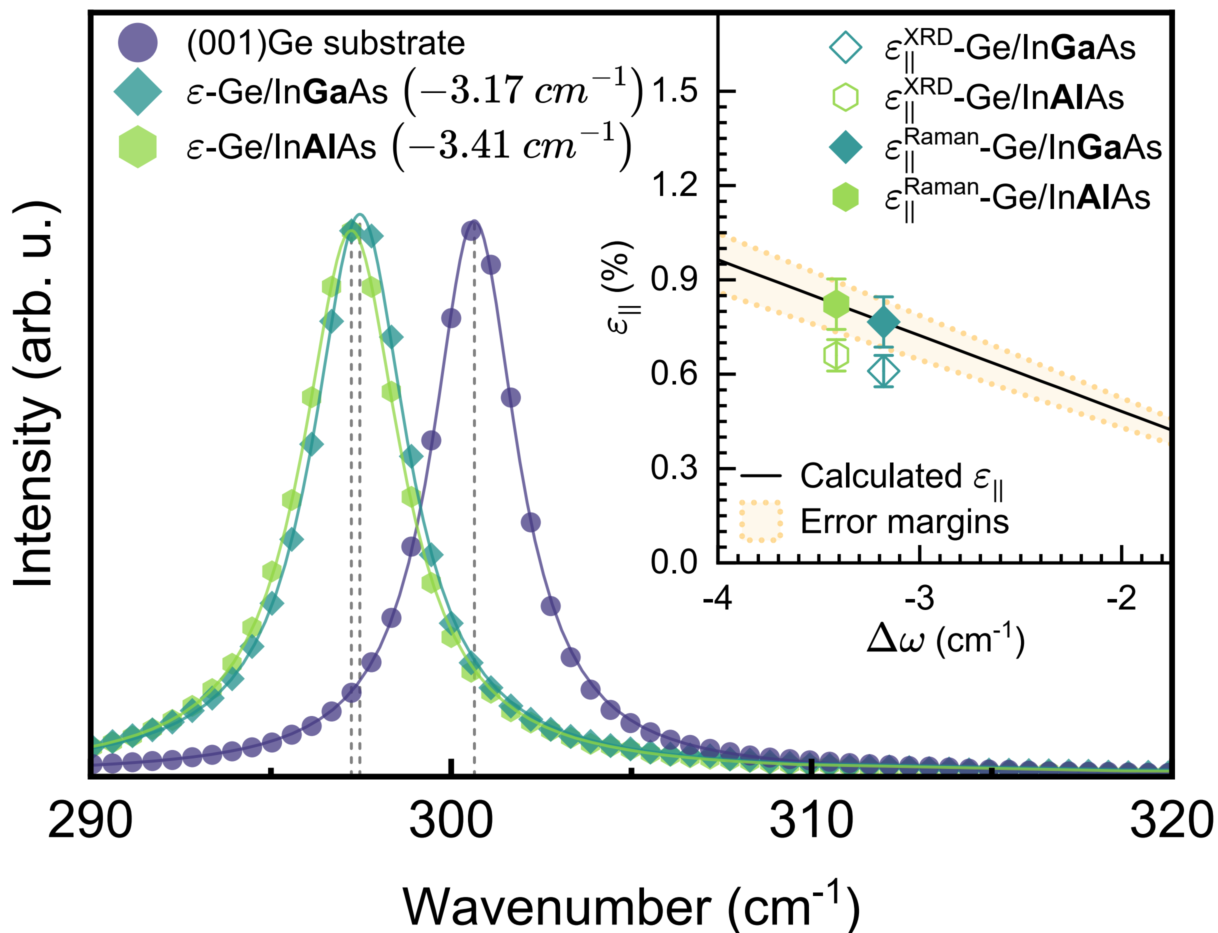

Figure 3.4: Raman spectra obtained from heterostructures A and B overlapped with Raman spectra recorded from (001)Ge substrate. Peak positions were found using Lorentzian fits to the spectra. The inset shows the strain relationship between the recorded Raman spectra and the tensile strain calculated using $\Delta\omega = b \cdot \varepsilon_{\|}$, where $\boldsymbol{b}$ and $\varepsilon_{\|}$ denote the fitting parameter and in-plane strain, respectively. The error margins for strain estimation are indicated by the shaded regions. In-plane tensile strain, $\varepsilon_{\|}$, estimated from XRD (Table 3.1) are also indicated by the corresponding symbols.

adhering to the strain balance model by People and Bean [49], and hence, are expected to be fully coherently strained. This is indeed observed in our previous work [38] where high magnification transmission electron micrographs obtained from the constant composition InGaAs virtual substrate, the ε-Ge epilayer and the ε-Ge/InGaAs heterointerface show a high degree of coherence and absence of misfit dislocations, alluding to the pseudomorphic epitaxy of Ge. the underlying mechanistic origins for the persistent disparity between strain estimates derived *via* XRD versus Raman spectroscopic assessment—particularly on InAlAs buffers—remain unresolved within the current study framework and warrant further experimental and theoretical investigation.

3.3.3 Surface Morphology *via* AFM

The topographical surface characteristics of heterostructures A and B were characterized *via* atomic force microscopy (AFM) due to its capacity to deliver high-resolution quantitative metrics pertaining to surface roughness and morphological uniformity—parameters instrumental in elucidating the underlying defect-mediated relaxation mechanisms operative during epitaxial growth processes. It is thoroughly substantiated within the literature that the mechanisms of excess strain energy alleviation in cubic (001)-oriented heteroepitaxy of metamorphic buffer layers predominantly manifest as a crosshatch surface morphology pattern [50]. As the thickness of any strained heteroepitaxial film surpasses the critical thickness, the accumulated elastic strain energy transcends that of the thermodynamically permitted strain energy density and the film undergoes plastic relaxation, thereby favoring the formation and subsequent glide of threading dislocations, which in turn form surface slip

steps, and segments of misfit dislocation at the heterointerface between the epilayer and the substrate. For heteroepitaxy of (001) oriented diamond or zinc blende cubic systems, the dominant class of slip systems is collectively referred to as $\frac{a}{2}\langle 110\rangle\{111\}$, where a is the lattice parameter [51]; hence, such threading dislocations glide along the $\{111\}$ slip planes in the $\langle 110\rangle$ directions. Consequently, there are eight such combinations of $\langle 110\rangle\{111\}$ systems that can take part in strain relaxation. At the growth front, the surface slip steps lead to local surface roughness; lateral mass transport, *i.e.* movement of adatoms to preferred step sites, and step-flow growth processes are initiated to remove this locally developed roughness. The trailing misfit segments along the heterointerface take part in relaxing the stress in the epilayer, while local stress is produced at the dislocation cores. Eventually, hillocks and valleys are formed because of the strain relaxation process which propagates along the dislocation lines near the heterointerface misfit dislocations. Several investigative works have reported on asymmetry in strain relaxation along the orthogonal $\langle 110\rangle$ directions and its effect on surface morphology. Another source of asymmetry, specifically in the case of low-mismatched compressive InGaAs heteroepitaxial growth on GaAs substrates, is the lower activation energy of dislocation nucleation and subsequent glide velocities for group-V terminated (α) dislocations than group-III terminated (β) dislocations, which are oriented along crystallographic $[1\bar{1}0]$ and $[110]$ directions, respectively. While this is equally true for InAlAs mismatched heteroepitaxy on GaAs, the large variation in surface adatom mobility between In and Al generally results in degraded surface morphology by virtue of phase separation and InAs and AlAs clustering [52].

AFM micrographs from heterostructures A and B are shown in Figure 3.5.

Heterostructure A, incorporating the InGaAs metamorphic buffer, exhibits a characteristic symmetric crosshatch pattern, which suggests a rather symmetrical relaxation process during the growth of the metamorphic buffer, as all eight slip systems seem to have contributed equally. This observation is further corroborated by the similar root-mean-squared roughness $\left(R_q\right)$ values of 1.156 nm and 1.091 nm along the orthogonal $[1\bar{1}0]$ and [110] directions, respectively. Consequently, the representative region shown exhibits a smooth surface with a modest $\left(R_q\right)$ value of 1.289 nm. In contrast, heterostructure B, with the InAlAs metamorphic buffer, displays a randomized rough pattern with a significantly higher $\left(R_q\right)$ of 6.303 nm. Additionally, no clear crosshatch pattern is visible in the representative region.

It is important to emphasize that the strain relaxation mechanism occurring in heteroepitaxial systems with lattice mismatch is profoundly influenced by the epitaxial growth temperature parameters as well as by the discrepancy in adatom surface diffusion mobilities. For heterostructure A, an epitaxial deposition temperature of 525°C was feasible, owing to the comparable adatom surface mobilities of In and Ga in this temperature range. Conversely, to attenuate the disparity in adatom surface diffusion coefficients between In and Al, an adjusted lower substrate temperature of 420°C was employed during the epitaxial growth of the linearly graded $In_xAl_{1-x}As$ metamorphic buffer. Prior to the deposition of the constant composition InAlAs VS, an *in-situ* thermal annealing was carried out at an elevated temperature of 540°C for a duration of 900 seconds, with the objective of of inducing enhanced strain relaxation within the linearly graded buffer, thereby attenuating potential tilt components and compositional heterogeneities typically associated with low-temperature buffer growth regimes [37].

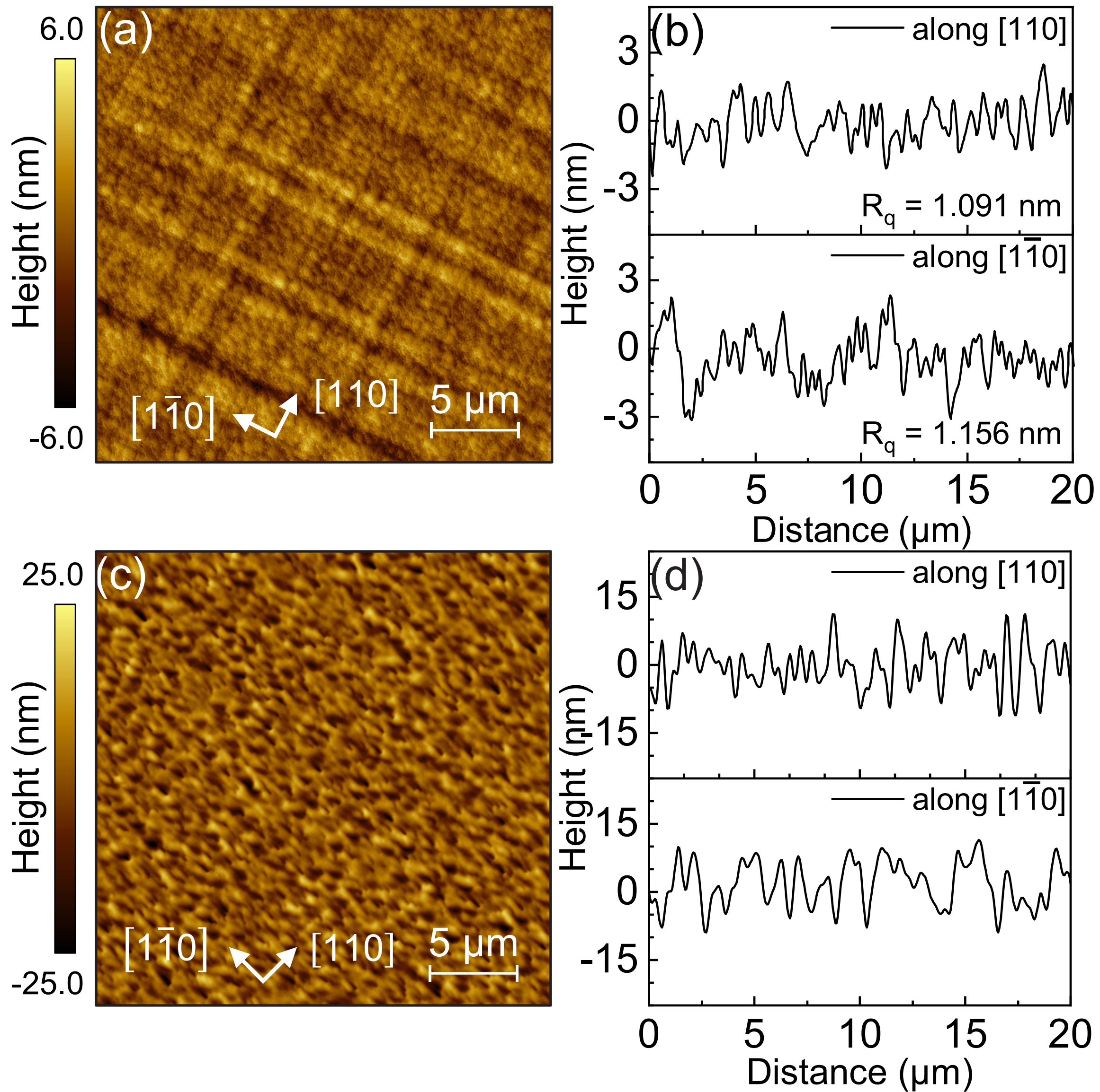

Figure 3.5: (a) and (c) Atomic force micrographs of $20\mu m \times 20\mu m$ representative regions obtained from heterostructures A and B, respectively. The orthogonal directions $\langle 110 \rangle$ are indicated. (b) and (d) Line profile scans showing the height variations along the orthogonal directions. Orthogonal R_q values for heterostructure B are not reported in (d) due to absence of observable cross-hatch.

These observations are corroborated by the findings of Chyi *et al.* [53], who reported increased surface roughness in InAlAs buffers grown within the temperature window of 420°C to 520°C—whether linearly graded or step-graded—relative to all InGaAs variants processed under comparable thermal budget and with similar InAs compositional parameters. Given the observed limited strain relaxation within the $In_xAl_{1-x}As$ buffer layer and the marginally increased substrate misorientation evidenced *via* HR-XRD analysis, the elevated surface topography and roughness measured in heterostructure B can be systematically ascribed to the following contributory factors: (i) reduced epitaxial growth temperature, which significantly constrains the surface diffusion mobility of Al adatoms relative to In adatoms, thus fostering the formation of InAs- and AlAs-rich microregions on the surface front, leading to local compositional modulation, surface heterogeneity, and progressive augmentation of topographical irregularities with increasing layer thickness; (ii) a marginally higher substrate misorientation angle relative to the [001] growth axis, as determined through HR-XRD, which introduces additional atomic step densities and surface step arrays [54], thereby increasing the density of potential dislocation nucleation sites, modifying the critical resolved shear stress across multiple slip systems, and favoring specific slip planes for dislocation nucleation and glide that are energetically preferred during strain alleviation [42]; and (iii) a pronounced disparity in the nucleation and glide activity of dislocation types, particularly favoring the formation and propagation of α-type dislocations over β-type, owing to energetic biasing mechanisms [55].

It is well established that increased surface roughness acts as trapping centers and recombination sites for charge carriers, critically impacting carrier dynamics and transport

properties. Consequently, the subsequent investigation focuses on quantifying the effective minority carrier lifetime, (τ_{eff}), within these ε-Ge heterostructures utilizing non-contact μ-PCD measurements.

3.3.4 Effective Carrier Lifetime Analysis *via* μ-PCD

Material quality exerts a profound influence on the defect-limited minority carrier lifetime $\tau_{SRH} \approx \tau_{eff}$, which is governed by Shockley-Read-Hall (SRH) recombination kinetics. This parameter serves as a critical indicator of the material's suitability for integration into semiconductor device architectures [56, 57]. The presence of intrinsic and extrinsic point and extended defects, as well as impurity states within the crystalline lattice or bulk matrix, introduces localized energy levels within the bandgap that function as carrier traps and nonradiative recombination centers, thereby markedly reducing τ_{SRH}. Furthermore, surface topography characterized by deviations from ideal smoothness—commonly described as surface roughness—plays a significant detrimental role by increasing scattering and facilitating the formation of surface recombination pathways, especially in cases where the active layers remain unpassivated, resulting in a pronounced diminution of carrier lifetime [58]. The most prevalent methodology for the non-destructive, rapid quantification of minority carrier lifetimes is the micro-photoconductance spectroscopy (μ-PCD) technique. This approach enables contactless acquisition and analysis of carrier recombination dynamics, effectively bypassing the need for complex microfabrication procedures that could introduce fabrication-induced defects or contamination, thereby preserving the material's intrinsic quality [59–61].

In operation, incident optical excitation generates excess photogenerated carriers within the semiconductor matrix. Upon cessation of illumination, the local excess carrier concentration gradient initiates a diffusion flux of minority carriers away from the excitation locus. This process proceeds until recombination mechanisms—Shockley-Read-Hall, radiative, Auger, or surface recombination—diminish the excess carrier population to equilibrium levels. These temporal carrier density variations induce fluctuations in the local electrical conductance (σ), which can be spatially probed *via* microwave reflectance techniques employing a microwave source coupled with a probing source. The measured changes in conductance as a function of time directly reflect carrier recombination kinetics.

Furthermore, by selectively tuning the wavelength of the optical excitation source, it is possible to probe different spatial regions within heterostructures—surface, interface, or bulk regions—allowing for the independent characterization of surface versus bulk recombination processes. This spectral selectivity facilitates the elucidation of recombination pathways that predominantly influence the carrier lifetime in regions distant from surface defect states and interface traps [62]. For this work, we have used the μ-PCD technique to characterize the effect of the underlying buffer and top overgrowth on the effective carrier lifetime in the ε-Ge epilayers. Details of the measurement technique have been reported in our previous work [38]. Under low-injection conditions, it can be shown that the reciprocal of effective carrier lifetime, τ_{eff}, is expressed as the cumulative response from two reciprocal components, $\tau_{surface}$ and τ_{bulk}, as follows [63, 64]:

$$\frac{1}{\tau_{eff}} = \frac{1}{\tau_{surface}} + \frac{1}{\tau_{bulk}} \tag{3.2}$$

where $\tau_{surface}$ and τ_{bulk} are effective lifetime components from the surface and the bulk, respectively. Intrinsic and extrinsic defect states, as well as other non-idealities present within the volume of the epitaxial layer, induce non-radiative recombination pathways that quantitatively diminish the effective minority charge carrier lifetime (τ_{eff}). When such volumetric recombination centers dominate, τ_{eff} is primarily constrained by bulk defect densities, rendering τ_{eff} of the material bulk-limited. Conversely, recombination phenomena localized at or near the material surface—such as surface dangling bonds due to insufficient passivation or exacerbation of surface topological features, or interface state distributions (D_{it})—contribute to the surface recombination velocity component, resulting in a surface-limited effective carrier lifetime regime. Despite the fundamental nature of these recombination mechanisms, this theoretical understanding underpins the strategic evaluation of how buffer layer architectures and overlayer deposition processes influence charge carrier dynamics within epitaxially grown ε-Ge layers, as examined in the upcoming sub-sections.

3.3.4.1 Effect of strain template on (001) biaxially tensile strained Ge

Figure 3.6(a) shows typical μ-PCD transients obtained from ε-Ge epilayers grown on heterostructures A and B. The absorption coefficient of Ge ($\alpha \approx 2.5 \times 10^4$ cm^{-1}) at the used excitation wavelength of λ = 1500 nm ensures that the excess photocarriers are generated homogeneously throughout the Ge epilayer. Additionally, the underlying

layers are transparent to the excitation at this wavelength, which ensures exclusive observation of the carrier dynamics within the Ge epilayers. The effective carrier lifetime (τ_{eff}), obtained by fitting an exponential decay regression to the principal mode of decay [63], is substantially higher in ε-Ge grown on InGaAs metamorphic buffer ($\tau_{eff} \approx 68$ ns) compared to its counterpart grown on InAlAs metamorphic buffer ($\tau_{eff} \approx 13$ ns). This observation can be explained as follows: when a semi-infinite crystal terminates at the surface, the potential energy at the surface is starkly different from that in the bulk of the material, where periodicity of the crystal lattice is maintained. This termination leads to unsatisfied, dangling bonds on the surface that can participate in recombination dynamics. Conversely, an increase in the surface roughness can be considered as an increase in the effective surface area and thus increase in surface recombination centers, due to the undulations. Thus, one can expect an increase in the rate of carrier recombination at the surface. In this case, when the optical source is removed, the generated photocarriers quickly diffuse toward the surface and recombine. While thickness of the epilayer can also influence the effective lifetime, with longer effective lifetime typically observed in thicker epilayers, the Ge epilayers are of the same thickness in this work and as such, thickness effects can be neglected. Therefore, it is modest to conclude that the observed difference in effective carrier lifetime is primarily due to the difference in surface topology, and possible difference in electronic nature of the interfacial defects at the ε-Ge/InAlAs and ε-Ge/InGaAs heterointerfaces. It follows that in an epilayer with a rough terminating surface/interface, higher surface recombination velocity results in reduced effective lifetime, and vice versa. In view of the above discussion, the reduced effective lifetime in ε-Ge grown on InAlAs metamorphic buffer corresponds well to our AFM findings and further corroborates the XRD results, wherein

a high degree of incomplete strain relaxation and asymmetric relaxation induced poor surface morphology. Likewise, the symmetric strain relaxation of the InGaAs metamorphic buffer resulted in a smoother surface morphology, and leads to enhanced effective carrier lifetime, τ_{eff} in the ε-Ge grown in heterostructure A.

3.3.4.2 Effect of overlayer growth on (001) biaxially tensile-strained Ge

We have further used μ-PCD to study the effect of the symmetric constant composition InGaAs overlayer on top of the ε-Ge epilayer. We previously noted in the XRD section that there was no apparent relaxation in the ε-Ge epilayer based on the positions of the diffraction peaks. Figure 3.6(b) shows typical PCD transients obtained from heterostructures C and D. The excitation wavelength for this case is kept at $\lambda = 1500nm$ for reasons cited above. As seen in Figure 3.6(b), the modest but measurable reduction in effective carrier lifetime in heterostructure D ($\tau_{eff,Het.D} \approx 76\ ns$, compared to $\tau_{eff,Het.C} \approx 99\ ns$) could possibly be due to (i) inadequate surface passivation by the overlying InGaAs layer; (ii) effect of low temperature growth of constant composition InGaAs overlayer resulting in a rougher heterointerface shared with the Ge epilayer; or (iii) presence of electrically active antiphase boundaries between antiphase domains resulting from the growth of polar InGaAs on non-polar Ge. This qualitative assumption is justified from the quicker decay of the transient curve in the capped sample, as the initial roll-off is exclusively dependent on the surface component [63] of the lifetime expression in Eqn 3.2. Thus, following from the above discussion and the observation from Figure 3.3, it is modest to conclude that: (i) the tensile strain in the capped Ge epilayer is not relaxed; (ii) the bulk lifetime in

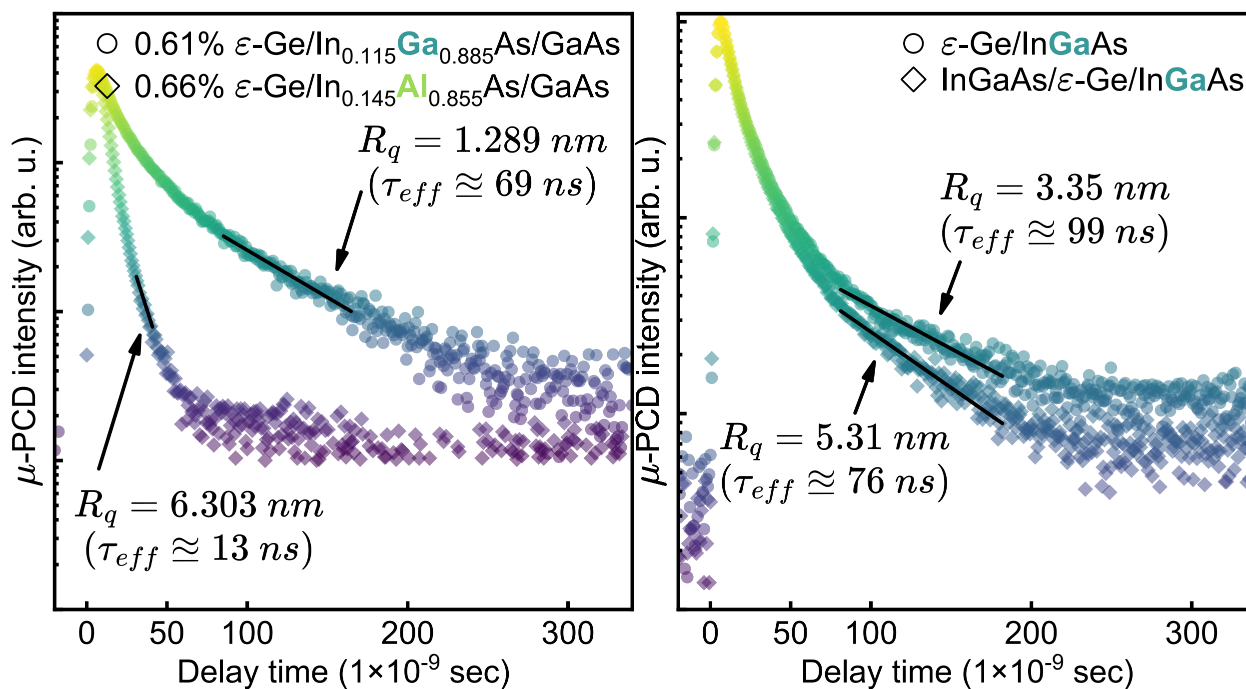

Figure 3.6: μ-PCD transient curves recorded from (a) Heterostructures A [38] and B and (b) Heterostructures C and D, respectively. The effective lifetime is obtained in each case by fitting an exponential regression to the principal mode of decay (solid black).

ε-Ge epilayer is most likely not affected by the overgrowth of the InGaAs epilayer, and (iii) the measurable reduction of the effective lifetime is a direct consequence of the surface properties of the top heterointerface. To the best of our knowledge, the experimental characterization of carrier recombination dynamics within ε-Ge QW double heterostructures utilizing μ-PCD has not been previously documented or reported. The findings from this work represent a significant milestone in the advancement toward the fabrication and optimization of high-quality Ge-based heterostructures, a critical prerequisite for the development of optoelectronic devices and integrated optical sources predicated on Ge semiconductor platforms.

Prior numerical modeling investigations [65] have demonstrated that theoretical internal quantum efficiency (IQE) metrics exhibit an enhancement factor of approximately 100 when the defect-limited non-radiative lifetime, $\tau_{SRH} \approx \tau_{bulk}$ is increased from 10 ns to 100 ns, under conditions of 2.0% tensile strain and moderate n-type doping concentration of 5×10^{18} cm^{-3}. This correlation underscores the critical dependence of IQE on intrinsic lifetime parameters, thereby motivating targeted improvements in crystalline material quality to mitigate defect densities. Analogously, our experimental data corroborate that highly crystalline ε-Ge can be achieved through epitaxial growth of III-V compound semiconductors on metamorphic buffer layers, thereby establishing a viable synthetic pathway for the fabrication of QW double heterostructures, emphasizing their potential in the development of integrated laser and light-emitting diode (LED) sources with enhanced radiative efficiencies.

3.4 Conclusion

In summary, this work reports on the differences in structural crystallinity and carrier dynamics of ε-Ge grown on InGaAs and InAlAs metamorphic buffers, and InGaAs/ε-Ge/InGaAs QW double heterostructures. While symmetric strain relaxation and a smooth surface morphology could be achieved on ε-Ge grown *via* InGaAs metamorphic buffers, ε-Ge grown *via* InAlAs metamorphic buffers were characterized by rough surface morphology owing to asymmetric strain relaxation during buffer growth. High-resolution XRD analyses confirmed the efficacy of the metamorphic buffers in reducing dislocation propagation to the active Ge layer. Notably, the strain state evaluation derived *via* HR-XRD and Raman scattering methodologies revealed quantitative discrepancies; despite this, the incorporation of tensile strain while maintaining pseudomorphic coherence was substantiated in ε-Ge in both heteroepitaxial configurations. Furthermore, surface morphology assessment using AFM corresponds well to the HR-XRD analyses, with higher symmetric relaxation correlating to smoother surface morphology (reduced R_q) in ε-Ge grown on InGaAs metamorphic buffers. Carrier dynamics studied using μ-PCD showed that effective lifetime is degraded due to increased surface roughness, corroborating the premise that increased surface roughness acts as a non-radiative recombination pathway. These findings position $In_xGa_{1-x}As$ as a preferable metamorphic pathway for strained heteroepitaxy. Furthermore, we showed that the strain state of Ge in a QW heterostructure remained substantially invariant after InGaAs overlayer growth, with slight degradation of effective carrier lifetime, alluding to the prime quality of ε-Ge epilayers. These results bear practical implications for realization of strain-engineered Ge for the goal of realizing inter- and intra-chip

communications and strained Ge-based optical sources.

Bibliography

[1] S. Bhattacharya, S. W. Johnston, R. J. Bodnar, and M. K. Hudait, "Elucidating the Role of InGaAs and InAlAs Buffers on Carrier Dynamics of Tensile-Strained Ge Double Heterostructures," *ACS Applied Electronic Materials*, vol. 6, no. 6, pp. 4247–4256, Jun. 2024, ISSN: 2637-6113. DOI: 10.1021/acsaelm.4c00347.

[2] R. Chau, B. Doyle, S. Datta, J. Kavalieros, and K. Zhang, "Integrated Nanoelectronics for the Future," *Nature Materials*, vol. 6, no. 11, pp. 810–812, Nov. 2007, ISSN: 1476-4660. DOI: 10.1038/nmat2014.

[3] K. J. Kuhn, "Considerations for Ultimate CMOS Scaling," *IEEE Transactions on Electron Devices*, vol. 59, no. 7, pp. 1813–1828, 2012, ISSN: 1557-9646. DOI: 10.1109/TED.2012.2193129.

[4] A. R. Goi, K. Syassen, and M. Cardona, "Direct-band-gap absorption in germanium under pressure," *Physical Review B*, vol. 39, no. 17, pp. 12 921–12 924, 1989, PRB. DOI: 10.1103/PhysRevB.39.12921.

[5] S. Gupta, B. Magyari-Köpe, Y. Nishi, and K. C. Saraswat, "Achieving direct band gap in germanium through integration of Sn alloying and external strain," *Journal of Applied Physics*, vol. 113, no. 7, 2013, ISSN: 0021-8979. DOI: 10.1063/1.4792649.

[6] R. Geiger, T. Zabel, E. Marin, A. Gassenq, J.-M. Hartmann, J. Widiez, J. Escalante, K. Guilloy, N. Pauc, and D. Rouchon, "Uniaxially stressed germanium with fundamental direct band gap," *arXiv preprint arXiv:1603.03454*, 2015. DOI: 10.48550/arXiv.1603.03454.

[7] R. Pillarisetty, “Academic and Industry Research Progress in Germanium Nanodevices,” *Nature*, vol. 479, no. 7373, pp. 324–328, Nov. 2011, ISSN: 1476-4687. DOI: 10.1038/nature10678.

[8] T. Ghani, M. Armstrong, C. Auth, M. Bost, P. Charvat, G. Glass, T. Hoffmann, K. Johnson, C. Kenyon, J. Klaus, B. McIntyre, K. Mistry, A. Murthy, J. Sandford, M. Silberstein, S. Sivakumar, P. Smith, K. Zawadzki, S. Thompson, and M. Bohr, “A 90nm High Volume Manufacturing Logic Technology Featuring Novel 45nm Gate Length Strained Silicon Cmos Transistors,” in *IEEE International Electron Devices Meeting 2003*, pp. 11.6.1–11.6.3. DOI: 10.1109/IEDM.2003.1269442.

[9] K. Mistry, M. Armstrong, C. Auth, S. Cea, T. Coan, T. Ghani, T. Hoffmann, A. Murthy, J. Sandford, R. Shaheed, K. Zawadzki, K. Zhang, S. Thompson, and M. Bohr, “Delaying forever: Uniaxial strained silicon transistors in a 90nm CMOS technology,” in *Digest of Technical Papers. 2004 Symposium on VLSI Technology, 2004.*, IEEE, 2004, pp. 50–51. DOI: 10.1109/VLSIT.2004.1345387.

[10] J. Liu, X. Sun, R. Camacho-Aguilera, L. C. Kimerling, and J. Michel, “Ge-on-Si laser operating at room temperature,” *Optics Letters*, vol. 35, no. 5, pp. 679–681, 2010. DOI: 10.1364/OL.35.000679.

[11] K. H. Koo, H. Cho, P. Kapur, and K. C. Saraswat, “Performance Comparisons Between Carbon Nanotubes, Optical, and Cu for Future High-Performance On-Chip Interconnect Applications,” *IEEE Transactions on Electron Devices*, vol. 54, no. 12, pp. 3206–3215, 2007, ISSN: 1557-9646. DOI: 10.1109/TED.2007.909045.

[12] K. Saraswat, D. Kim, T. Krishnamohan, D. Kuzum, A. K. Okyay, A. Pethe, and H.-Y. Yu, “Germanium for High Performance MOSFETs and Optical

Interconnects," *ECS Transactions*, vol. 16, no. 10, pp. 3–12, 2008, ISSN: 1938-5862 1938-6737. DOI: 10.1149/1.2986748.

[13] P. Chaisakul, D. Marris-Morini, J. Frigerio, D. Chrastina, M.-S. Rouifed, S. Cecchi, P. Crozat, G. Isella, and L. Vivien, "Integrated Germanium Optical Interconnects on Silicon Substrates," *Nature Photonics*, vol. 8, no. 6, pp. 482–488, 2014, ISSN: 1749-4893. DOI: 10.1038/nphoton.2014.73.

[14] W. van Roosbroeck and W. Shockley, "Photon-Radiative Recombination of Electrons and Holes in Germanium," *Physical Review*, vol. 94, no. 6, pp. 1558–1560, 1954, PR. DOI: 10.1103/PhysRev.94.1558.

[15] M. Virgilio, C. L. Manganelli, G. Grosso, G. Pizzi, and G. Capellini, "Radiative recombination and optical gain spectra in biaxially strained *n*-type germanium," *Physical Review B*, vol. 87, no. 23, p. 235 313, 2013, PRB. DOI: 10.1103/PhysRevB.87.235313.

[16] J. Liu, X. Sun, D. Pan, X. Wang, L. C. Kimerling, T. L. Koch, and J. Michel, "Tensile-strained, *n*-type Ge as a gain medium for monolithic laser integration on Si," *Optics Express*, vol. 15, no. 18, pp. 11 272–11 277, 2007. DOI: 10.1364/OE.15.011272.

[17] M. E. Kurdi, G. Fishman, S. Sauvage, and P. Boucaud, "Band structure and optical gain of tensile-strained germanium based on a 30 band $\vec{k} \cdot \vec{p}$ formalism," *Journal of Applied Physics*, vol. 107, no. 1, p. 013 710, 2010. DOI: 10.1063/1.3279307.

[18] B. Dutt, D. S. Sukhdeo, D. Nam, B. M. Vulovic, Z. Yuan, and K. C. Saraswat, "Roadmap to an Efficient Germanium-on-Silicon Laser: Strain vs. *n*-Type Doping,"

IEEE Photonics Journal, vol. 4, no. 5, pp. 2002–2009, 2012, ISSN: 1943-0655. DOI: 10.1109/jphot.2012.2221692.

[19] J. Liu, “Monolithically Integrated Ge-on-Si Active Photonics,” *Photonics*, vol. 1, no. 3, pp. 162–197, 2014, ISSN: 2304-6732. DOI: 10.3390/photonics1030162.

[20] R. Geiger, T. Zabel, and H. Sigg, “Group IV Direct Band Gap Photonics: Methods, Challenges, and Opportunities,” *Frontiers in Materials*, vol. 2, 2015, ISSN: 2296-8016. DOI: 10.3389/fmats.2015.00052.

[21] E. Kasper, M. Kittler, M. Oehme, and T. Arguirov, “Germanium tin: silicon photonics toward the mid-infrared [Invited],” *Photonics Research*, vol. 1, no. 2, pp. 69–76, Jul. 2013, ISSN: 2327-9125. DOI: 10.1364/PRJ.1.000069.

[22] M. El Kurdi, H. Bertin, E. Martincic, M. de Kersauson, G. Fishman, S. Sauvage, A. Bosseboeuf, and P. Boucaud, “Control of direct band gap emission of bulk germanium by mechanical tensile strain,” *Applied Physics Letters*, vol. 96, no. 4, 2010, ISSN: 0003-6951. DOI: 10.1063/1.3297883.

[23] A. Gassenq, K. Guilloy, G. O. Dias, N. Pauc, D. Rouchon, J.-M. Hartmann, J. Widiez, S. Tardif, F. Rieutord, J. Escalante, I. Duchemin, Y.-M. Niquet, R. Geiger, T. Zabel, H. Sigg, J. Faist, A. Chelnokov, V. Reboud, and V. Calvo, “1.9% bi-axial Tensile Strain in Thick Germanium Suspended Membranes Fabricated in Optical Germanium-On-Insulator Substrates for Laser Applications,” *Applied Physics Letters*, vol. 107, no. 19, p. 191 904, 2015. DOI: 10.1063/1.4935590.

[24] R. W. Millar, K. Gallacher, J. Frigerio, A. Ballabio, A. Bashir, I. MacLaren, G. Isella, and D. J. Paul, “Analysis of Ge micro-cavities with in-plane tensile strains

above 2%," *Optics Express*, vol. 24, no. 5, pp. 4365–4374, 2016. DOI: 10.1364/OE.24.004365.

[25] J. R. Jain, A. Hryciw, T. M. Baer, D. A. B. Miller, M. L. Brongersma, and R. T. Howe, "A micromachining-based technology for enhancing germanium light emission via tensile strain," *Nature Photonics*, vol. 6, no. 6, pp. 398–405, 2012, ISSN: 1749-4893. DOI: 10.1038/nphoton.2012.111.

[26] A. Ghrib, M. El Kurdi, M. Prost, S. Sauvage, X. Checoury, G. Beaudoin, M. Chaigneau, R. Ossikovski, I. Sagnes, and P. Boucaud, "All-Around SiN Stressor for High and Homogeneous Tensile Strain in Germanium Microdisk Cavities," *Advanced Optical Materials*, vol. 3, no. 3, pp. 353–358, 2015, ISSN: 2195-1071. DOI: 10.1002/adom.201400369.

[27] V. Reboud, A. Gassenq, N. Pauc, J. Aubin, L. Milord, Q. M. Thai, M. Bertrand, K. Guilloy, D. Rouchon, J. Rothman, T. Zabel, F. A. Pilon, H. Sigg, A. Chelnokov, J. M. Hartmann, and V. Calvo, "Optically pumped GeSn micro-disks with 16% Sn lasing at 3.1 μm up to 180K," *Applied Physics Letters*, vol. 111, no. 9, p. 092 101, 2017. DOI: 10.1063/1.5000353.

[28] Q. Chen, L. Zhang, Y. Song, X. Chen, S. Koelling, Z. Zhang, Y. Li, P. M. Koenraad, J. Shao, C. S. Tan, S. Wang, and Q. Gong, "Highly Tensile-Strained Self-Assembled Ge Quantum Dots on InP Substrates for Integrated Light Sources," *ACS Applied Nano Materials*, vol. 4, no. 1, pp. 897–906, 2021. DOI: 10.1021/acsanm.0c03373.

[29] Y. Huo, H. Lin, R. Chen, Y. Rong, T. I. Kamins, and J. S. Harris, "MBE growth of tensile-strained Ge quantum wells and quantum dots," *Frontiers of Optoelectronics*,

vol. 5, no. 1, pp. 112–116, 2012, ISSN: 1674-4594. DOI: 10.1007/s12200-012-0193-x.

[30] M. K. Hudait, M. Clavel, P. Goley, N. Jain, and Y. Zhu, "Heterogeneous integration of epitaxial Ge on Si using AlAs/GaAs buffer architecture: suitability for low-power fin field-effect transistors," *Sci Rep*, vol. 4, p. 6964, 2014, 2045-2322 Hudait, Mantu K Clavel, Michael Goley, Patrick Jain, Nikhil Zhu, Yan Journal Article Research Support, Non-U.S. Gov't Research Support, U.S. Gov't, Non-P.H.S. England 2014/11/08 Sci Rep. 2014 Nov 7;4:6964. doi: 10.1038/srep06964., ISSN: 2045-2322. DOI: 10.1038/srep06964.

[31] Y. Bai, K. E. Lee, C. Cheng, M. L. Lee, and E. A. Fitzgerald, "Growth of highly tensile-strained Ge on relaxed $In_xGa_{1-x}As$ by metal-organic chemical vapor deposition," *Journal of Applied Physics*, vol. 104, no. 8, 2008, ISSN: 0021-8979. DOI: 10.1063/1.3005886.

[32] M. Clavel, D. Saladukha, P. S. Goley, T. J. Ochalski, F. Murphy-Armando, R. J. Bodnar, and M. K. Hudait, "Heterogeneously-Grown Tunable Tensile Strained Germanium on Silicon for Photonic Devices," *ACS Applied Materials & Interfaces*, vol. 7, no. 48, pp. 26 470–26 481, 2015, ISSN: 1944-8244. DOI: 10.1021/acsami.5b07385.

[33] R. Fischer, D. Neuman, H. Zabel, H. Morkoç, C. Choi, and N. Otsuka, "Dislocation reduction in epitaxial GaAs on Si(100)," *Applied Physics Letters*, vol. 48, no. 18, pp. 1223–1225, 1986, ISSN: 0003-6951. DOI: 10.1063/1.96988.

[34] M. K. Hudait, G. Dewey, S. Datta, J. M. Fastenau, J. Kavalieros, W. K. Liu, D. Lubyshev, R. Pillarisetty, W. Rachmady, M. Radosavljevic, T. Rakshit, and

R. Chau, "Heterogeneous integration of Enhancement Mode $In_{0.7}Ga_{0.3}As$ Quantum Well Transistor on Silicon Substrate using thin (<2 μm) Composite Buffer Architecture for High-Speed and Low-Voltage (0.5 V) Logic Applications," in *2007 IEEE International Electron Devices Meeting*, pp. 625–628, ISBN: 2156-017X. DOI: 10.1109/IEDM.2007.4419017.

[35] M. K. Hudait, F. Murphy-Armando, D. Saladukha, M. B. Clavel, P. S. Goley, D. Maurya, S. Bhattacharya, and T. J. Ochalski, "Design, Theoretical, and Experimental Investigation of Tensile-Strained Germanium Quantum-Well Laser Structure," *ACS Applied Electronic Materials*, vol. 3, no. 10, pp. 4535–4547, 2021. DOI: 10.1021/acsaelm.1c00660.

[36] J. Tersoff, "Dislocations and strain relief in compositionally graded layers," *Applied Physics Letters*, vol. 62, no. 7, pp. 693–695, 1993, ISSN: 0003-6951. DOI: 10.1063/1.108842.

[37] S.-G. Ihn, S.-J. Jo, and J.-I. Song, "Effects of postgrowth rapid thermal annealing on InAlAs/InGaAs metamorphic high-electron-mobility transistor grown on a compositionally graded InAlAs/InGaAlAs buffer," *Applied Physics Letters*, vol. 87, no. 4, 2005, ISSN: 0003-6951. DOI: 10.1063/1.1988983.

[38] S. Bhattacharya, S. W. Johnston, S. Datta, and M. K. Hudait, "Interplay Between Strain and Thickness on the Effective Carrier Lifetime of Buffer-Mediated Epitaxial Germanium Probed by the Photoconductance Decay Technique," *ACS Applied Electronic Materials*, vol. 5, no. 6, pp. 3190–3197, May 2023, ISSN: 2637-6113. DOI: 10.1021/acsaelm.3c00256.

[39] J.-M. Chauveau, Y. Androussi, A. Lefebvre, J. D. Persio, and Y. Cordier, "Indium Content Measurements in Metamorphic High Electron Mobility Transistor Structures by Combination of X-Ray Reciprocal Space Mapping and Transmission Electron Microscopy," *Journal of Applied Physics*, vol. 93, no. 7, pp. 4219–4225, 2003. DOI: 10.1063/1.1544074.

[40] M. K. Hudait, Y. Lin, and S. A. Ringel, "Strain relaxation properties of $InAs_yP_{1-y}$ metamorphic materials grown on InP substrates," *Journal of Applied Physics*, vol. 105, no. 6, 2009, ISSN: 0021-8979. DOI: 10.1063/1.3098232.

[41] K. L. Kavanagh, M. A. Capano, L. W. Hobbs, J. C. Barbour, P. M. J. Marée, W. Schaff, J. W. Mayer, D. Pettit, J. M. Woodall, J. A. Stroscio, and R. M. Feenstra, "Asymmetries in dislocation densities, surface morphology, and strain of GaInAs/GaAs single heterolayers," *Journal of Applied Physics*, vol. 64, no. 10, pp. 4843–4852, Nov. 1988, ISSN: 0021-8979. DOI: 10.1063/1.341232.

[42] R. S. Goldman, K. L. Kavanagh, H. H. Wieder, S. N. Ehrlich, and R. M. Feenstra, "Effects of GaAs substrate misorientation on strain relaxation in $In_xGa_{1-x}As$ films and multilayers," *Journal of Applied Physics*, vol. 83, no. 10, pp. 5137–5149, 1998, ISSN: 0021-8979. DOI: 10.1063/1.367331.

[43] M. B. Clavel, F. Murphy-Armando, Y. Xie, K. T. Henry, M. Kuhn, R. J. Bodnar, G. A. Khodaparast, D. Smirnov, J. J. Heremans, and M. K. Hudait, "Multivalley Electron Conduction at the Indirect-Direct Crossover Point in Highly Tensile-Strained Germanium," *Physical Review Applied*, vol. 18, no. 6, p. 064 083, 2022, PRAPPLIED. DOI: 10.1103/PhysRevApplied.18.064083.

[44] N. Pavarelli, T. J. Ochalski, F. Murphy-Armando, Y. Huo, M. Schmidt, G. Huyet, and J. S. Harris, "Optical Emission of a Strained Direct-Band-Gap Ge Quantum Well Embedded Inside InGaAs Alloy Layers," *Physical Review Letters*, vol. 110, no. 17, p. 177 404, 2013, PRL. DOI: 10.1103/PhysRevLett.110.177404.

[45] Z. Sui and I. P. Herman, "Effect of strain on phonons in Si, Ge, and Si/Ge heterostructures," *Physical Review B*, vol. 48, no. 24, pp. 17 938–17 953, 1993, PRB. DOI: 10.1103/PhysRevB.48.17938.

[46] E. Anastassakis, "Phonons, Strains, and Pressure," *High Pressure in Semiconductor Physics II*, p. 117, 1998, ISSN: 0080864538.

[47] Y.-Y. Fang, J. Tolle, R. Roucka, A. V. G. Chizmeshya, J. Kouvetakis, V. R. D'Costa, and J. Menéndez, "Perfectly tetragonal, tensile-strained Ge on $Ge_{1-y}Sn_y$ buffered Si(100)," *Applied Physics Letters*, vol. 90, no. 6, 2007, ISSN: 0003-6951. DOI: 10.1063/1.2472273.

[48] Y. Hoshina, A. Yamada, and M. Konagai, "Growth and Characterization of Highly Tensile-Strained Ge on $In_xGa_{1-x}As$ Virtual Substrate by Solid Source Molecular Beam Epitaxy," *Japanese Journal of Applied Physics*, vol. 48, no. 11R, p. 111 102, 2009, ISSN: 1347-4065 0021-4922. DOI: 10.1143/JJAP.48.111102.

[49] R. People and J. C. Bean, "Calculation of critical layer thickness versus lattice mismatch for Ge_xSi_{1-x}/Si strained-layer heterostructures," *Applied Physics Letters*, vol. 47, no. 3, pp. 322–324, 1985, ISSN: 0003-6951. DOI: 10.1063/1.96206.

[50] A. M. Andrews, J. S. Speck, A. E. Romanov, M. Bobeth, and W. Pompe, "Modeling Cross-Hatch Surface Morphology in Growing Mismatched Layers,"

Journal of Applied Physics, vol. 91, no. 4, pp. 1933–1943, 2002, ISSN: 0021-8979. DOI: 10.1063/1.1428091.

[51] E. A. Fitzgerald, S. B. Samavedam, Y. H. Xie, and L. M. Giovane, "Influence of strain on semiconductor thin film epitaxy," *Journal of Vacuum Science & Technology A*, vol. 15, no. 3, pp. 1048–1056, 1997, ISSN: 0734-2101. DOI: 10.1116/1.580428.

[52] B. Shin, A. Lin, K. Lappo, R. S. Goldman, M. C. Hanna, S. Francoeur, A. G. Norman, and A. Mascarenhas, "Initiation and evolution of phase separation in heteroepitaxial InAlAs films," *Applied Physics Letters*, vol. 80, no. 18, pp. 3292–3294, 2002, ISSN: 0003-6951. DOI: 10.1063/1.1476386.

[53] J.-I. Chyi, J.-L. Shieh, J.-W. Pan, and R.-M. Lin, "Material properties of compositional graded $In_xGa_{1-x}As$ and $In_xAl_{1-x}As$ epilayers grown on GaAs substrates," *Journal of Applied Physics*, vol. 79, no. 11, pp. 8367–8370, 1996, ISSN: 0021-8979. DOI: 10.1063/1.362555.

[54] G. J. Shiflet and J. H. Van Der Merwe, "Misfit accommodation by steps in cubic materials," *Journal of Electronic Materials*, vol. 20, no. 7, pp. 785–791, 1991, ISSN: 1543-186X. DOI: 10.1007/BF02665966.

[55] J. A. Olsen, E. L. Hu, S. R. Lee, I. J. Fritz, A. J. Howard, B. E. Hammons, and J. Y. Tsao, "X-ray reciprocal-space mapping of strain relaxation and tilting in linearly graded InAlAs buffers," *Journal of Applied Physics*, vol. 79, no. 7, pp. 3578–3584, 1996, ISSN: 0021-8979. DOI: 10.1063/1.361410.

[56] E. Gaubas, J. Vanhellemont, E. Simoen, I. Romandic, W. Geens, and P. Clauws, "Carrier lifetime dependence on doping, metal implants and excitation density in

Ge and Si," *Physica B: Condensed Matter*, vol. 401-402, pp. 222–225, 2007, ISSN: 0921-4526. DOI: 10.1016/j.physb.2007.08.151.

[57] J. J. Sheng, D. Leonhardt, S. M. Han, S. W. Johnston, J. G. Cederberg, and M. S. Carroll, "Empirical correlation for minority carrier lifetime to defect density profile in germanium on silicon grown by nanoscale interfacial engineering," *Journal of Vacuum Science & Technology B*, vol. 31, no. 5, p. 051 201, 2013. DOI: 10.1116/1.4816488.

[58] M. K. Hudait, S. W. Johnston, M. R. Das, S. Karthikeyan, P. P. Sahu, J. Das, J. Zhao, R. J. Bodnar, and R. Joshi, "Carrier Recombination Dynamics of Surface-Passivated Epitaxial (100)Ge, (110)Ge, and (111)Ge Layers by Atomic Layer Deposited Al_2O_3," *ACS Applied Electronic Materials*, vol. 5, no. 6, pp. 3350–3361, 2023. DOI: 10.1021/acsaelm.3c00383.

[59] S. Deb and B. R. Nag, "Measurement of lifetime of carriers in semiconductors through microwave reflection," *Journal of Applied Physics*, vol. 33, no. 4, pp. 1604–1604, 1962, ISSN: 0021-8979 1089-7550. DOI: 10.1063/1.1728779.

[60] Y. Mada, "A Nondestructive Method for Measuring the Spatial Distribution of Minority Carrier Lifetime in Silicon Wafer," *Japanese Journal of Applied Physics*, vol. 18, no. 11, pp. 2171–2172, 1979, ISSN: 0021-4922. DOI: 10.1143/jjap.18.2171.

[61] M. Kunst and G. Beck, "The study of charge carrier kinetics in semiconductors by microwave conductivity measurements," *Journal of Applied Physics*, vol. 60, no. 10, pp. 3558–3566, 1986. DOI: 10.1063/1.337612.

[62] S. Johnston, K. Zaunbrecher, R. Ahrenkiel, D. Kuciauskas, D. Albin, and W. Metzger, "Simultaneous Measurement of Minority-Carrier Lifetime in

Single-Crystal CdTe Using Three Transient Decay Techniques," *IEEE Journal of Photovoltaics*, vol. 4, no. 5, pp. 1295–1300, 2014, ISSN: 2156-3403. DOI: 10.1109/JPHOTOV.2014.2339491.

[63] K. L. Luke and L.-J. Cheng, "Analysis of the interaction of a laser pulse with a silicon wafer: Determination of bulk lifetime and surface recombination velocity," *Journal of Applied Physics*, vol. 61, no. 6, pp. 2282–2293, 1987, ISSN: 0021-8979. DOI: 10.1063/1.337938.

[64] E. Yablonovitch and T. J. Gmitter, "A contactless minority lifetime probe of heterostructures, surfaces, interfaces and bulk wafers," *Solid-State Electronics*, vol. 35, no. 3, pp. 261–267, 1992, ISSN: 0038-1101. DOI: 10.1016/0038-1101(92)90230-A.

[65] D. S. Sukhdeo, S. Gupta, K. C. Saraswat, B. Dutt, and D. Nam, "Impact of minority carrier lifetime on the performance of strained Germanium light sources," *Optics Communications*, vol. 364, pp. 233–237, 2016, (Raj), ISSN: 0030-4018. DOI: 10.1016/j.optcom.2015.11.060.

Chapter 4:

Heavy Boron Doping Effects on Biaxially Tensile Strained Germanium (> 1.5%) investigated via Structural Characterization, Effective Lifetime Assessment and Atomistic Modeling

This chapter has been reproduced from a manuscript under preparation titled ***Heavy Boron Doping Effects on Biaxially Tensile Strained Germanium (>1.5%) investigated via Structural Characterization, Effective Lifetime Assessment and Atomistic Modeling, authored by Shuvodip Bhattacharya, Steven W. Johnston and Mantu K. Hudait.***

Highly tensile strained germanium (ε-Ge) represents an essential material system for emerging electronic and photonics applications. Moreover, adjusting the doping levels to moderate or high concentrations can effectively tailor the properties of ε-Ge for specific applications. This article combines

experimental characterization with a theoretical framework to examine the effects of heavy elemental boron (B) doping on pseudomorphic sub-50 nm ε-Ge. High resolution x-ray diffractometry is used to validate tensile strain levels of 1.53% and 1.68% in Ge epilayers, surpassing the indirect-to-direct band gap crossover point at ≃1.5% tensile strain. High-resolution transmission electron microscopy revealed visual evidence of stacking faults and surface roughening in 1.68% ε-Ge, although a coherent and abrupt Ge/III-V heterointerface is observed, devoid of interfacial misfit dislocations. Effective lifetime measurements demonstrated approximately twofold enhancement in the 1.53% B-doped ε-Ge ($N_B \approx 7 \times 10^{19}\ cm^{-3}$) compared to its *unstrained* B-doped counterpart, while no such improvement was observed in 1.68% B-doped ε-Ge. This lack of enhancement is attributed to the presence of stacking faults and surface roughness within the ε-Ge epilayer. Through density functional theory calculations, we independently demonstrate that substitutional B atoms induce local deformation of Ge-Ge bonds in both unstrained and ε-Ge epilayers, resulting in an additive tensile strain. This phenomenon leads to a reduction in the critical layer thickness for the system, facilitating the nucleation and subsequent glide of 90° leading Shockley partial dislocations, which ultimately create stacking faults. In essence, these findings establish an upper limit on the B-doping concentration that can be achieved in highly ε-Ge epilayers. Collectively, these results offer valuable insights into the significance of heavy doping in Ge-based heterostructures, and as such, serve as a cautionary guide for the integration of heavy doping in highly ε-Ge materials for electronic and

photonic applications.

4.1 Introduction

The scope of application of heavily doped $Si_{1-x}Ge_x$, Ge, and $Ge_{1-y}Sn_y$ thin films is immense, and it should come as no surprise that these material systems have garnered special attention over the past decade. In addition to their significance in advancing complementary metal-oxide-semiconductor (CMOS) technologies [1, 2], this group-IV material system forms part of a collective endeavor by researchers to enable monolithic integration of optical and photonic devices together with CMOS integrated circuits [3–5]. Furthermore, recent research has shown enormous potential of these material systems for application in spintronics [6], quantum information processing [7, 8], particle detection [9], optical sensing [10] and single-hole/single-electron transistors [11]. Particularly, holes in Ge exhibit strong inherent spin-orbit coupling, which can find application in hybrid semiconductor-superconductor hybrid systems. Moreover, Ge exhibits a pseudo-direct bandgap which can be engineered to become a direct band-gap material by virtue of uniaxial/biaxial tensile strain [12–14], heavy n-type doping, Sn alloying [15] and special nanostructures such as nanomembranes [16] and micro-disks [17, 18]. Such versatility opens up new frontiers in realizing Ge based optical sources to alleviate the performance limits of copper-based interconnect systems [19–21]. In all of the abovementioned applications, lattice engineering to induce strain and/or moderate to heavy doping concentrations are common factors to tailor the material system to specific applications. Previous investigations have focused primarily on (i) achieving heavily doped $Si_{1-x}Ge_x$ [22] and Ge [23, 24] epitaxial layers with high dopant activation levels [25], (ii) solid solubility limit of dopants in Ge [23], (iii) magnetotransport properties of bulk/bulk-like Ge materials [26, 27] and (iv) structural implications of heavy B-doping concentration in

unstrained Ge [28, 29]. However, not much work has been devoted toward understanding the implications of high concentrations of B-doping on ε-Ge beyond the crossover point, crucial for realizing the potential of such a material system in emerging technologies.

In this work, we employ a combination of structural characterization and effective lifetime measurements, independently corroborated using atomistic modeling, to investigate the impact of substantial B-doping on Ge epilayers, which are tensile strained above the indirect-to-direct crossover point [30]. Pseudomorphic unstrained Ge and tensile strained Ge (ε-Ge) were grown using solid-source molecular beam epitaxy (MBE) in isolated chambers. *In-situ* B-doping was used to achieve a high concentration of B incorporation ($N_B \approx 7 \times 10^{19}$ cm^{-3} *obtained from Hall measurements*) in the ε-Ge epilayers. High resolution x-ray analysis was employed to confirm strain levels of 1.53% and 1.68%. Using cross sectional transmission electron microscopy (HR-XTEM), we show that heavy B-doping in highly ε-Ge favors formation of Shockley partial dislocations (SPDs) and surface roughness. Quantifiable corroboration with structural analysis is provided by way of microwave reflectance photoconductance decay (μ-PCD) effective minority carrier lifetime (τ_{eff}) measurements, where B-doped 1.53% ε-Ge showed $\simeq 2\times$ enhancement in τ_{eff} compared to its B-doped *unstrained* counterpart. No such improvement in τ_{eff}, however, was observed in B-doped 1.68% ε-Ge, which is attributed to the presence of stacking faults and surface roughness. These findings indicate an interplay of dynamics between tensile strain-induced (heavy doping-induced) lifetime enhancement (degradation), *wherein* enhancement in τ_{eff} is observed when the former dominates. Furthermore, atomistic modeling of B-doped bulk Ge and ε-Ge revealed that substitutional B-atoms induce strong deformation of Ge-Ge bonds, which result in an

additive tensile strain at this doping concentration. The consequence is an inherent lowering of the critical layer thickness, h_c, for the system. When the h_c is exceeded, the cumulative tensile strain from the III-V strain template *and* substitutional B atoms paves the way for nucleation and glide of 90° leading Shockley partial dislocations (SPDs) and formation of stacking faults. Thus, we speculate on the existence of a doping dependent critical tensile strain, ε_{doping}, beyond which surface roughening and nucleation of dislocations will compete, and might even become unavoidable, during epitaxial growth. For this work, the results suggest ε_{doping} exists between 1.53% and 1.68% tensile strain levels in ε-Ge for a B-doping concentration of $N_B \approx 7 \times 10^{19}\ cm^{-3}$.

4.2 Experimental Section

4.2.1 Materials Synthesis

In-situ heavily B-doped *unstrained* Ge and ε-Ge heterostructures studied in this work were grown on epi-ready, semi-insulating GaAs (001) substrates with typical 2° $\langle 110 \rangle$ offcut, in an isolated group III-V and group IV dual-chamber solid-source MBE system. The chambers are interconnected *via* an ultra-high vacuum transfer chamber to prevent unwanted oxidation during transfer. The isolation is intended to mitigate atomic interdiffusion at group IV/group III-V heterointerfaces during epitaxial growth of group IV material at elevated temperatures. Growth temperatures at each stage were monitored using thermocouple and controlled using remotely calibrated Eurotherm 2404/8 PID controllers. Surface oxide desorption from GaAs substrates was performed at $\simeq$750°C with an As_2 overpressure of 10^{-5} Torr inside the III-V chamber to prevent surface reconstruction due to As desorption. A reflection high-energy electron diffraction (RHEED) module housed inside the III-V chamber was used for in-situ monitoring of growth rate and temporal surface morphology variations at each growth stage. Oxide desorption step was concluded when clear (2×4) pattern was visible for each growth run. After oxide desorption, the substrates were cooled down to 650°C for 250 nm of GaAs overgrowth. For the control heterostructure C, post GaAs overgrowth, 170 nm of AlAs was grown at 650°C, following which the sample was transferred to the group IV chamber. For heterostructures A and B, after oxide desorption, $In_xGa_{1-x}As$ linearly graded metamorphic buffers (LGBs) were grown at 525°C and 560°C, respectively, where $\boldsymbol{x}$ (*InAs molar fraction*) was linearly varied by adjusting the cell temperature (or in other

words, the In and Ga flux ratio) to achieve the desired InAs compositions for the respective buffers. A much thinner LGB was made possible in heterostructure A compared to heterostructure B by the overshoot layer, which promotes enhanced relaxation of the buffer, thereby providing a coherent growth front for the subsequent constant composition virtual substrate (VS) growth. Afterwards, constant composition $In_xGa_{1-x}As$ VSs were grown at 525°C and 560°C, respectively, for heterostructures A and B, at nominal growth rates of 0.6568 μm/hr and 0.6951 μm/hr. Finally, both samples were transferred to the group IV chamber under high vacuum. For heterostructure C, 270 nm epitaxial Ge, and for heterostructures A and B, ~30 nm epitaxial Ge was grown, at a temperature of 400°C at a nominal growth rate of 0.067 Å/sec. The thickness for ε-Ge is limited by h_c in accordance with the strain energy balance model proposed by People and Bean [31]. To achieve the same doping concentration in all heterostructures, the B-dopant cell was maintained at 1650°C during epitaxial Ge growth to achieve a B-doping concentration of 7×10^{19} cm^{-3} (*validated ex-situ using Hall measurements on van der Pauw structures*). After epitaxial Ge growth, all heterostructures were cooled down to 50°C at a temperature ramp down rate of 5°C/min to prevent thermal cracking or wafer bowing that could arise from the varying thermal coefficients of the materials used in the heterostructure stack. The heterostructures studied in this work are depicted in Figure 4.1.

4.2.2 Materials Characterization

To investigate the strain state of the Ge epilayers and InAs molar fraction in the $In_xGa_{1-x}As$ VSs, *ex-situ* high-resolution x-ray diffraction (HR-XRD) was used. High

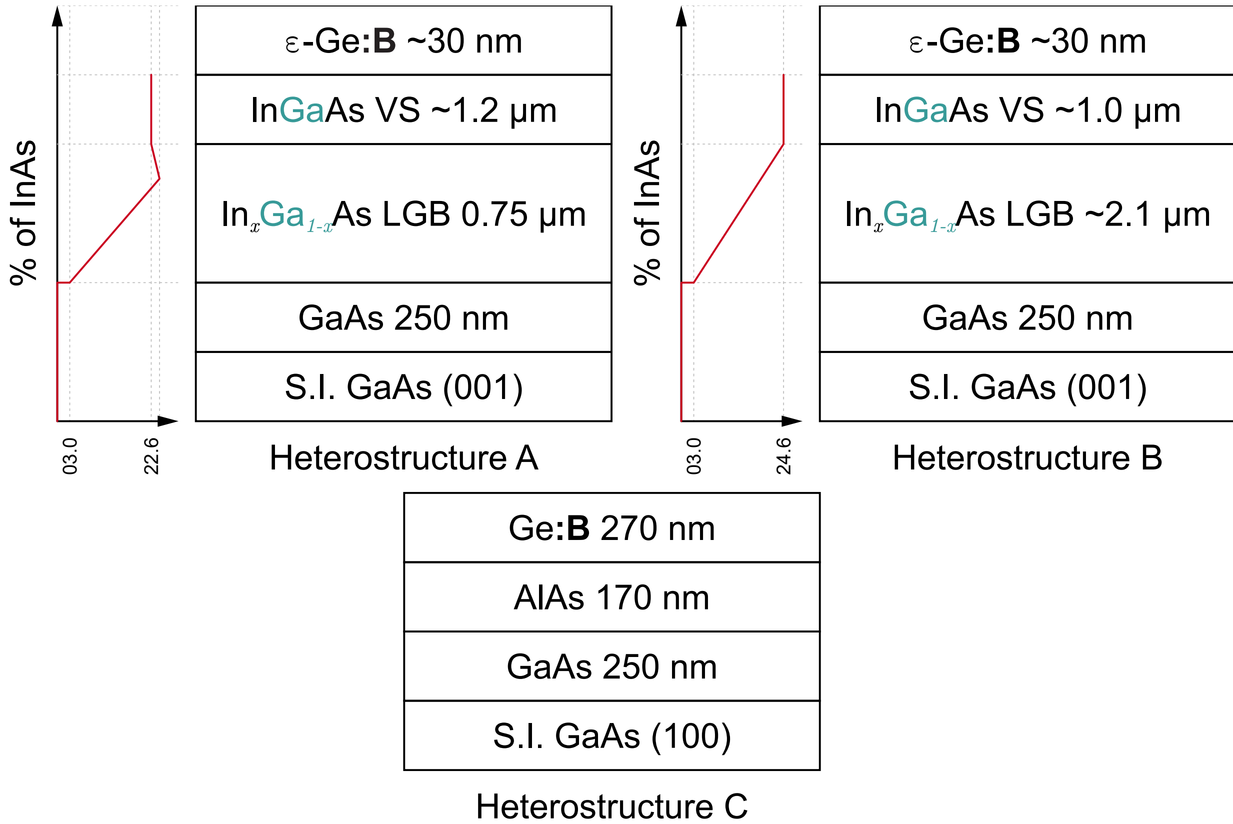

Figure 4.1: Schematic representation of the heterostructures analyzed in this study. Heterostructure C serves as the *unstrained* control sample with 270 nm epitaxial Ge on vicinal 2°⟨110⟩ (001)GaAs substrates, with AlAs as an intermediate buffer. For heterostructures A and B, respectively, 30 nm of 1.53% and 1.68% biaxially tensile strained epitaxial Ge was grown on InGaAs virtual substrates. The boron doping concentration ($N_A \approx N_B$, where N_A denotes the acceptor concentration) for all heterostructures was confirmed *via* Hall measurements of van der Pauw structures to be $N_B \approx 7 \times 10^{19}\ cm^{-3}$.

resolution symmetric (004) and asymmetric (115) reciprocal space maps (RSMs) were recorded on a PANalytical X'Pert Pro diffractometer, which is equipped with a monochromatic Cu Kα_1 (λ=1.540597 Å) x-ray source. All RSMs were recorded with the PIXcel 3D detector, with the goniometer resolution set to 0.0001° and step size set to 0.0049° for both 2θ and ω axes during measurement. To evaluate the structural implications of heavy B-doping on ε-Ge epilayers and ε-Ge/In$_x$Ga$_{1-x}$As heterointerfaces, bright field cross sectional transmission electron micrographs (XTEM) were recorded on a JEOL 2100 system with a formatted operating voltage of 200kV ($\lambda_{electron} \simeq$ 2.5079 pm). Electron transparent thin foils required for TEM characterization were prepared using conventional mechanical milling process, which was followed by Ar^+ ion milling at low temperatures to achieve the desired lamella. To measure the effective minority carrier lifetime (τ_{eff}) of each B-doped sample, conventional microwave-reflectance photoconductance decay (μ-PCD) measurements were performed at the National Renewable Energy Laboratory (NREL). All measurements were done at room temperature on representative 1 cm $\times$ 1 cm cleaved sample pieces. The samples were placed underneath a rectangular waveguide (WR42, 20 GHz, 0.43 cm $\times$ 1.07 cm) and optically pumped using a Q-switched neodymium-doped YAG laser with a power rating of 20 mW. The waveguide is used to guide the 20 GHz microwave probe source reflected from the samples that is recorded by an oscilloscope to map the conductance decay. The wavelength was maintained at 1500 nm for all measurements to ensure complete excitation of the Ge epilayers. The decay curves, thus recorded, were fitted with an exponential decay regression as explained in the later part of the text.

Atomistic density functional theory calculations were performed to study the

deformation of Ge-Ge bonds in relaxed, *undoped* and B-doped ⟨110⟩ biaxially 1.5% ε-Ge. These calculations were made possible using the Synopsys QuantumATK software suite [32]. The standard unpolarized generalized gradient approximation (GGA) [33] with PerdewBurkeErnzerhof (PBE) exchange and correlation functionals was used for these calculations. Norm-conserving SG15 [34] pseudopotentials were used as the basis set for each element, with HighProjectorShift applied for Ge for reasons explained elsewhere [32]. *Undoped* and **B**-doped bulk and tensile-strained Ge supercells were geometrically optimized using a kinetic energy cutoff of 85 Hartree and a $6 \times 6 \times 8$ Monkhorst-Pack k-point grid leading to 148 k-points to map the irreducible Brillouin zone, in conjunction with a force tolerance of 0.05 eV·Å^{-1}, stress error tolerance of 0.1 GPa and maximum atomic displacement size of 0.2 Å.

4.3 Results and Discussion

4.3.1 ε-Ge Strain State and Buffer InAs Composition Analysis using HR-XRD

The structural analyses of the heterostructures illustrated in Figure 4.1 were conducted using double-axis HR-XRD. A typical combination of symmetric (004) and asymmetric (115) reciprocal space maps (RSMs) were recorded from each heterostructure to determine the InAs molar fraction in the InGaAs VS and the level of imparted mechanical strain to the active Ge epilayer, following methodologies outlined elsewhere [35]. In a typical symmetric (004) RSM along the (001) growth direction, the relative positions of the reciprocal lattice contour centroids (RLCCs) in relation to the substrate RLCC provide insights into the out-of-plane lattice parameters, $a_\perp$, of the corresponding epilayers. The RLCCs from individual epilayers in a symmetric scan should exhibit vertical alignment with the substrate along the Q_x axis, barring any influence from tilt or finite crystal effects [36]. However, in mismatched heteroepitaxy, strain relaxation often leads to tetragonal distortion of the lattice, resulting in potential epilayer tilt in arbitrary directions, influenced by the number and efficiency of slip systems active during the relaxation process. This non-uniform relaxation, typically linked to differences in preferential nucleation and glide velocities of α and β dislocations with group-V- and group-III-terminated cores, respectively, manifests as a horizontal shift of the RLCCs of the epilayers relative to that of the substrate in both symmetric and asymmetric scans [37]. Figure 4.2(a)-(b) display the symmetric (004) RSMs for heterostructures A and B, respectively, where the angular $(2\theta - \omega)$ coordinates have been converted to reciprocal

space coordinates (reciprocal lattice unit, *r.l.u.*). The RLCCs of the constant composition InGaAs VSs are positioned below that of the GaAs substrate, in accordance with expansion (contraction) of out-of-plane lattice constant, $a_{\perp}$ (in-plane lattice constant, $a_{\parallel}$). Along the same lines, the RLCCs from ε-Ge epilayers are seen to be shifted above that of GaAs substrates, indicative of expansion (contraction) of $a_{\parallel}$ ($a_{\perp}$), with the magnitude of displacement indicating the strain imparted to the Ge epilayers. The magnitude of the vertical displacement of the InGaAs VSs RLCCs correlates with the InAs molar fraction present in the InGaAs VSs. A similar argument holds for the Ge RLCCs; a larger vertical displacement relative to the GaAs substrate RLCC suggests a higher tensile strain, and vice versa. Notably, while the InGaAs VS RLCC for heterostructure B is vertically displaced further than in heterostructure A indicating a higher InAs molar fraction and consequently a higher tensile strain – it is observed that the Ge epilayer RLCCs in both heterostructures exhibit similar displacement magnitudes relative to the GaAs substrate RLCC. This could imply that the Ge epilayers in both heterostructures exhibit comparable tensile strain. This observation could arise from several possibilities: (i) insufficient relaxation of the buffer, (ii) partial relaxation of the Ge epilayer, or (iii) epilayer tilt resulting from tetragonal distortion which obscures the actual RLCC position. Further understanding of this observation can be gained from the asymmetric (115) scan. It should also be noted that the symmetric and well-defined contours of the InGaAs VSs suggest that defects nucleating from mismatched heteroepitaxy were effectively confined within the linearly graded metamorphic buffers. Consequently, reduced propagation of threading dislocations (TDs) to both the InGaAs VSs and the active Ge epilayers can be expected.

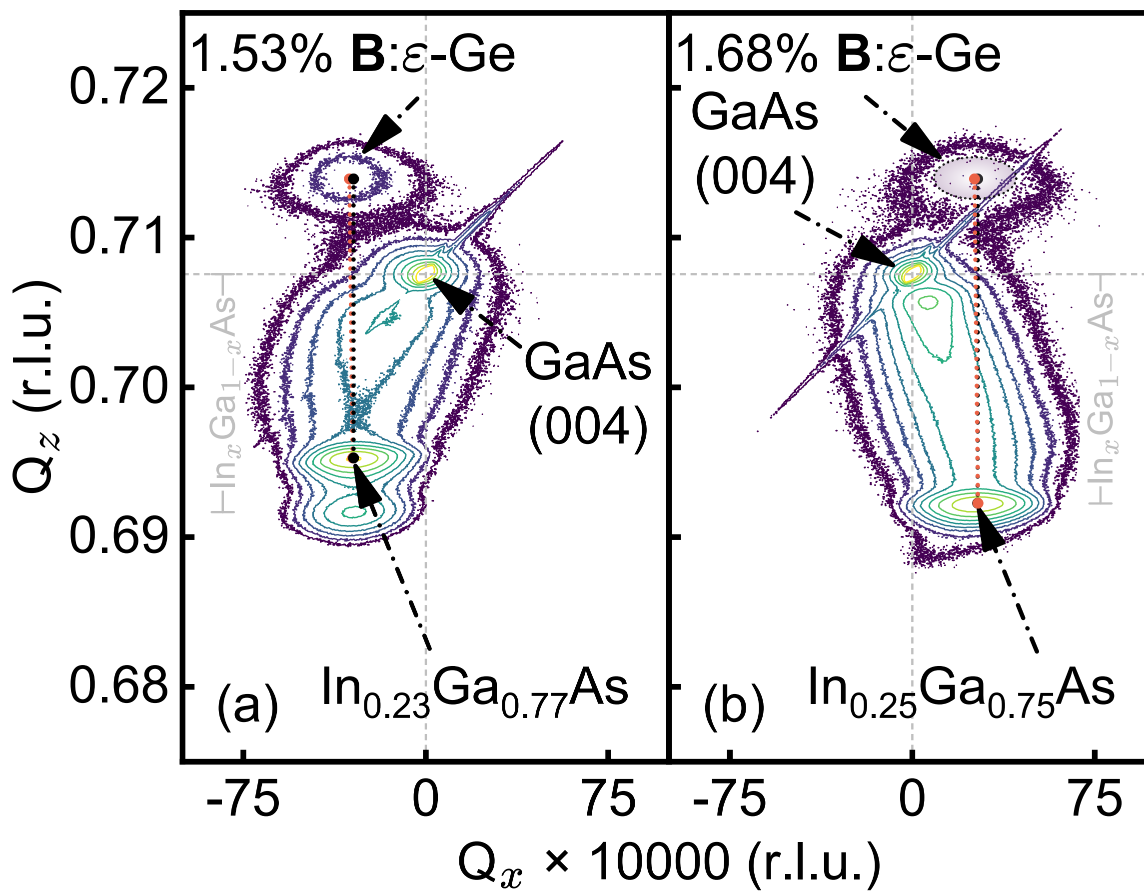
1.53% B:ε-Ge
1.68% B:ε-Ge
GaAs (004)
GaAs (004)
In0.23Ga0.77As
In0.25Ga0.75As
InxGa1−xAs
InxGa1−xAs
(a)
(b)
0.72
0.71
0.70
0.69
0.68
Qz (r.l.u.)
-75
0
75
-75
0
75
Qx × 10000 (r.l.u.)

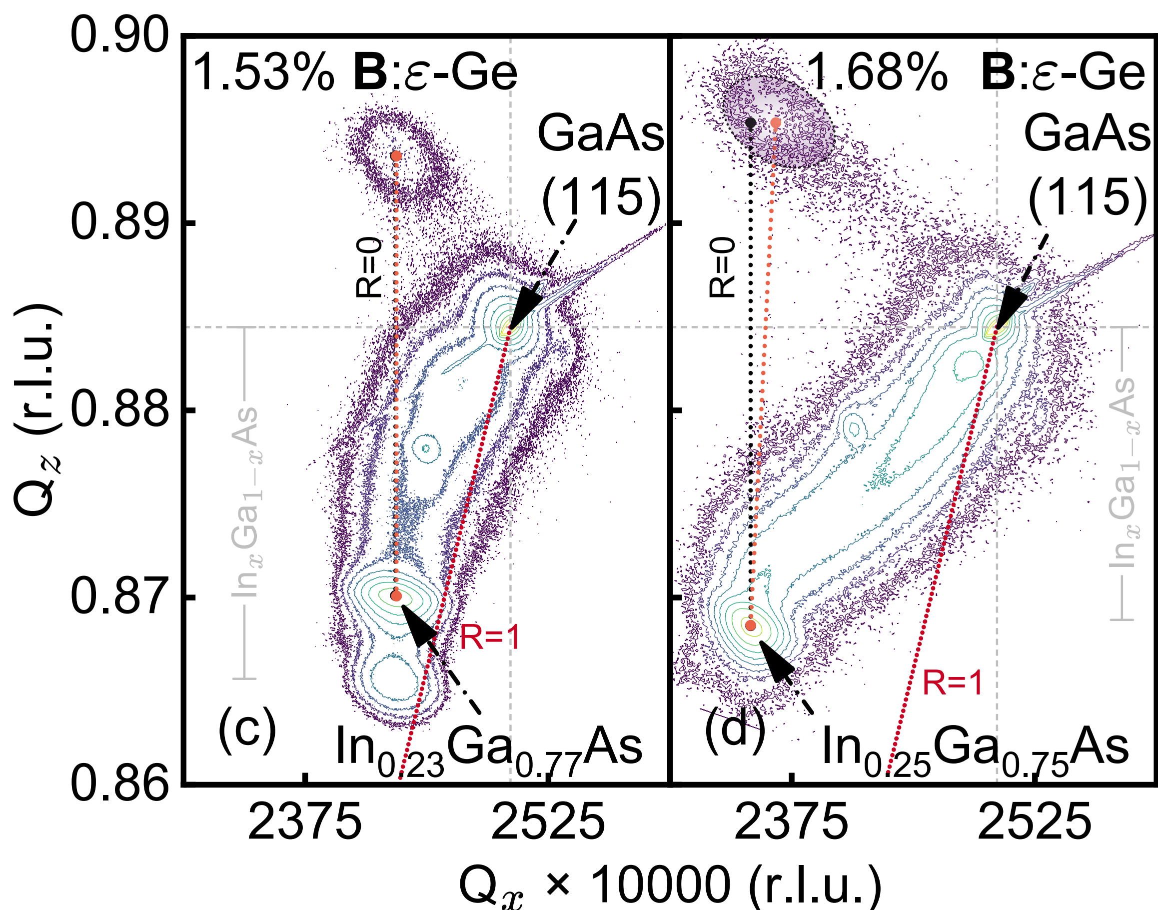

Figure 4.2: (a)-(b) Symmetric (004) RSMs recorded from heterostructures A and B, respectively. The dotted orange lines connect the RLCC of the InGaAs VS and the ε-Ge epilayer used for characterization. The dotted black lines are provided to indicate the expected position of the Ge epilayer RLCC in the absence of tilt. (c)-(d) Asymmetric (115) RSM scans recorded from heterostructures A and B, respectively, with the dotted black and orange lines having the same significance as described previously. The dotted red line (R=1) signifies the trajectory along which the InGaAs VS RLCCs would be positioned if they were fully relaxed.

As previously noted, crystallographic epilayer tilting relative to the substrate and between epilayers is often observed in mismatched heteroepitaxy. In Figure 4.2, the reciprocal lattice contours (RLCs) from the respective epilayers exhibit horizontal shift relative to the GaAs substrate RLC due to epilayer tilting. Majority of the observed tilting occurs within the linearly graded metamorphic buffer, suggesting non-uniform relaxation dynamics [37], whereas minimal tilt is observed between the InGaAs VS RLCC and the corresponding Ge epilayer RLCC. Illustrated as visual aids, the dotted orange lines are drawn from the InGaAs VS RLCCs and terminate at the corresponding Ge epilayer RLCCs utilized for tensile strain calculations. In contrast, the dotted black lines originate from the InGaAs VS RLCCs and extend to where the Ge epilayer RLCCs would coincide in the absence of tilt. The minimal angle between these two dotted lines in both heterostructures suggests minimal tilting; this finding further rules out the possibility of partial relaxation in the Ge epilayer in heterostructure B. For heterostructure B specifically, due to the low intensity from the Ge epilayer contour, an ellipsoid is provided as visual aid to indicate the region of interest (ROI) used to locate the Ge RLCC.

To ascertain the out-of-plane lattice parameters, asymmetric (115) RSM scans were recorded from heterostructures A and B, as depicted in Figures 4.2(c)-(d). The low angle of incidence in an asymmetric scan results in additional splitting of the iso-intensity contours in the reciprocal coordinate space. Consistent with symmetric (004) scan findings, the InGaAs VS RLCCs are located below, and the Ge epilayer RLCCs are located above the GaAs substrate RLCCs. Notably, the Ge epilayer RLCC from heterostructure B is observed to be positioned slightly higher than that in heterostructure A. As mentioned earlier, tetragonal distortion during mismatched

heteroepitaxy may give rise to epilayer tilt which can obscure the accurate determination of the lattice parameters. Given the minimal epilayer tilting between the InGaAs VS and Ge epilayer RLCCs of interest, indicative of pseudomorphic growth, adjustments for epilayer tilt have not been pursued for this work. The nominal InAs compositions were determined to be 22.6% and 24.6% for heterostructures A and B, respectively, closely aligning with targets of 22.5% and 24%. We emphasize that the slight deviation between targeted and measured InAs molar fractions may be an artifact of epilayer tilt. The in-plane epitaxial strain, $\varepsilon_{\parallel}$, is defined as:

$$\varepsilon_{\parallel} = \frac{a_{\parallel} - a_r}{a_r} \tag{4.1}$$

where $a_{\parallel}$ and a_r refer to the in-plane lattice parameter and relaxed epilayer lattice parameter, respectively. Utilizing the relaxed lattice constant of Ge, $a_{r,Ge} = 5.658$ Å [38] along with XRD measured in-plane lattice parameters, the strain states of Ge in heterostructure A ($a_{\parallel} = 5.7447$ Å) and heterostructure B ($a_{\parallel} = 5.7530$ Å) were calculated to be 1.53% and 1.68%, respectively. The calculated relaxed lattice parameters for Ge were $a_{r,Ge,Het.\ A} = 5.6583$ Å and $a_{r,Ge,Het.\ B} = 5.6520$ Å, respectively, for heterostructures A and B, which are in close proximity to the literature value. Additionally, any minor discrepancy in the calculated relaxed Ge lattice parameter relative to the literature value for heterostructure B could be attributed to errors in locating the accurate RLCC position, considering the low intensity recorded. It is also important to note that while B-doping-induced tensile strain has been measured using HR-XRD previously [39], decoupling the doping-induced tensile strain from mechanical

strain induced by the metamorphic buffer presents significant challenges at this stage. This limitation arises from the fact that the ε-Ge unit cells are constrained by the underlying III-V strain template, where any alterations in the strain state due to B-induced distortion predominantly affect only the Ge-Ge bonds immediately proximal to the B atom. Consequently, such effect is likely obscured by the buffer-induced strain and exceeds the resolution capabilities of the current experimental setup.

4.3.2 Heterostructure analysis *via* TEM

To provide additional insight into the structural integrity of heavily *in-situ* B-doped ε-Ge heterostructures in this work, cross-sectional low- and high-magnification TEM micrographs were recorded from heterostructure B. Figure 4.3(a) illustrates the low-resolution cross-sectional TEM recorded from heterostructure B, displaying the complete stack. The lattice-mismatch induced defects are observed to be confined within the $In_xGa_{1-x}As$ metamorphic buffer and do not glide into the constant composition InGaAs VS. This observation supports the previously noted symmetric and confined contours of the InGaAs VS in the recorded RSM. The absence of extended defects within the InGaAS VS and further into the active Ge epilayer suggests coherent pseudomorphic growth. Figure 4.3(b) presents a typical representative heterointerface region shared by $In_{0.25}Ga_{0.75}As$ and ε-Ge. Several key observations can be made from this micrograph. The contrast in atomic factors between Ge and InGaAs highlights the abrupt nature of the heterointerface, indicating minimal atomic interdiffusion. Additionally, stacking faults are observed to initiate at the heterointerface (region of interest 1 (ROI-1)), and along the dislocation line, they dissociate into two diverging $\langle 112 \rangle$ directions (ROI-2).

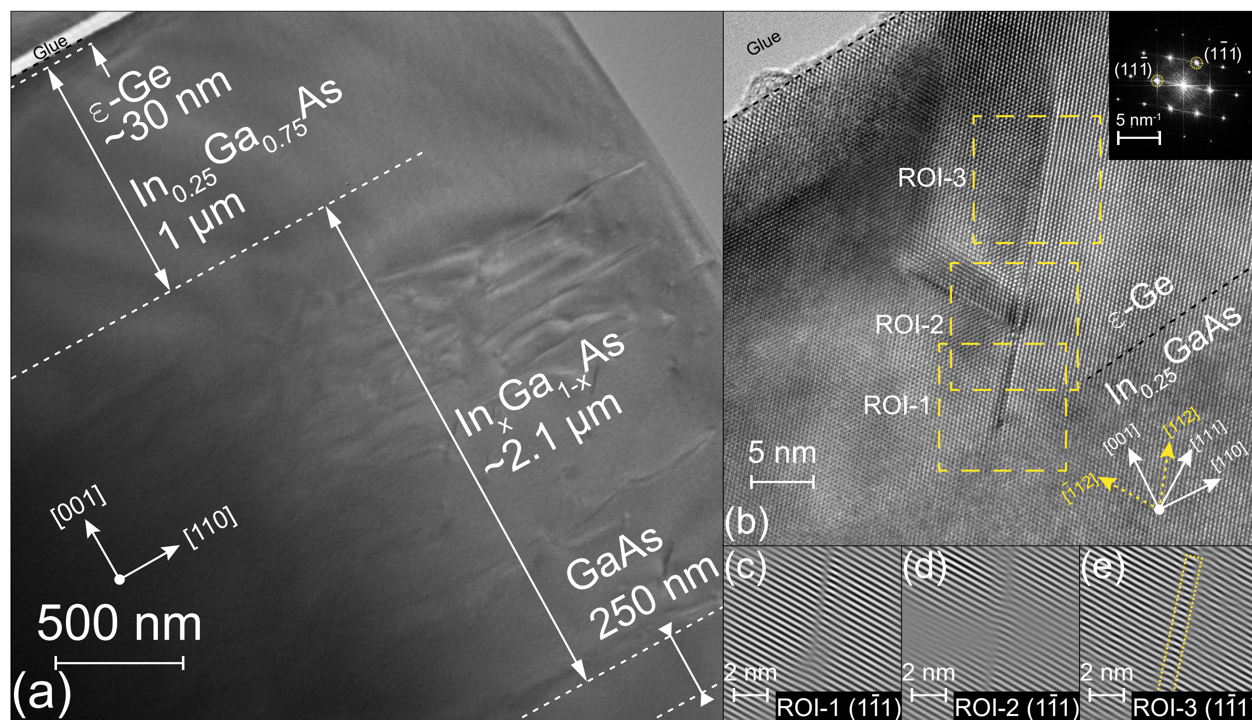

Figure 4.3: (a) Cross-sectional low magnification bright-field TEM recorded heterostructure B showing the full stack. (b) High-resolution cross-sectional bright-field TEM recorded from heterostructure B, showing a representative ε-Ge/In$_{0.25}$Ga$_{0.75}$As heterointerface region. The dotted yellow lines indicate the 10 nm × 10 nm regions of interest (ROIs) analyzed. The inset presents the FFT pattern ($\mathfrak{F}(\omega)$) derived from the entire region. The presence of an abrupt and coherent interface is evident by the difference in atomic factor contrast between Ge and In$_{0.25}$Ga$_{0.75}$As. A stacking fault is identifiable in this figure along the projected $\langle 112 \rangle$ directions. (c)-(e) Inverse FFT patterns $\left(\mathfrak{F}^{-1}\left(\mathfrak{F}(\omega)\right)\right)$ corresponding to ROI-1, ROI-2 and ROI-3, respectively, obtained by selectively masking the $\left(1\bar{1}1\right)$ planes from the FFT pattern displayed in the inset of Figure 4.3(b). The dotted yellow line in Figure 4.3(e) signifies the area of the two-monolayer twin observed in ROI-3.

The inset of Figure 4.3(b) shows the diffraction pattern from the representative region, where diffraction streaks along the $\langle 111 \rangle$ directions suggest the presence of stacking faults. Moreover, the absence of satellite peaks in the diffraction pattern indicates that no multiple distinct lattice parameters exist, further confirming the pseudomorphic nature of the Ge epilayer.

In ROI-3, marked in the micrograph, a 2-monolayer twin region is identified, terminating at a Shockley partial dislocation (SPD) along the $\langle 112 \rangle$ direction. Using noise-filtering inverse Fast Fourier Transform (iFFT) *i.e.*, $(\mathfrak{F}^{-1}(\mathfrak{F}(\omega)))$, selective masking of the $(1\bar{1}1)$ planes from the diffraction pattern was conducted on ROIs 1, 2 and 3 as shown in Figures 4.4(c)-(e), respectively. Each figure reveals a discontinuity of lattice planes on the $(1\bar{1}1)$ planes, with the 2-monolayer twin region highlighted by the yellow rectangular area in Figure 4.3(e). In contrast, no discontinuity was observed on the $(11\bar{1})$ planes (not shown here) indicating that the active slip plane in this case is either $(1\bar{1}1)$ or $(\bar{1}1\bar{1})$.

Figure 4.4(a) illustrates another representative heterointerface region shared between $In_{0.25}Ga_{0.75}As$ and ε-Ge from heterostructure B. Notably, this figure reveals a virtually defect-free heterointerface shared between the metamorphic buffer VS and the active epitaxial Ge, as indicated by the dotted black line in ROI-4. Similar to the observations in Figure 4.3(b), the abrupt nature of the heterointerface is also evident here. In ROI-5, a stacking fault along the $[\bar{1}12]$ direction is observed; however, unlike in Figure 4.3(b), the stacking fault is located further away from the heterointerface. This could suggest the presence of local micro-strain effects favoring nucleation of partial dislocations (PDs) that form stacking faults. Figures 4.4(b)-(c) present the diffraction patterns obtained from ROIs 4 and 5, respectively. In these figures, satellite peaks are absent, reinforcing

the pseudomorphic nature of the growth. Additionally, streaks are observed along the $\langle 111 \rangle$ directions, indicating the presence of the stacking fault. Figures 4.4(d)-(f) depict the iFFT of selectively masked $(11\bar{1})$ and $(1\bar{1}1)$ diffraction points from ROIs 4 and 5, respectively. No discontinuity along the $\{111\}$ planes is observed in ROI-4, which supports the presence of a coherent heterointerface. However, discontinuity in lattice planes is noted along the $(1\bar{1}1)$ planes from ROI-5, coinciding with the location of the identified stacking fault. Marée *et al.* have previously addressed that stacking faults are formed when the typical 60° mixed-type perfect dislocations in zinc-blende structures (with Burgers vector $\frac{a}{2}\langle 110 \rangle$) dissociate into pairs of Shockley Partial Dislocations (SPDs) (with Burgers vector $\frac{a}{6}\langle 112 \rangle$) [40]. Under tensile shear stress, as is the case here, the maximum force is subjected to the 90° SPD which must nucleate first, followed by the trailing 30° SPD responsible for annihilating the stacking fault and restoring the typical ABCABC... stacking pattern along the $\langle 111 \rangle$ directions observed in diamond cubic zinc-blende structures. Figure 4.4(h) displays the noise-filtered iFFT from the stacking fault region, notably showing clear evidence of a perfect 60° dislocation dissociating into a 90° leading SPD and 30° trailing SPD. A Burgers circuit is depicted around each SPD, with the plane of slip indicated by the dotted yellow line, surrounding the entire stacking fault ribbon. As discontinuity is observed on the $(1\bar{1}1)$ or $(\bar{1}1\bar{1})$ planes, projection of the Burgers vector onto the $[\bar{1}10]$ planes can infer the directions of the SPDs. Consequently, the dissociation of the perfect $\frac{a}{2}\langle 110 \rangle$ dislocation is inferred as $\overrightarrow{b_{60°}} \rightarrow \overrightarrow{b_{90°}} + \overrightarrow{b_{30°}} \implies \frac{a}{2}[110] \rightarrow \frac{a}{6}[121] + \frac{a}{6}[21\bar{1}]$, where a denotes the lattice parameter. It is essential to address the presence of stacking faults, in contrast to the lack of visible disorder at the heterointerface in Figures 4.3(b) and 4.4(a). Despite the observations here, we previously demonstrated excellent pseudomorphic *uid*-epitaxial Ge growth with

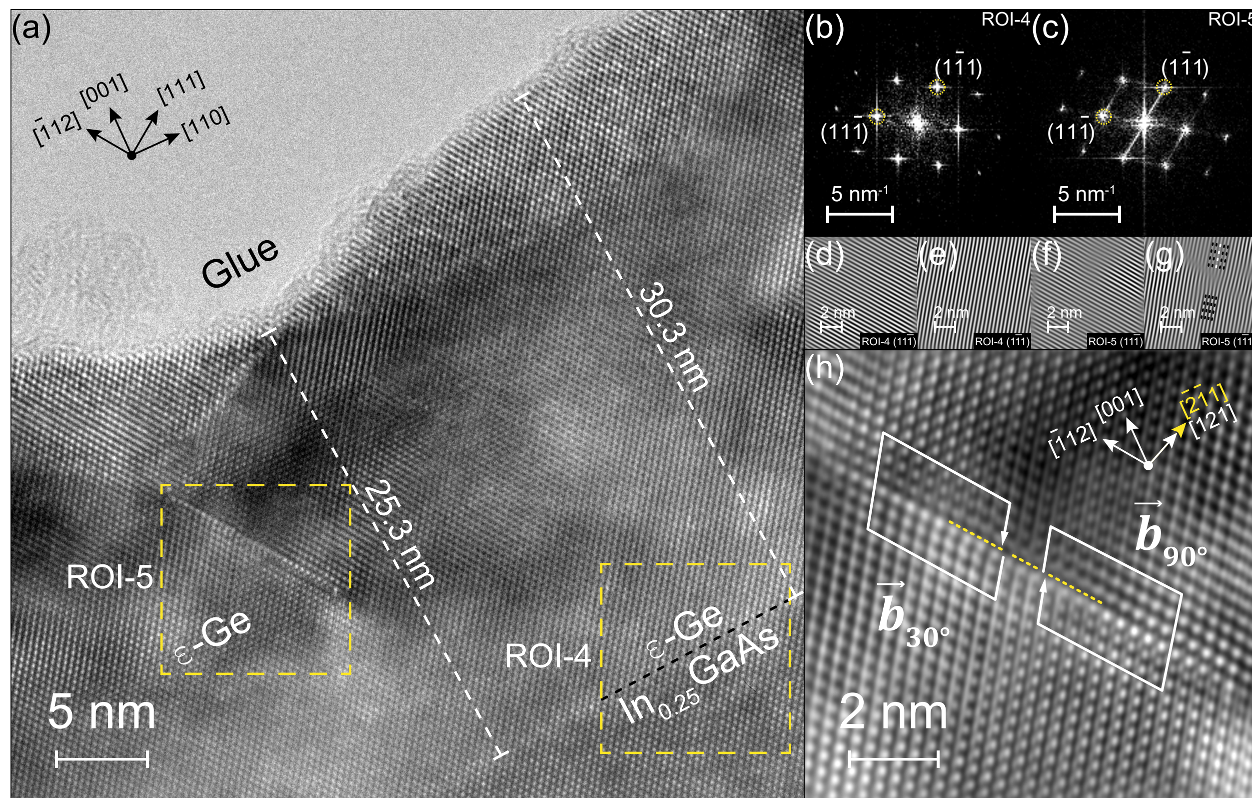

Figure 4.4: (a) High-resolution cross-sectional bright-field TEM micrograph from a representative region of ε-Ge/$In_{0.25}Ga_{0.75}As$ heterointerface recorded from heterostructure B. The dotted yellow lines highlight the 10 nm × 10 nm ROIs analyzed. The variation in thickness, indicative of surface roughness, is represented by the dotted white lines, along with the corresponding measured thickness. (b)-(c) FFT ($\mathfrak{F}(\omega)$) diffraction patterns derived from ROI-4 and ROI-5, respectively. (d)-(e) Inverse FFT patterns $\left(\mathfrak{F}^{-1}\left(\mathfrak{F}(\omega)\right)\right)$ from ROI-4, obtained by selectively masking $\left(11\bar{1}\right)$ and $\left(1\bar{1}1\right)$ diffraction points, respectively, with no lattice plane discontinuities observed. (f)-(g) Inverse FFT patterns from ROI-5, also obtained by selectively masking $\left(11\bar{1}\right)$ and $\left(1\bar{1}1\right)$ diffraction points, respectively, where lattice discontinuity is noted only along the $\left(11\bar{1}\right)$ planes, as indicated by the additional dotted white line. (h) Inverse FFT pattern obtained by mapping all diffraction points from ROI-5, clearly illustrating the stacking fault ribbon, with the 90° leading and 30° trailing PDs highlighted, as explained in the main text. The slip plane $\left(11\bar{1}\right)$ is marked by the dotted yellow line.

up to 1.94% tensile strain on a similar strain template (*albeit with higher InAs content*), where no extended defects or stacking faults were observed, at the heterointerface or within the ε-Ge epilayer [41]. A significant distinction in this study is the deliberate *in-situ* heavy B-doping of the ε-Ge epilayer. While the $In_{0.25}Ga_{0.75}As$ was not doped, the B dopant shutter was opened during the epitaxial Ge growth. Previous studies have shown that during B-doping, the lattice of the host Ge experiences warping in the vicinity of the B-atoms [29]. In a subsequent section, we illustrate this effect through atomistic modeling of the tensile strained system. Nonetheless, it is important to note that while low doping concentrations may or may not favor nucleation of dislocations, increase in local micro-strains within the Ge epilayer occurs due to reduced B-B distance at heavier doping concentrations.

The adverse effects of heavy B-doping on the crystallinity of Si—epitaxially grown or using the seed method—have been documented. For instance, Miller *et al.* studied the introduction of edge dislocations due to substantial contraction of the Si lattice beyond a B-doping concentration of 8×10^{18} cm^{-3} [42]. Schwuttke utilized x-ray topography measurements to illustrate the presence of precipitates along the {111} planes which serve as significant micro-strain centers [43]. Recently, it was reported that the solid solubility of B in Ge is $\sim 5.5 \times 10^{18}$ cm^{-3} at 850°C in single crystal Ge [23]. Additionally, a B concentration as low as 1% facilitated compressive strain compensation in $Si_{1-x}Ge_x$ crystals, enabling a higher Ge content incorporation without an increase in residual strain energy [44].

Furthermore, Figure 4.4(a) presents an intriguing observation that is less apparent in Figure 4.3(b). In contrast to the coherent and abrupt ε-Ge/$In_{0.25}Ga_{0.75}As$

heterointerface, the terminating surface of the Ge epilayer exhibits undulations, suggesting a rough surface, with thickness ranging from 25.3 nm to 30.3 nm in the representative micrograph. Researchers have established that surface roughening by way of island formation serves as an elastic deformation pathway for alleviating misfit-induced strain [45]. This surface roughening competes with dislocation nucleation, with surface roughening scaling as ε^{-4} compared to ε^{-1} for dislocation nucleation, where ε is the lattice misfit. In mismatched heteroepitaxy, the energy barrier to surface roughening is significantly lower for high misfit growths, allowing for partial relaxation of misfit strain by surface roughening. Conversely, a critical misfit, ε_0, exists below which dislocation nucleation is favored over surface roughening, resulting in misfit strain relief through nucleation of new dislocations or glide of preexisting dislocations. This reduction in misfit strain subsequently increases the energy barrier for surface roughening, enabling the growth to proceed with an atomically smooth growth front. We have recently demonstrated island-driven growth (or 3D Stranski-Krastanov mode of growth) in epitaxial Ge grown on $In_{0.53}Ga_{0.47}As$ and $In_{0.51}Al_{0.49}As$, which contain significantly higher InAs compositions than those utilized in this work [46].

In light of the aforementioned discussion, we propose that heavy B-doping, as is the case in this work, may be the primary cause for the nucleation of SPDs, consequently leading to stacking faults and/or surface roughening. One qualitative hypothesis could be the following. When growth of Ge begins from the abrupt $Ge/In_{0.25}Ga_{0.75}As$ heterointerface, the **B** adatoms occupy certain host Ge lattice sites, inducing significant warping of the Ge-Ge covalent bonds proximal to the B atoms. This concomitantly increases the local strain at the growth front. At low to moderate B concentrations (*i.e.* $10^{14} - 10^{18}$ cm^{-3}),

only a limited number of Ge-Ge bonds around the B atoms are deformed. However, heavy B doping reduces the B-B distance, potentially leading to long-range residual strain energy. This additional strain energy lowers the critical misfit, ε_0, thereby promoting surface roughening. As some strain energy is relieved elastically by surface roughening, the critical misfit, ε_0, is again elevated, pushing the system into a low misfit regime. Consequently, the strain energy reduction induced by surface roughening at the growth front also diminishes the barrier for nucleation of dislocations, especially PDs in this case. Furthermore, this dynamic modification of the h_c for the system due to the added strain makes it energetically favorable for nucleation and glide of perfect or partial dislocations, thereby providing a qualitative explanation for the observed stacking faults within the ε-Ge epilayer. In a more specific case, the lattice distortion due to B adatoms can induce formation of PDs at the heterointerface itself, which could explain the formation of stacking faults at the heterointerface observed in this work in the absence of misfit dislocations or extended defects from the underlying buffers. In tandem, we emphasize that there exists a certain critical limit of tensile strain for a corresponding doping concentration, ε_{doping}, above which surface roughening and possibly the nucleation of dislocations will be observed. It is to be noted that no B precipitates or B impurity segregation were observed at the resolution limit of the current experimental setup, which have been shown to induce surface roughening [47] and nucleation of dislocations. A direct consequence of extended defects in epitaxial layers is the degradation of minority carrier lifetime, which is the topic of the next sub-section.

4.3.3 Effective Minority Carrier Lifetime using μ-PCD

In the context of semiconductor materials, minority carrier lifetime serves as a critical figure of merit (FOM) for assessing material quality. The presence of defects and other irregularities in the active material can cause severe degradation of minority carrier lifetime by functioning as effective recombination centers [48, 49]. Additionally, surface roughness contributes to this degradation; effectively, surface roughness increases the number of surface states per unit area which can also act as recombination centers.

In this work, we have employed non-contact optical μ-PCD technique to analyze the heterostructures under investigation [50, 51]. A microwave laser pump source is employed to generate photocarriers within the sample. This causes a change in local concentration and enhancement in local conductance. With the optical source removed, the excess photocarriers return to equilibrium conditions through various recombination processes. This process leads to a decrease in non-equilibrium conductance, which can be monitored using a microwave probe source. A considerable portion of the generated photocarriers also recombine at surface states before they can diffuse into the material, indicating that a surface lifetime component is always present within the observed characteristics. Moreover, the pump wavelength can be adjusted to mitigate the effect of the surface states. Longer wavelengths possess greater skin depth, which allows for a high concentration of photocarriers generated further from the surface, effectively within the bulk of the material. Under low injection conditions, we can neglect non-linear recombination dynamics and express the inverse of the principal mode of decay lifetime, τ_{eff}, as a cumulative sum of the inverse bulk lifetime component (τ_{bulk}) and inverse surface lifetime component (τ_S) as [52, 53]:

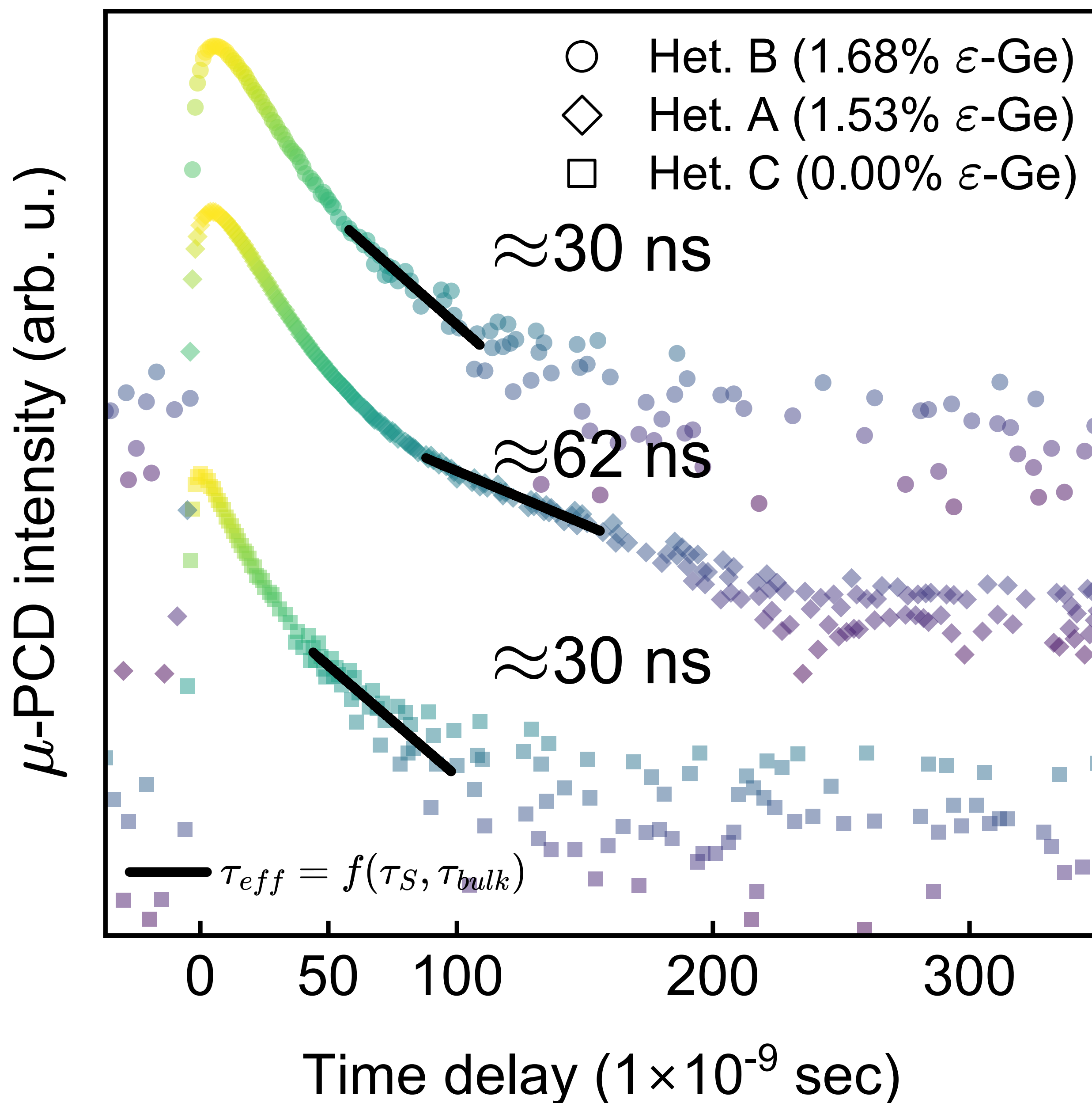

Figure 4.5: Typical μ-PCD transient decay curves recorded from heterostructures A, B and C, as illustrated in Figure 4.1. The effective minority carrier lifetime, τ_{eff}, is indicated for each trace. The traces have been normalized to the peak intensity and vertically shifted for clarity.

$$\frac{1}{\tau_{eff}} = \frac{1}{\tau_{bulk}} + \frac{1}{\tau_S} \tag{4.2}$$

Figure 4.5 presents typical μ-PCD transient decay curves obtained from the heterostructures illustrated in Figure 4.1. According to theoretical studies, the crossover from indirect to direct band gap for biaxially ε-Ge occurs at 1.5% [30], where the fundamental direct band-gap is $E_g \approxeq 0.58\ eV$ ($\lambda \approxeq 2138\ nm$). Consequently, we used $\lambda = 1500\ nm$ for the microwave pump source, ensuring that carriers are effectively excited to the fundamental L- and Γ-valleys across all heterostructures examined in this investigation. Furthermore, it is important to highlight that the underlying buffer layers are transparent at the selected wavelength, enabling us to exclusively probe the carrier dynamics within the Ge epilayers. For further details about the measurement technique, interested readers are encouraged to consult our previous works [54, 55].

The transient curves in Figure 4.5 show an initial fast roll-off, which is attributed to the fast recombination at the surface states. Beyond the fast decay regime, the transient curves are dominated by the principal mode of decay. The effective lifetime, τ_{eff}, of the principal mode of decay was obtained using exponential decay regression according to $V_{\mu-PCD}(t) = V_0 \cdot e^{\left(\frac{-t}{\tau_{eff}}\right)}$, where $V_{\mu-PCD}$ is the temporal variation of the microwave probe source response (*and is a direct measure of the change in local conductance,* $\Delta\sigma_0$), and V_0 is the peak microwave probe source intensity recorded at the instantaneous time t = 0, or in other words, the temporal instant when the optical source is removed. These findings are detailed in Table 4.1, which also includes previously reported experimentally measured τ_{eff} values from ε-Ge grown on InGaAs strain template for direct comparison [54].

A few notable insights can be drawn from Figure 4.5. The τ_{eff} obtained from heterostructure A (1.53% ε-Ge) shows $\simeq$2$\times$ improvement compared to heterostructure C, which is the control unstrained heavily B-doped Ge grown on GaAs, with AlAs as an intermediate buffer. This observation aligns qualitatively with our earlier reports, which indicate that pseudomorphic biaxially tensile strained Ge exhibits enhanced τ_{eff} compared to their unstrained counterparts, likely due to increased mobility induced by tensile strain [56–58]. It is important to note that while higher doping may lead to higher impurity scattering rates and consequently affect mobility, the interplay between doping levels and tensile strain on mobility remains insufficiently understood at the present moment. As such, we believe this enhancement in τ_{eff} represents a cumulative effect of mobility degradation due to doping and mobility enhancement due to tensile strain, with the latter exerting a more significant influence. This conjecture is further supported by the lower τ_{eff} observed in heterostructure A compared to *uid* ε-Ge grown on InGaAs strain template reported previously (*Samples R2-R4* in Table 4.1). In fact, our *uid unstrained* Ge counterparts showed higher τ_{eff} than heterostructure C (*Sample R1* in Table 4.1). Conversely, heterostructure B exhibits a reduction of $\simeq$2$\times$ in τ_{eff} compared to heterostructure A, ***insofar*** that it exhibits a similar τ_{eff} as heterostructure C. This observation can be attributed to the presence of stacking faults in heterostructure B, which act as strong Shockley-Read-Hall (SRH) recombination centers, thereby degrading the τ_{bulk} component of τ_{eff}. Additionally, surface roughness seen in heterostructure B leads to additional surface states that contribute to increased surface recombination. The resulting effect is an increased degradation in the τ_S component, in addition to the degraded τ_{bulk} in Eqn 4.1, which ultimately results in a degraded effective minority carrier lifetime, τ_{eff}.

These observations provide substantial support for the findings presented in the XRD and TEM sections, as well as for the aforementioned hypothesis. Although heterostructure B has a slightly higher tensile strain than heterostructure A, the heavy B-doping affects the crystalline integrity of the material, concomitantly reducing the benefits of tensile strain. This ultimately reinforces the hypothesis that there exists a critical tensile strain corresponding to a specific doping concentration, ε_{doping}, below which the tensile strained-induced enhancement may be retained. While this relationship has not been explicitly calculated in this work, the findings suggest that ε_{doping} likely falls between 1.53% and 1.68% tensile strain levels in this study for a doping concentration of $N_A \approxeq N_B \approx 7 \times 10^{19}\ cm^{-3}$.

4.3.4 Atomistic simulation for B-induced deformation of Ge-Ge bonds

In the current investigation, we have further employed atomistic density functional theory (DFT) framework to study the structural deformation of Ge-Ge bonds resulting from the introduction of B dopant atoms under conditions of applied tensile strain. To emulate the ~1.5% ε-Ge/InGaAs heterostructure, biaxial tensile $\langle 110 \rangle$ stress of 2.089 GPa was imposed on a relaxed energy minimized Ge supercell. Subsequent variational geometry optimization was conducted to derive the ε-Ge cell parameters. A (001) oriented ε-Ge supercell was then constructed using the determined cell parameters; within this structure, a singular Ge atom was replaced by a B atom. In adherence to periodic boundary conditions, the x and y dimensions of the supercell were set to $n \times a_{[110]}$, and z dimension was set to $(n-1) \times a_{[001]}$. Here, $n = 3$, $a_{[110]}$ is the lattice

Table 4.1: Benchmarking effective minority carrier lifetimes (τ_{eff}) of ε-Ge epilayers measured using μ-PCD technique. The microwave pump source wavelength for all reported measurements, carried out at 300 K, was kept constant at $\lambda = 1500\ nm$.

sample information				experimental setup	lifetime parameters		
label	Ge thickness (nm)	ε (%)	Doping, N_A (cm^{-3})	photon fluence per pulse ($\#\ of\ photons \cdot cm^{-2}$)	effective lifetime, τ_{eff} (ns)	error ($\pm ns$)	coeff. of determination, R^2
C	270	0.00	**B**:$\sim 7 \times 10^{19}$		30.31	1.73	0.88
A	~30	1.53	**B**:$\sim 7 \times 10^{19}$		62.41	1.34	0.97
B	~30	1.68	**B**:$\sim 7 \times 10^{19}$	1×10^8	29.67	1.03	0.95
R1 [54]	270	0.00	*uid*		95.37	0.19	0.98
R2 [54]	75	0.61	*uid*		68.46	1.16	0.95
R3 [54]	75	0.89	*uid*		89.75	1.68	0.90
R4 [54]	~30	1.60	*uid*		101.20	0.87	0.98

parameter in the x and y directions, and $a_{[001]}$ is the lattice parameter in the z direction. Geometry optimization was subsequently performed on the supercell while imposing constraints on the x, y and z directions, in order to accurately reflect the mechanical constraints exerted by the underlying III-V VS on the Ge epilayer. To ascertain the deformation induced by B atoms, we adhered to the procedural methodology delineated in Ref. [29]. Illustrated in Figure 4.6(a) is the representative supercell configuration of 1.5% ε-Ge, with $x = y = 3 \times a_{[110]}$ and $z = 2 \times a_{[001]}$, with an individual B atom incorporated into the central unit cell. This results in a B-B distance, $d_{B \longrightarrow B} \approx 12.365$ Å. An increase in the volume of the supercell corresponds directly to augmentation of the B-B distance, or in other words, reducing B-dopant concentration within the Ge epilayer. Assuming a Poisson impurity distribution profile for the B-dopant atoms within the Ge epilayer, the B-B distance, $d_{B \longrightarrow B}$, can be estimated as [59]:

$$d_{B \longrightarrow B} \approx \frac{3}{2\pi} \cdot \frac{1}{\sqrt[3]{N_B}} \tag{4.3}$$

Subsequently, for a doping concentration of $N_B \approx 7 \times 10^{19}$ cm^{-3} used in this work, $d_{B \longrightarrow B} \approx 11.585$ Å, which deviates by less than 1 Å of $d_{B \longrightarrow B}$ of the simulated supercell depicted in Figure 4.6(a), thereby corroborating the reliability of the modeled framework. The total volume of the supercell can be denoted as $V_{total} = N \cdot V_{cell}$, wherein N is the total number of unit cells incorporated in the supercell, and V_{cell} designates the volume of each discrete unit cell. It is evident from Figure 4.6(a) that the B-containing unit cell undergoes volumetric contraction attributable to the disparity in covalent radii between Ge and B. In a similar vein, given that the Ge epilayer is constrained by the III-V strain template, certain

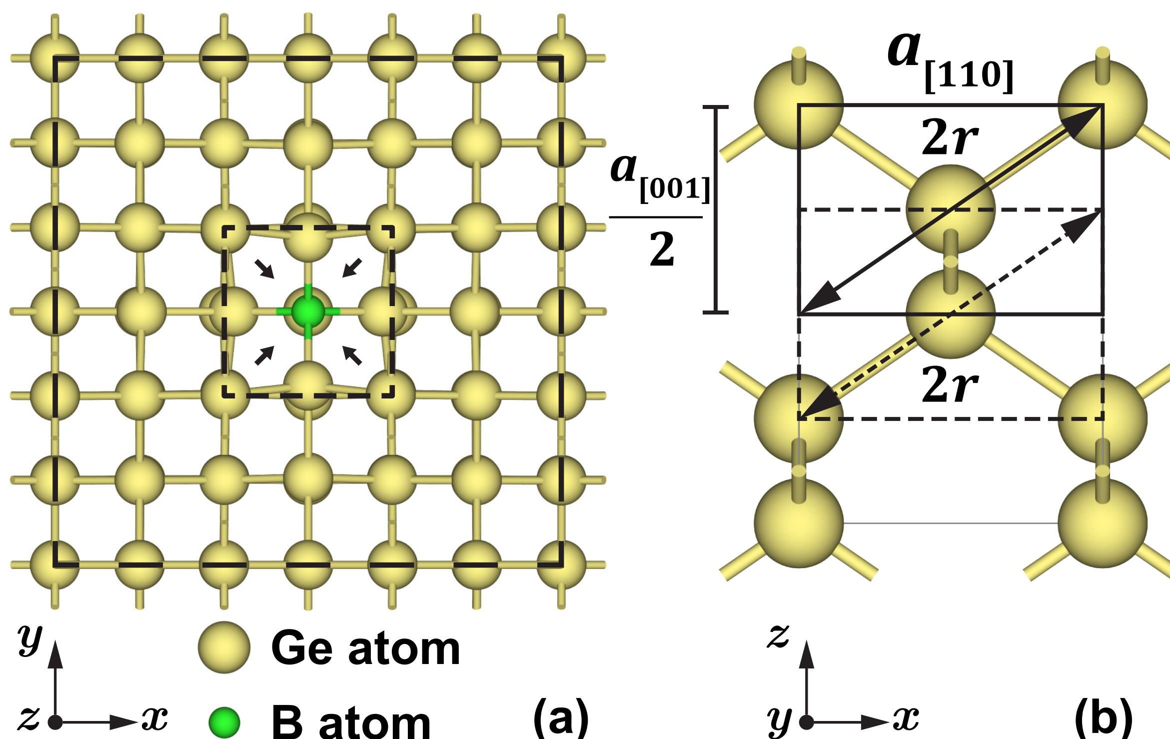

Figure 4.6: (a) Depicts a representative supercell utilized for the atomistic modeling of B dopant atoms in a (001) oriented Ge. The dimensions of the supercell are defined as $x = y = 3 \times a_{[110]}$ and $z = 2 \times a_{[001]}$, to preserve periodic boundary conditions. The dotted black line illustrates one such [110] oriented unit cell, each of which consists of either 4 Ge atoms, or 3 Ge atoms and 1 B atom. (b) Outlines the qualitative model employed for this study along the [001] direction, based on the assumption that $2r = \sqrt{a_{[110]}^2 + \left(\frac{a_{[001]}}{2}\right)^2} \approx \sqrt{a_{[110]}^2 + \left(\frac{a_{[110]}}{\sqrt{2}}\right)^2}$. The calculated changes in bond lengths are referenced against the geometry optimized *undoped*, *unstrained* bulk Ge supercell. It should be noted that tetragonal distortion induced by the III-V strain template is not considered in this qualitative model.

Ge-Ge bonds proximal to the B-containing unit cell undergo an effective expansion, which corresponds to an added tensile strain condition. Consequently, a rudimentary qualitative model may be employed to map the strain induced in the Ge-Ge bonds in the presence of substitutional B atoms. If we designate δ and γ, respectively, as proportional volumetric contraction and expansion coefficients, V_B and V_{Ge} as the volumes of B-containing unit cell and Ge-containing cells, respectively, V_{total} can be formulated as [29]:

$$V_{total} = V_B + (N-1) \cdot V_{Ge}, \tag{4.4}$$

$$V_B = \frac{V_{total}}{N} \cdot (1-\delta), \tag{4.5}$$

and

$$V_{Ge} = \frac{V_{total}}{N} \cdot (1+\gamma). \tag{4.6}$$

Finally, Figure 4.6(b) illustrates that the volume of each unit cell can be represented in relation to the Ge-Ge ($r_{Ge\longrightarrow Ge}$) or Ge-B ($r_{Ge\longrightarrow B}$) bond lengths as:

$$V_{Ge/B} = \frac{1}{\sqrt{2}} \cdot \left(\sqrt{\frac{8}{3}} \cdot r_{Ge\longrightarrow Ge/Ge\longrightarrow B}\right)^3. \tag{4.7}$$

Therefore, combining equations (4), (5), (6) and (7), we get:

$$\delta = 1 - \frac{N}{\sqrt{2}V_{total}} \cdot \left(\sqrt{\frac{8}{3}} \cdot r_{Ge \longrightarrow Ge/Ge \longrightarrow B} \right)^3 \tag{4.8}$$

leading to:

$$\delta = (N-1) \cdot \gamma. \tag{4.9}$$

We would like to highlight that this rudimentary qualitative model does not account for the tetragonal distortion caused by tensile strain from the underlying buffer. However, this omission can be justified, as the maximum error observed in mapping the B-induced tensile strain was only 1%. The values of $r_{Ge \longrightarrow Ge}$ were obtained from geometry optimized cells of bulk Ge, 1.5% ε-Ge interface supercell and B-doped 1.5% ε-Ge interface supercell, as detailed in Table 4.2. An effective additive tensile strain of $0.2854 - 0.2912$ % was identified in B-doped ε-Ge compared to *undoped* 1.5% ε-Ge, aligning closely with previously reported estimates within the constraints of atomistic modeling [29]. This range accounts for the variations in $r_{Ge \longrightarrow B}$ due to the lattice tetragonal distortion induced by tensile strain from the underlying III-V buffer template, which leads to slight differences in $r_{Ge \longrightarrow B}$ along the [110] and [001] directions. It is well established that nucleation of defects, by means of heterointerfacial misfit dislocations and gliding threading dislocations, becomes energetically favorable in mismatched heteroepitaxy when h_c is exceeded. To reiterate, while evidence of stacking faults is presented in Figures 4.3(b) and 4.4(a), no misfit dislocations were detected at the heterointerface. This observation suggests that the effective tensile strain, induced by the

III-V strain template and heavy B doping, impedes the glide of 60° perfect dislocations. Instead, the dissociation of the perfect dislocations into their 90° PD component and their subsequent glide appears to be favored, resulting in the formation of stacking faults. Consequently, this indicates an inherent modification of the strain energy balance model, suggesting that a lower effective h_c is adequate to nucleate 90° PDs and stacking faults. Referring to the strain energy balance model by People and Bean [31], 1.53% and 1.68% tensile strain levels, respectively, correspond to h_c of ∼48 nm and ∼38 nm. Given that the thickness of both Ge epilayers in this work is ∼30 nm, it can be posited that the cumulative tensile strain from the III-V strain template, and that induced by the

Table 4.2: Summary of extracted parameters obtained from atomistic simulation of *undoped* and **B**-doped *unstrained* and *tensile strained* Ge supercells

parameter		extracted value
relaxed Ge bulk cell	$r_{Ge \to Ge}$	2.48483 Å
1.5% ε-Ge interface cell	$r_{Ge \to Ge}$	2.50079 Å
1.5% **B:**ε-Ge interface cell	$r_{Ge \to Ge}$	2.50804 Å
1.5% **B:**ε-Ge interface cell	$r_{Ge \to B}$	2.18951 Å
Contraction coefficient	δ	30.515 %
Expansion coefficient	γ	0.872%
Resultant **B**-induced strain	ε_B	0.2854 - 0.2912%

substitutional B atoms, causes the h_c to be exceeded in heterostructure B. As a result, the nucleation and subsequent glide of 90° PDs becomes energetically favorable. This finding supports the observations made by XRD and TEM analyses and explains the origin of the stacking faults at the heterointerface and within the film. Furthermore, as τ_{eff} showed a twofold improvement in heterostructure A compared to heterostructure C, one can argue that the ε-Ge is pseudomorphic in heterostructure A and that h_c has not been exceeded for this system. Although we have not calculated the forces governing the nucleation and glide of 90° PDs in this study, prior research has documented this phenomenon in strained epitaxy of silicon on Ge_xSi_{1-x} VS, where a modified h_c for stacking fault generation was established [60]. Therefore, this work provides valuable insights and considerations regarding the impact of heavy B-doping of highly ε-Ge epilayers, which hold significant potential for various emerging electronic and photonic applications.

4.4 Conclusion

In summary, we have conducted a thorough investigation into the effects of heavy B-doping on highly ε-Ge, utilizing structural and effective lifetime characterization and independently validating the observations by atomistic modeling. We demonstrated successful growth of heavily B-doped 1.53% and 1.68% ε-Ge ($N_B \approx 7 \times 10^{19}\ cm^{-3}$) as confirmed by HR-XRD measurements. TEM analysis revealed a coherent and abrupt heterointerface between 1.68% ε-Ge and $In_{0.25}Ga_{0.75}As$ heterointerface, while also providing visual evidence of stacking faults and surface roughening. Measurement of effective lifetime via μ-PCD indicated that tensile strain induced an enhancement in τ_{eff} to **62 ns** (up from **30 ns** in *unstrained* highly B-doped Ge) in the 1.53% ε-Ge sample. However, no such improvement was observed in 1.68% ε-Ge despite a higher level of tensile strain, which we attribute to the presence of stacking faults and surface roughness within the Ge epilayer. Through independent first-principles atomistic calculations, we demonstrate that the deformation of Ge-Ge bonds due to substitutional B-atoms induces an *additive* tensile strain. This deformation effectively lowers the critical layer thickness, h_c, for the system, thereby energetically favoring the nucleation and subsequent glide of 90° leading PDs, which results in the formation of stacking faults. These stacking faults are primarily responsible for the lack of τ_{eff} enhancement in the 1.68% ε-Ge sample. Consequently, this work highlights that while heavily B-doped ε-Ge can be achieved, it is essential to consider the structural implications of the same. Conversely, this work provides a novel approach to achieving high tensile strain in Ge epilayers without necessitating higher InAs compositions in the underlying III-V strain template. Overall, this research provides a comprehensive understanding of ε-Ge:B/InGaAs material

system, which will be beneficial for their application in emerging electronic and photonic applications.

Bibliography

[1] O. Qiqing, Y. Min, J. Holt, S. Panda, C. Huajie, H. Utomo, M. Fischetti, N. Rovedo, L. Jinghong, N. Klymko, H. Wildman, T. Kanarsky, G. Costrini, D. M. Fried, A. Bryant, J. A. Ott, I. Meikei, and S. Chun-Yung, "Investigation of CMOS devices with embedded SiGe source/drain on hybrid orientation substrates," in *Digest of Technical Papers. 2005 Symposium on VLSI Technology, 2005.*, pp. 28–29, ISBN: 2158-9682. DOI: 10.1109/.2005.1469199.

[2] B. Liu, C. Zhan, Y. Yang, R. Cheng, P. Guo, Q. Zhou, E. Y. J. Kong, N. Daval, C. Veytizou, D. Delprat, B. Y. Nguyen, and Y. C. Yeo, "Germanium Multiple-Gate Field-Effect Transistor With In Situ Boron-Doped Raised Source/Drain," *IEEE Transactions on Electron Devices*, vol. 60, no. 7, pp. 2135–2141, 2013, ISSN: 1557-9646. DOI: 10.1109/TED.2013.2262135.

[3] E. Kasper, M. Oehme, T. Arguirov, J. Werner, M. Kittler, and J. Schulze, "Room Temperature Direct Band Gap Emission from Ge p-i-n Heterojunction Photodiodes," *Advances in optoelectronics*, vol. 2012, no. 1, p. 916 275, 2012, ISSN: 1687-5648.

[4] J. Liu, "Monolithically Integrated Ge-on-Si Active Photonics," *Photonics*, vol. 1, no. 3, pp. 162–197, 2014, ISSN: 2304-6732. DOI: 10.3390/photonics1030162.

[5] G. T. Reed, G. Z. Mashanovich, F. Y. Gardes, D. J. Thomson, Y. Hu, J. Soler-Penades, M. Nedeljkovic, A. Khokar, P. Thomas, C. Littlejohns, A. Ahmad, S. Reynolds, R. Topley, C. Mitchell, S. Stankovic, P. R. Wilson, L. Ke, T. M. B. Masaud, A. Tarazona, and H. Chong, "Silicon Photonics," in *2014 7th International*

Silicon-Germanium Technology and Device Meeting (ISTDM), pp. 5–6. DOI: 10.1109/ISTDM.2014.6874661.

[6] Y. Zhou, W. Han, L.-T. Chang, F. Xiu, M. Wang, M. Oehme, I. A. Fischer, J. Schulze, R. K. Kawakami, and K. L. Wang, "Electrical Spin Injection and Transport in Germanium," *Physical Review B*, vol. 84, no. 12, p. 125 323, 2011, PRB. DOI: 10.1103/PhysRevB.84.125323.

[7] N. W. Hendrickx, W. I. L. Lawrie, M. Russ, F. van Riggelen, S. L. de Snoo, R. N. Schouten, A. Sammak, G. Scappucci, and M. Veldhorst, "A four-qubit germanium quantum processor," *Nature*, vol. 591, no. 7851, pp. 580–585, 2021, ISSN: 1476-4687. DOI: 10.1038/s41586-021-03332-6.

[8] G. Scappucci, C. Kloeffel, F. A. Zwanenburg, D. Loss, M. Myronov, J.-J. Zhang, S. De Franceschi, G. Katsaros, and M. Veldhorst, "The germanium quantum information route," *Nature Reviews Materials*, vol. 6, no. 10, pp. 926–943, 2021, ISSN: 2058-8437. DOI: 10.1038/s41578-020-00262-z.

[9] K. Vetter, "Recent Developments in the Fabrication and Operation of Germanium Detectors," *Annual Review of Nuclear and Particle Science*, vol. 57, no. Volume 57, 2007, pp. 363–404, 2007, ISSN: 1545-4134. DOI: 10.1146/annurev.nucl.56.080805.140525.

[10] R. R. Sumathi, N. Abrosimov, K. P. Gradwohl, M. Czupalla, and J. Fischer, "Growth of heavily-doped Germanium single crystals for mid-Infrared applications," *Journal of Crystal Growth*, vol. 535, p. 125 490, 2020, ISSN: 0022-0248. DOI: 10.1016/j.jcrysgro.2020.125490.

[11] P.-Y. Hong, C.-C. Lai, T. Tsai, H.-C. Lin, T. George, D. M. T. Kuo, and P.-W. Li, "Determination of exciton binding energy using photocurrent spectroscopy of Ge quantum-dot single-hole transistors under CW pumping," *Scientific Reports*, vol. 13, no. 1, p. 14 333, 2023, ISSN: 2045-2322. DOI: 10.1038/s41598-023-41582-8.

[12] B. Dutt, D. S. Sukhdeo, D. Nam, B. M. Vulovic, Z. Yuan, and K. C. Saraswat, "Roadmap to an Efficient Germanium-on-Silicon Laser: Strain vs. *n*-Type Doping," *IEEE Photonics Journal*, vol. 4, no. 5, pp. 2002–2009, 2012, ISSN: 1943-0655. DOI: 10.1109/jphot.2012.2221692.

[13] D. S. Sukhdeo, D. Nam, J.-H. Kang, M. L. Brongersma, and K. C. Saraswat, "Direct bandgap germanium-on-silicon inferred from 5.7% ⟨100⟩ uniaxial tensile strain [Invited]," *Photonics Research*, vol. 2, no. 3, A8–A13, 2014. DOI: 10.1364/PRJ.2.0000A8.

[14] M. K. Hudait, F. Murphy-Armando, D. Saladukha, M. B. Clavel, P. S. Goley, D. Maurya, S. Bhattacharya, and T. J. Ochalski, "Design, Theoretical, and Experimental Investigation of Tensile-Strained Germanium Quantum-Well Laser Structure," *ACS Applied Electronic Materials*, vol. 3, no. 10, pp. 4535–4547, 2021. DOI: 10.1021/acsaelm.1c00660.

[15] E. Kasper, M. Kittler, M. Oehme, and T. Arguirov, "Germanium tin: silicon photonics toward the mid-infrared [Invited]," *Photonics Research*, vol. 1, no. 2, pp. 69–76, Jul. 2013, ISSN: 2327-9125. DOI: 10.1364/PRJ.1.000069.

[16] A. Gassenq, K. Guilloy, G. O. Dias, N. Pauc, D. Rouchon, J.-M. Hartmann, J. Widiez, S. Tardif, F. Rieutord, J. Escalante, I. Duchemin, Y.-M. Niquet, R. Geiger, T. Zabel, H. Sigg, J. Faist, A. Chelnokov, V. Reboud, and V. Calvo,

"1.9% bi-axial Tensile Strain in Thick Germanium Suspended Membranes Fabricated in Optical Germanium-On-Insulator Substrates for Laser Applications," *Applied Physics Letters*, vol. 107, no. 19, p. 191 904, 2015. DOI: 10.1063/1.4935590.

[17] A. Ghrib, M. El Kurdi, M. Prost, S. Sauvage, X. Checoury, G. Beaudoin, M. Chaigneau, R. Ossikovski, I. Sagnes, and P. Boucaud, "All-Around SiN Stressor for High and Homogeneous Tensile Strain in Germanium Microdisk Cavities," *Advanced Optical Materials*, vol. 3, no. 3, pp. 353–358, 2015, ISSN: 2195-1071. DOI: 10.1002/adom.201400369.

[18] V. Reboud, A. Gassenq, N. Pauc, J. Aubin, L. Milord, Q. M. Thai, M. Bertrand, K. Guilloy, D. Rouchon, J. Rothman, T. Zabel, F. A. Pilon, H. Sigg, A. Chelnokov, J. M. Hartmann, and V. Calvo, "Optically pumped GeSn micro-disks with 16% Sn lasing at 3.1 μm up to 180K," *Applied Physics Letters*, vol. 111, no. 9, p. 092 101, 2017. DOI: 10.1063/1.5000353.

[19] K. H. Koo, H. Cho, P. Kapur, and K. C. Saraswat, "Performance Comparisons Between Carbon Nanotubes, Optical, and Cu for Future High-Performance On-Chip Interconnect Applications," *IEEE Transactions on Electron Devices*, vol. 54, no. 12, pp. 3206–3215, 2007, ISSN: 1557-9646. DOI: 10.1109/TED.2007.909045.

[20] K. Saraswat, D. Kim, T. Krishnamohan, D. Kuzum, A. K. Okyay, A. Pethe, and H.-Y. Yu, "Germanium for High Performance MOSFETs and Optical Interconnects," *ECS Transactions*, vol. 16, no. 10, pp. 3–12, 2008, ISSN: 1938-5862 1938-6737. DOI: 10.1149/1.2986748.

[21] P. Chaisakul, D. Marris-Morini, J. Frigerio, D. Chrastina, M.-S. Rouifed, S. Cecchi, P. Crozat, G. Isella, and L. Vivien, "Integrated Germanium Optical Interconnects on Silicon Substrates," *Nature Photonics*, vol. 8, no. 6, pp. 482–488, 2014, ISSN: 1749-4893. DOI: 10.1038/nphoton.2014.73.

[22] J. Aubin, J. M. Hartmann, M. Veillerot, Z. Essa, and B. Sermage, "Very low temperature (450 °C) selective epitaxial growth of heavily in situ boron-doped SiGe layers," *Semiconductor Science and Technology*, vol. 30, no. 11, p. 115 006, Oct. 2015, ISSN: 0268-1242. DOI: 10.1088/0268-1242/30/11/115006.

[23] S. Uppal, A. F. Willoughby, J. M. Bonar, A. G. Evans, N. E. Cowern, R. Morris, and M. G. Dowsett, "Diffusion of ion-implanted boron in germanium," *Journal of Applied Physics*, vol. 90, no. 8, pp. 4293–4295, 2001, ISSN: 0021-8979. DOI: 10.1063/1.1402664.

[24] T.-H. Chang, C. Chang, Y.-H. Chu, C.-C. Lee, J.-Y. Chang, I.-C. Chen, and T. Li, "Low temperature growth of highly conductive boron-doped germanium thin films by electron cyclotron resonance chemical vapor deposition," *Thin solid films*, vol. 551, pp. 53–56, 2014, ISSN: 0040-6090. DOI: 10.1016/j.tsf.2013.11.099.

[25] A. Satta, E. Simoen, T. Clarysse, T. Janssens, A. Benedetti, B. De Jaeger, M. Meuris, and W. Vandervorst, "Diffusion, activation, and recrystallization of boron implanted in preamorphized and crystalline germanium," *Applied Physics Letters*, vol. 87, no. 17, 2005, ISSN: 0003-6951. DOI: 10.1063/1.2117631.

[26] P. J. Newton, J. Llandro, R. Mansell, S. N. Holmes, C. Morrison, J. Foronda, M. Myronov, D. R. Leadley, and C. H. W. Barnes, "Magnetotransport in p-type Ge

quantum well narrow wire arrays," *Applied Physics Letters*, vol. 106, no. 17, 2015, ISSN: 0003-6951. DOI: 10.1063/1.4919053.

[27] M. B. Clavel, J.-S. Liu, M. A. Meeker, G. A. Khodaparast, Y. Xie, J. J. Heremans, S. Bhattacharya, and M. K. Hudait, "Electronic and optical properties of highly boron-doped epitaxial Ge/AlAs(001) heterostructures," *Journal of Applied Physics*, vol. 127, no. 7, 2020, ISSN: 0021-8979. DOI: 10.1063/1.5130567.

[28] G. Zhou, K. H. Lee, D. H. Anjum, Q. Zhang, X. Zhang, C. S. Tan, and G. Xia, "Impacts of doping on epitaxial germanium thin film quality and Si-Ge interdiffusion," *Optical Materials Express*, vol. 8, no. 5, pp. 1117–1131, 2018, (Maggie). DOI: 10.1364/OME.8.001117.

[29] M. B. Clavel, G. Greene-Diniz, M. Grüning, K. T. Henry, M. Kuhn, R. J. Bodnar, and M. K. Hudait, "Engineering the Interfacial Electronic Structure of Epitaxial Ge/AlAs(001) Heterointerfaces via Substitutional Boron Incorporation: The Roles of Doping and Interface Stoichiometry," *ACS Applied Electronic Materials*, vol. 1, no. 12, pp. 2646–2654, 2019. DOI: 10.1021/acsaelm.9b00615.

[30] D. Saladukha, M. B. Clavel, F. Murphy-Armando, G. Greene-Diniz, M. Grüning, M. K. Hudait, and T. J. Ochalski, "Direct and indirect band gaps in Ge under biaxial tensile strain investigated by photoluminescence and photoreflectance studies," *Physical Review B*, vol. 97, no. 19, p. 195 304, 2018, PRB. DOI: 10.1103/PhysRevB.97.195304.

[31] R. People and J. C. Bean, "Calculation of critical layer thickness versus lattice mismatch for Ge_xSi_{1-x}/Si strained-layer heterostructures," *Applied Physics Letters*, vol. 47, no. 3, pp. 322–324, 1985, ISSN: 0003-6951. DOI: 10.1063/1.96206.

[32] S. Smidstrup, T. Markussen, P. Vancraeyveld, J. Wellendorff, J. Schneider, T. Gunst, B. Verstichel, D. Stradi, P. A. Khomyakov, U. G. Vej-Hansen, M.-E. Lee, S. T. Chill, F. Rasmussen, G. Penazzi, F. Corsetti, A. Ojanperä, K. Jensen, M. L. N. Palsgaard, U. Martinez, A. Blom, M. Brandbyge, and K. Stokbro, "QuantumATK: an integrated platform of electronic and atomic-scale modelling tools," *Journal of Physics: Condensed Matter*, vol. 32, no. 1, p. 015 901, 2020, ISSN: 0953-8984. DOI: 10.1088/1361-648X/ab4007.

[33] M. A. L. Marques, M. J. T. Oliveira, and T. Burnus, "Libxc: A library of exchange and correlation functionals for density functional theory," *Computer Physics Communications*, vol. 183, no. 10, pp. 2272–2281, 2012, ISSN: 0010-4655. DOI: 10.1016/j.cpc.2012.05.007.

[34] M. Schlipf and F. Gygi, "Optimization algorithm for the generation of ONCV pseudopotentials," *Computer Physics Communications*, vol. 196, pp. 36–44, 2015, ISSN: 0010-4655. DOI: 10.1016/j.cpc.2015.05.011.

[35] J.-M. Chauveau, Y. Androussi, A. Lefebvre, J. D. Persio, and Y. Cordier, "Indium Content Measurements in Metamorphic High Electron Mobility Transistor Structures by Combination of X-Ray Reciprocal Space Mapping and Transmission Electron Microscopy," *Journal of Applied Physics*, vol. 93, no. 7, pp. 4219–4225, 2003. DOI: 10.1063/1.1544074.

[36] G. Bauer, J. Li, and E. Koppensteiner, "X-ray reciprocal space mapping of $Si/Si_{1-x}Ge_x$ heterostructures," *Journal of Crystal Growth*, vol. 157, no. 1, pp. 61–67, 1995, ISSN: 0022-0248. DOI: 10.1016/0022-0248(95)00372-X.

[37] K. L. Kavanagh, M. A. Capano, L. W. Hobbs, J. C. Barbour, P. M. J. Marée, W. Schaff, J. W. Mayer, D. Pettit, J. M. Woodall, J. A. Stroscio, and R. M. Feenstra, "Asymmetries in dislocation densities, surface morphology, and strain of GaInAs/GaAs single heterolayers," *Journal of Applied Physics*, vol. 64, no. 10, pp. 4843–4852, Nov. 1988, ISSN: 0021-8979. DOI: 10.1063/1.341232.

[38] O. Madelung, *Elements of the IVth group and IV-IV compounds.* Springer Berlin Heidelberg, 2012, pp. 7–70, ISBN: 9783642188657. DOI: 10.1007/978-3-642-18865-7_2.

[39] H. H. Radamson, K. B. Joelsson, W. X. Ni, J. Birch, J. E. Sundgren, L. Hultman, and G. V. Hansson, "Strain characterization of $Ge_{1-x}Si_x$ and heavily B-doped Ge layers on Ge(001) by two-dimensional reciprocal space mapping," *Journal of Crystal Growth*, vol. 167, no. 3, pp. 495–501, 1996, ISSN: 0022-0248. DOI: 10.1016/0022-0248(96)00294-1.

[40] P. M. J. Marée, J. C. Barbour, J. F. van der Veen, K. L. Kavanagh, C. W. T. Bulle-Lieuwma, and M. P. A. Viegers, "Generation of misfit dislocations in semiconductors," *Journal of Applied Physics*, vol. 62, no. 11, pp. 4413–4420, 1987, ISSN: 0021-8979. DOI: 10.1063/1.339078.

[41] M. Clavel, P. Goley, N. Jain, Y. Zhu, and M. K. Hudait, "Strain-Engineered Biaxial Tensile Epitaxial Germanium for High-Performance Ge/InGaAs Tunnel Field-Effect Transistors," *IEEE Journal of the Electron Devices Society*, vol. 3, no. 3, pp. 184–193, 2015, ISSN: 2168-6734. DOI: 10.1109/JEDS.2015.2394743.

[42] D. P. Miller, J. E. Moore, and C. R. Moore, "Boron induced dislocations in silicon," *Journal of Applied Physics*, vol. 33, no. 8, pp. 2648–2652, 1962, ISSN: 0021-8979. DOI: 10.1063/1.1729037.

[43] G. H. Schwuttke, "Boron-Induced Microstrains in Dislocation-Free Silicon Crystals," *Journal of Applied Physics*, vol. 34, no. 6, pp. 1662–1664, 1963, ISSN: 0021-8979. DOI: 10.1063/1.1702652.

[44] S. Chopra, M. C. Ozturk, V. Misra, K. McGuire, and L. E. McNeil, "Analysis of boron strain compensation in silicon-germanium alloys by Raman spectroscopy," *Applied Physics Letters*, vol. 88, no. 20, 2006, ISSN: 0003-6951. DOI: 10.1063/1.2205752.

[45] J. Tersoff and F. K. LeGoues, "Competing relaxation mechanisms in strained layers," *Physical review letters*, vol. 72, no. 22, pp. 3570–3573, 1994, ISSN: 0031-9007. DOI: 10.1103/physrevlett.72.3570.

[46] M. K. Hudait, S. Bhattacharya, S. Karthikeyan, J. Zhao, R. J. Bodnar, B. A. Magill, and G. A. Khodaparast, "Mapping the Ge/InAl(Ga)As interfacial electronic structure and strain relief mechanism in germanium quantum dots," *Journal of Materials Chemistry C*, vol. 12, no. 35, pp. 14 062–14 073, 2024, ISSN: 2050-7526. DOI: 10.1039/D4TC01587H.

[47] X. Lu, Z. Jiang, H. Zhu, X. Zhang, and X. Wang, "Observation of boron doping induced surface roughening in silicon molecular beam epitaxy," *Applied Physics Letters*, vol. 68, no. 23, pp. 3278–3280, 1996, ISSN: 0003-6951. DOI: 10.1063/1.116573.

[48] E. Gaubas and J. Vanhellemont, "Comparative Study of Carrier Lifetime Dependence on Dopant Concentration in Silicon and Germanium," *Journal of The Electrochemical Society*, vol. 154, no. 3, H231, 2007, ISSN: 0013-4651. DOI: 10.1149/1.2429031.

[49] J. J. Sheng, D. Leonhardt, S. M. Han, S. W. Johnston, J. G. Cederberg, and M. S. Carroll, "Empirical correlation for minority carrier lifetime to defect density profile in germanium on silicon grown by nanoscale interfacial engineering," *Journal of Vacuum Science & Technology B*, vol. 31, no. 5, p. 051 201, 2013. DOI: 10.1116/1.4816488.

[50] S. Deb and B. R. Nag, "Measurement of lifetime of carriers in semiconductors through microwave reflection," *Journal of Applied Physics*, vol. 33, no. 4, pp. 1604–1604, 1962, ISSN: 0021-8979 1089-7550. DOI: 10.1063/1.1728779.

[51] S. Johnston, K. Zaunbrecher, R. Ahrenkiel, D. Kuciauskas, D. Albin, and W. Metzger, "Simultaneous Measurement of Minority-Carrier Lifetime in Single-Crystal CdTe Using Three Transient Decay Techniques," *IEEE Journal of Photovoltaics*, vol. 4, no. 5, pp. 1295–1300, 2014, ISSN: 2156-3403. DOI: 10.1109/JPHOTOV.2014.2339491.

[52] K. L. Luke and L.-J. Cheng, "Analysis of the interaction of a laser pulse with a silicon wafer: Determination of bulk lifetime and surface recombination velocity," *Journal of Applied Physics*, vol. 61, no. 6, pp. 2282–2293, 1987, ISSN: 0021-8979. DOI: 10.1063/1.337938.

[53] E. Yablonovitch and T. J. Gmitter, "A contactless minority lifetime probe of heterostructures, surfaces, interfaces and bulk wafers," *Solid-State*

Electronics, vol. 35, no. 3, pp. 261–267, 1992, ISSN: 0038-1101. DOI: 10.1016/0038-1101(92)90230-A.

[54] S. Bhattacharya, S. W. Johnston, S. Datta, and M. K. Hudait, "Interplay Between Strain and Thickness on the Effective Carrier Lifetime of Buffer-Mediated Epitaxial Germanium Probed by the Photoconductance Decay Technique," *ACS Applied Electronic Materials*, vol. 5, no. 6, pp. 3190–3197, May 2023, ISSN: 2637-6113. DOI: 10.1021/acsaelm.3c00256.

[55] S. Bhattacharya, S. W. Johnston, R. J. Bodnar, and M. K. Hudait, "Elucidating the Role of InGaAs and InAlAs Buffers on Carrier Dynamics of Tensile-Strained Ge Double Heterostructures," *ACS Applied Electronic Materials*, vol. 6, no. 6, pp. 4247–4256, Jun. 2024, ISSN: 2637-6113. DOI: 10.1021/acsaelm.4c00347.

[56] M. El Kurdi, H. Bertin, E. Martincic, M. de Kersauson, G. Fishman, S. Sauvage, A. Bosseboeuf, and P. Boucaud, "Control of direct band gap emission of bulk germanium by mechanical tensile strain," *Applied Physics Letters*, vol. 96, no. 4, 2010, ISSN: 0003-6951. DOI: 10.1063/1.3297883.

[57] F. Murphy-Armando and S. Fahy, "Giant enhancement of *n*-type carrier mobility in highly strained germanium nanostructures," *Journal of Applied Physics*, vol. 109, no. 11, p. 113 703, 2011. DOI: 10.1063/1.3590334.

[58] M. B. Clavel, F. Murphy-Armando, Y. Xie, K. T. Henry, M. Kuhn, R. J. Bodnar, G. A. Khodaparast, D. Smirnov, J. J. Heremans, and M. K. Hudait, "Multivalley Electron Conduction at the Indirect-Direct Crossover Point in Highly Tensile-Strained Germanium," *Physical Review Applied*, vol. 18, no. 6, p. 064 083, 2022, PRAPPLIED. DOI: 10.1103/PhysRevApplied.18.064083.

[59] E. F. Schubert, *Doping in III-V Semiconductors* (Cambridge Studies in Semiconductor Physics and Microelectronic Engineering). Cambridge: Cambridge University Press, 1993, ISBN: 9780521419192. DOI: 10.1017/CBO9780511599828.

[60] J. Parsons, R. J. H. Morris, D. R. Leadley, E. H. C. Parker, D. J. F. Fulgoni, and L. J. Nash, "Relaxation of strained silicon on $Si_{0.5}Ge_{0.5}$ virtual substrates," *Applied Physics Letters*, vol. 93, no. 7, 2008, ISSN: 0003-6951. DOI: 10.1063/1.2975188.

This page left intentionally blank

Chapter 5:

Summary and Future Prospects

5.1 Summary

In summary, *this research work* offers an in-depth analysis of tensile-strained germanium (ε-Ge) realized through the utilization of III-V metamorphic buffer layers—specifically InGaAs and InAlAs—as strain-inducing templates. As detailed in Chapter 1, this heterostructure platform is anticipated to be instrumental in the development of next-generation electronic and photonic devices. A comprehensive understanding of the intrinsic and extrinsic properties of this material system is essential to inform future research trajectories and facilitate technological integration. The principal findings of this work are delineated below:

1. In Chapter 2, the crystallographic and carrier dynamic properties of (ε-Ge) epitaxially grown *via* $In_xGa_{1-x}As$ are comprehensively analyzed. Material quality assessment is performed through effective minority carrier lifetime measurements (τ_{eff}), obtained *via* microwave-photoconductance decay (μ-PCD) technique.

High-resolution x-ray diffraction (HR-XRD) measurements confirm tensile strain levels of 0.61% and 0.89% within the Ge epilayers. Cross-sectional high-resolution transmission electron microscopy (HR-XTEM) micrographs reveal the presence of coherent and atomically abrupt ε-Ge/III–V heterointerfaces. Thickness-dependent τ_{eff} measurements conducted on *unstrained* Ge/AlAs/GaAs heterostructures yield a bulk carrier lifetime, τ_{bulk}, of $\approx 114 \pm 2$ ns, with a surface recombination velocity $S \approx 21.3 \pm 0.04$ cm/sec. Enhanced τ_{eff} values in the ε-Ge epilayers indicate an improvement in both τ_{bulk} and surface recombination lifetime, τ_S, within the active ε-Ge epilayers relative to their *unstrained* counterparts. These findings validate the potential of this heteroepitaxial system for the development of advanced electronic and photonic devices.

2. In Chapter 3, a detailed comparative analysis of the metamorphic buffer layers employed as the ε-Ge strain accommodation templates was conducted, focusing on $In_xGa_{1-x}As$ and $In_xAl_{1-x}As$ buffers. High-resolution x-ray diffraction (HR-XRD) and Raman spectroscopy were employed synergistically to verify the effective transfer of strain to the underlying Ge active layers. A key distinction in the strain relaxation mechanisms was elucidated through atomic force microscopy (AFM) surface morphology assessments, revealing non-uniform relaxation phenomena within $In_xAl_{1-x}As$-based metamorphic buffers, which correlated with increased surface roughness metrics. Microwave-reflectance photoconductance decay (μ-PCD) measurements of the effective carrier lifetime, τ_{eff}, demonstrated the superior strain accommodation capability of $In_xGa_{1-x}As$ buffers relative to $In_xAl_{1-x}As$, exhibiting superior surface morphology and enhanced τ_{eff} in the active ε-Ge

epilayers. Therefore, these findings establishes InGaAs as the preferable strain template for active ε-Ge epilayers, while also warranting further optimization for InAlAs metamorphic buffer stressor, should higher band offsets be required for specific applications. Subsequently, with InGaAs confirmed as the preferred strain template, the feasibility of quantum well (QW) double heterostructures—mimicking conventional separate confinement heterostructure (SCH) configurations with InGaAs cladding layers—was investigated. μ-PCD analysis on both *uncapped* and InGaAs-capped ε-Ge double heterostructures indicated measurable lifetime degradation, potentially attributable to interface quality deterioration at the InGaAs/ε-Ge heterointerface, underscoring the necessity for optimization of epitaxial overlayer growth conditions. Additionally, HR-XRD studies confirmed that low-temperature growth of InGaAs on ε-Ge substrates is feasible without inducing appreciable relaxation within the active epitaxial layer, although further process optimization is required to mitigate the observed decline in τ_{eff}.

3. In Chapter 4, a combined theoretical and experimental framework was employed to elucidate the effects of high-concentration *in-situ* boron (B) doping in ε-Ge epilayers, reaching dopant concentrations on the order of $N_A \approx N_B \approx 7 \times 10^{19}\ cm^{-3}$, thereby addressing a significant gap within existing literature. High-resolution x-ray diffraction (HR-XRD) quantification indicated tensile strain levels up to 1.68%, beyond the indirect-to-direct band-gap *crossover point* in [001] biaxially ε-Ge. Cross sectional high-resolution transmission electron microscopy (HR-XTEM) micrographs revealed stacking faults and pronounced surface roughness in B-doped 1.68% ε-Ge. Microwave reflectance photoconductance

(μ-PCD) measurements demonstrated a twofold τ_{eff} increase in B-doped 1.53% ε-Ge, whereas in B-doped 1.68% ε-Ge, no such enhancement was observed, attributed to defect formation associated with stacking faults, as well as, surface morphology degradation. These observations identified a critical tensile strain threshold, denoted as ε_{doping}, which is doping-concentration dependent, beyond which doping-induced defect nucleation becomes unavoidable. Complementary first-principles atomistic simulations established that high-level B incorporation induces local deformation of Ge–Ge bonds near substitutional B sites, resulting in an *additive* residual tensile strain component. This deformation-driven strain energy effectively reduces the critical layer thickness, h_c, augmenting the propensity for dislocation and defect formation while simultaneously influencing surface roughness evolution. Although detailed modeling of the competition between dislocation nucleation and surface roughening was beyond the scope of this study, the critical importance of optimizing dopant incorporation to balance tensile strain and defect nucleation was emphasized. Conversely, these findings suggest that heavy B doping constitutes a novel route to attain elevated tensile strains in active Ge layers, offering an alternative to high InAs molar fractions in InGaAs heterostructures and potentially mitigating lattice-mismatch limitations inherent to heteroepitaxial growth.

Figure 5.1 presents a comprehensive overview of the principal findings from this study. The effective carrier lifetime values, τ_{eff}, obtained through μ-PCD measurements across all examined samples, are plotted as a function of the applied in-plane biaxial tensile strain, ε. In the case of *bulk-like* Ge epitaxial layers (*i.e.* $\varepsilon = 0\%$), a clear relationship

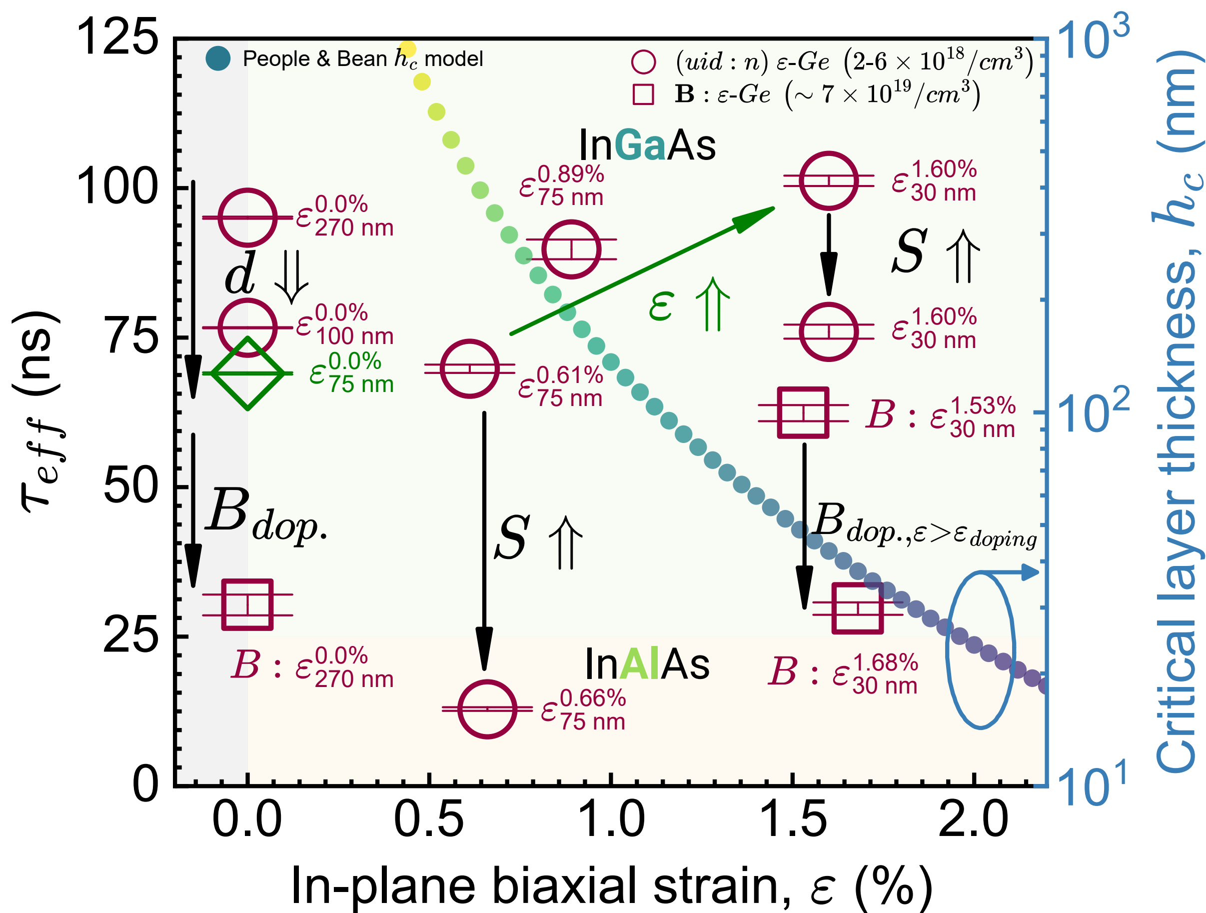

Figure 5.1: Summary of key findings in this research work. μ-PCD measured τ_{eff} values are plotted against the in-plane biaxial tensile strain, ε.

between τ_{eff} and the epilayer thickness, d, is observed, as indicated by the downward pointing arrow (black). Additionally, heavy boron doping results in notable mobility degradation, primarily due to ionized impurity scattering. This effect is consistent with the relationship $\mu_{impurity} \propto \frac{1}{N_A} \propto \frac{1}{N_D}$, where N_A and N_D refer to acceptor and donor impurity concentrations, respectively. Consequently, these factors influence the local conductance variation, $\Delta\sigma$, as follows:

$$\Delta n \approx \frac{\Delta\sigma}{q \cdot (\mu_e + \mu_h)}, \tag{5.1}$$

where Δn, q, μ_e and μ_h signify the photogenerated excess carrier concentration in $\#/cm^3$, elementary charge, and mobility of electrons and holes, respectively. It is assumed that equal quantities of excess electrons and holes are generated by optical excitation, *i.e.*, $\Delta n = \Delta p$. This induced change in the conductance of the sample, $\Delta\sigma$, is manifested as a change in the reflected microwave power, $P(\sigma)$, by ΔP. Specifically, Kunst *et al.* demonstrated that [1]:

$$\frac{\Delta P}{P(\sigma)} = A \cdot \Delta\sigma, \tag{5.2}$$

where A is the system response sensitivity factor. This relationship underscores the utility of the μ-PCD technique for assessing material quality. Furthermore, the observed reduction in τ_{eff} for heavily B-doped *unstrained* Ge epilayers—where the effects of doping overshadow the influence of thickness—provides additional insight. Interestingly, this method effectively distinguishes between τ_{eff} in moderately-*uid*:Ge

($N_D \approx 2-6 \times 10^{18}$ cm^{-3}) and heavily B-doped:Ge ($N_A \approx 7 \times 10^{19}$ cm^{-3}), demonstrating its effectiveness in characterizing τ_{eff} at different doping regimes.

The interaction between layer thickness, d, and tensile strain, ε, is also evident in the data presented in Figure 5.1. The enhancement in τ_{eff} in ε-Ge epilayers is likely a combined effect of decreased photon scattering and a reduction in conductivity mass resulting from the induced tensile strain [2, 3], as detailed in Section 2.3.3. However, this enhancement was limited to ε-Ge epilayers grown using $In_xGa_{1-x}As$ metamorphic strain templates. Conversely, due to asymmetric relaxation dynamics within Al-based $In_xAl_{1-x}As$ metamorphic buffers, a deterioration of surface morphology is observed in ε-Ge epilayers grown on this strain template, as discussed extensively in Section 3.3.3 and Section 3.3.4. This deterioration correlates with a reduction in the effective carrier lifetime, τ_{eff}. As previously noted, $In_xGa_{1-x}As$ metamorphic buffers offer a more suitable approach for integrating ε-Ge epilayers. Another important observation is the measurable decrease in τ_{eff} in InGaAs-capped ε-Ge epilayers compared to *uncapped* counterparts, indicating potential degradation at the top InGaAs/ε-Ge heterointerface, which could negatively impact the surface recombination component, τ_S, of τ_{eff} and thus result in overall lower τ_{eff}. These findings underscore the necessity for further optimization of the overlayer growth process and highlight the significance of both the top III-V/ε-Ge and bottom ε-Ge/III-V heterointerfaces in the development of Ge-based heterostructures for optical applications.

The interaction between tensile-strain-induced enhancement and heavy doping-induced degradation of τ_{eff}, as illustrated in Figure 5.1, is of particular interest. In the 1.68% ε-Ge epilayer, a reduction in τ_{eff} due to heavy B-doping is observed, which is attributed

to defect nucleation resulting from the dynamic modification of the critical layer thickness, h_c, within the material system. Conversely, the 1.53% ε-Ge epilayer demonstrates an increase in τ_{eff} driven by tensile strain, suggesting suppression of the doping-related τ_{eff} degradation despite being B-doped to the same level. These findings imply the existence of a doping-dependent critical tensile strain threshold, denoted as ε_{doping}, which warrants further investigation beyond the scope of this current study.

Thus, this research study presents several important findings that can serve as valuable guidelines for the effective utilization of the ε-Ge/III-V and III-V/ε-Ge/III-V material systems in the development of advanced electronic and photonic devices.

5.2 Future Work

While this investigative study yields multiple pivotal empirical results, certain unresolved and methodologically significant inquiries persist, which are systematically enumerated as follows:

1. In Chapters 2, 3, and 4, an enhancement of the effective carrier lifetime, τ_{eff}, was observed in ε-Ge epilayers. This improvement was attributed to a potential increase in carrier mobility induced by tensile strain. While the augmentation of τ_{eff} is advantageous, a comprehensive theoretical framework—encompassing both qualitative and quantitative analyses—must be developed to elucidate the underlying physical mechanisms governing this strain-induced enhancement.

2. In Chapter 4 (as depicted in Figure 5.1), the interaction between strain effects and

doping concentrations on τ_{eff} was examined. A hypothesis was posited regarding the existence of a doping-dependent critical tensile strain, ε_{doping}, beyond which the energetics favor the formation of Shockley partial dislocations in B-doped ε-Ge epilayers. Exceeding this threshold appears to promote the nucleation of such partial dislocations. Accordingly, an important research direction involves quantitatively analyzing the forces acting on 90° partial dislocations under varying doping and strain conditions to determine the inflection point of ε_{doping}. Development of a look-up table outlining ε_{doping} as a function of doping levels would serve as a valuable design parameter. Further, investigating the suppression mechanisms of 60° perfect dislocations, which may facilitate the formation of 90° partial dislocations, could yield insights to optimize defect engineering strategies for heavily doped ε-Ge epilayers.

3. In Chapter 3, empirical observations indicated superior crystallinity of ε-Ge layers grown on InGaAs metamorphic buffers relative to those on InAlAs buffers. Consequently, InGaAs was identified as the optimal metamorphic buffer for integrating ε-Ge. Nevertheless, InAlAs buffers offer notable advantages in the context of QW heterostructures intended for Ge-based optoelectronic devices. Specifically, (i) higher conduction and valence band offsets facilitate enhanced electronic confinement, and (ii) greater optical mode confinement arises from the significant difference in refractive indices between InAlAs and ε-Ge. Therefore, targeted optimization of InAlAs metamorphic buffers is necessary to expand their applicability in ε-Ge integration and to improve the performance of Ge-based optical sources.

4. Ultimately, in Chapter 3, although we demonstrated the viability of constructing

InGaAs-capped III–V/ε-Ge/III–V heterostructures that emulate QW separate confinement heterostructures, a measurable decline in τ_{eff} was observed. This underscores the critical importance of the top heterointerface between III–V and IV materials in the realization of high-quality QW double heterostructures. Additional optimization of interface quality, doping profiles, and growth parameters is anticipated to significantly enhance the performance and facilitate the broader adoption of Ge-based optoelectronic devices.

Bibliography

[1] M. Kunst and G. Beck, "The study of charge carrier kinetics in semiconductors by microwave conductivity measurements," *Journal of Applied Physics*, vol. 60, no. 10, pp. 3558–3566, 1986. DOI: 10.1063/1.337612.

[2] M. E. Kurdi, G. Fishman, S. Sauvage, and P. Boucaud, "Band structure and optical gain of tensile-strained germanium based on a 30 band $\vec{k} \cdot \vec{p}$ formalism," *Journal of Applied Physics*, vol. 107, no. 1, p. 013 710, 2010. DOI: 10.1063/1.3279307.

[3] F. Murphy-Armando and S. Fahy, "Giant enhancement of n-type carrier mobility in highly strained germanium nanostructures," *Journal of Applied Physics*, vol. 109, no. 11, p. 113 703, 2011. DOI: 10.1063/1.3590334.

Appendices

This page left intentionally blank

Appendix A:

List of Publications

[1] **S. Bhattacharya**, S. W. Johnston, R. J. Bodnar, and M. K. Hudait, "Elucidating the Role of InGaAs and InAlAs Buffers on Carrier Dynamics of Tensile-Strained Ge Double Heterostructures," *ACS Applied Electronic Materials*, vol. 6, no. 6, pp. 4247–4256, Jun. 2024, ISSN: 2637-6113. DOI: 10.1021/acsaelm.4c00347.

[2] M. K. Hudait, **S. Bhattacharya**, S. Karthikeyan, J. Zhao, R. J. Bodnar, B. A. Magill, and G. A. Khodaparast, "Mapping the Ge/InAl(Ga)As interfacial electronic structure and strain relief mechanism in germanium quantum dots," *Journal of Materials Chemistry C*, vol. 12, no. 35, pp. 14 062–14 073, 2024, ISSN: 2050-7526. DOI: 10.1039/D4TC01587H.

[3] **S. Bhattacharya**, S. W. Johnston, S. Datta, and M. K. Hudait, "Interplay Between Strain and Thickness on the Effective Carrier Lifetime of Buffer-Mediated Epitaxial Germanium Probed by the Photoconductance Decay Technique," *ACS Applied Electronic Materials*, vol. 5, no. 6, pp. 3190–3197, May 2023, ISSN: 2637-6113. DOI: 10.1021/acsaelm.3c00256.

[4] M. B. Clavel, **S. Bhattacharya**, and M. K. Hudait, "Atomic layer deposited tantalum silicate on crystallographically-oriented epitaxial germanium: interface chemistry and band alignment," *Materials Advances*, vol. 3, no. 12, pp. 5001–5011, 2022. DOI: 10.1039/D2MA00208F.

[5] M. K. Hudait, S. W. Johnston, M. B. Clavel, **S. Bhattacharya**, S. Karthikeyan, and R. Joshi, "High carrier lifetimes in epitaxial germanium–tin/Al(In)As heterostructures with variable tin compositions," *Journal of Materials Chemistry C*, vol. 10, no. 29, pp. 10 530–10 540, 2022, ISSN: 2050-7526. DOI: 10.1039/D2TC00830K.

[6] M. K. Hudait, M. Meeker, J.-S. Liu, M. B. Clavel, **S. Bhattacharya**, and G. A. Khodaparast, "Temperature and doping-dependent interplay between the direct and indirect optical response in buffer-mediated epitaxial germanium," *Optical Materials*, vol. 131, p. 112 633, 2022, ISSN: 0925-3467. DOI: 10.1016/j.optmat.2022.112633.

[7] M. K. Hudait, F. Murphy-Armando, D. Saladukha, M. B. Clavel, P. S. Goley, D. Maurya, **S. Bhattacharya**, and T. J. Ochalski, "Design, Theoretical, and Experimental Investigation of Tensile-Strained Germanium Quantum-Well Laser Structure," *ACS Applied Electronic Materials*, vol. 3, no. 10, pp. 4535–4547, 2021. DOI: 10.1021/acsaelm.1c00660.

[8] M. B. Clavel, J.-S. Liu, M. A. Meeker, G. A. Khodaparast, Y. Xie, J. J. Heremans, **S. Bhattacharya**, and M. K. Hudait, "Electronic and optical properties of highly boron-doped epitaxial Ge/AlAs(001) heterostructures," *Journal of Applied Physics*, vol. 127, no. 7, 2020, ISSN: 0021-8979. DOI: 10.1063/1.5130567.

[9] M. K. Hudait, M. B. Clavel, J.-S. Liu, and **S. Bhattacharya**, “In Situ SiO_2 Passivation of Epitaxial (100) and (110) InGaAs by Exploiting $TaSiO_x$ Atomic Layer Deposition Process,” *ACS omega*, vol. 3, no. 11, pp. 14 567–14 574, 2018, ISSN: 2470-1343. DOI: 10.1021/acsomega.8b02314.